Fast Magnetic Reconnection in Relativistic Laser-Plasma Interactions

by

Anthony Elias Raymond

A dissertation submitted in partial fulfillment
of the requirements for the degree of
Doctor of Philosophy
(Applied Physics)
in the University of Michigan
2016

Doctoral Committee:
Professor Karl M. Krushelnick, Chair
Research Scientist Gennady Fiksel
Research Scientist Anatoly M. Maksimchuk
Associate Professor Alexander G. R. Thomas
Assistant Professor Louise Willingale

Acknowledgments

The work presented in this Thesis would not have been possible without the steadfast support of the University of Michigan's High Field Science group. Foremost, I would like to thank my adviser Karl Krushelnick for providing invaluable guidance during my studies, and providing me with the opportunities to contribute to many research experiments both local and external. Thank you Louise Willingale for the insightful conversations, meticulous editing, and for trusting me to lead the external Titan campaign. Thanks Alec Thomas, for the invaluable discussions. A major thank you to Anatoly Maksimchuk, in whose laboratory I learned the tricks of the trade. Thank you Victor Yanovsky, Vladimir Chykov, John Nees, and Bixue Hou for keeping the show running. Thanks to all the staff and scientists with whom I worked at the Jupiter Laser Facility and Laboratory for Laser Energetics for the patience and support, especially Jaebum Park. In addition, much appreciation is extended to all of our collaborators in Princeton, especially Chuanfei Dong. I would like to thank all of my fellow graduate students without whose hard work and occasional emotional support the last few years would not have been as fruitful, especially Calvin Zulick and Andrew McKelvey. Thank you Dr. Marble and Dr. McCoy for sharpening my physical intuition. Thank you Mrs. Aldridge for sparking my interest in the physical sciences. Special thanks to the Mighty Good Coffee, RoosRoast, and Hyperion Roasting companies for the quality caffeine. I would also like to acknowledge the endless support of the Applied Physics department, in particular Cynthia McNabb and Cagliyan Kurdak, and the Alfred P. Sloan Foundation for the financial aid.

I'd like to thank my family, who have supported me until this point. Finally, thank you Hannah for everything.

The HERCULES reconnection experiments were conceived collaboratively by K. Krushel-

nick, A. Thomas, L. Willingale, and A. Maksimchuk, and executed by A. Raymond, A. McKelvey, and C. Zulick with experimental support from V. Yanovsky, V. Chvykov, A. Maksimchuk, J. Nees, and B. Hou. The Omega EP experiments were designed collaboratively by A. Raymond, K. Krushelnick, L. Willingale, and A. Thomas, with experimental support from P. Campbell, H. Chen, D. Haberberger, C. Mileham, P. Nilson, C. Stoekl, and M. S. Wei, with target development support from P. Fitzsimmons, N. Alexander, and E. Del Rio. The Titan experiments were designed by A. Raymond and L. Willingale with experimental support from J. Park, A. McKelvey, S. Nagel, A. Hazi, and S. Andrews. Data and simulation analysis was performed by A.Raymond with support from C. F. Dong, W. Fox, A. Bhattacharjee, A. Thomas, L. Willingale, and K. Krushelnick.

Grateful acknowledgement is owed for the use of NASA's High End Computing Capability.

Preface

This thesis presents work reported by the Author in the following publications:

1. Relativistic Magnetic Reconnection in the Laboratory, *Nature Communications*, 2016 (Accepted).

2. Fast, Relativistic Magnetic Reconnection in Intense Laser-Plasma Interactions, *Physics of Plasmas*, 2016 (In Preparation).

3. Asymmetric, Fast Magnetic Reconnection in the Relativistic Regime, *IEEE*, 2016 (In Preparation).

The Author has also participated in research reported in the following publications not present in this thesis.

1. A Maksimchuk, **A Raymond**, F Yu, F Dollar, L Willingale, C Zulick, K Krushelnick, G M Petrov, J Davis. Dominant deuteron acceleration with a high-intensity laser for isotope production and neutron generation. *Appl. Phys. Lett.* 102, 191117 (2013).

2. C Zulick, F Dollar, V Chvykov, J Davis, G Kalinchenko1, A Maksimchuk, G. M. Petrov, **A. Raymond**, A G R Thomas, L Willingale, V Yanovsky and K Krushelnick. Energetic neutron beams generated from femtosecond laser plasma interactions. *Appl. Phys. Lett.* 102, 124101 (2013).

3. C Zulick, **A Raymond**, A McKelvey, V Chvykov, A Maksimchuk, A G R Thomas, L Willingale, V Yanovsky and K Krushelnick. Target surface area effects on hot electron dynamics from high intensity laser–plasma interactions. *New Journal of Physics* 18, 063020 (2016).

Contents

List of Figures

List of Abbreviations

AFR Angular Filter Refractometry

AIA Atmospheric Imaging Assembly

ASE Amplified Spontaneous Emission

BL Beam Line

CCD Charge Coupled Device

CID Charge Injection Device

CPA Chirped Pulse Amplification

CUOS Center for Ultrafast Optical Science

DIXI Dilation X-ray Imager

DM Deformable Mirror

DPM Double Plasma Mirror

EPPS Electron Proton Positron Spectrometer

EMHD Electron Magnetohydrodynamics

EUV Extreme UltraViolet

FWHM Full Width at Half Maximum

HERCULES High Energy Repetitive CUos LasEr System

IP Image Plate

JLF Jupiter Laser Facility

LLE Laboratory for Laser Energetics

LLNL Lawrence Livermore National Laboratory

LPI Laser Plasma Interactions

LTE Local Thermodynamic Equilibrium

MCP Micro-Channel Plate

MHD Magnetohydrodynamics

MR Magnetic Reconnection

MRX Magnetic Reconnection Experiment

OAP Off Axis Parabola

OPA Optical Parametric Amplification

OPCPA Optical Parametric Chirped Pulse Amplification

OU-ESM Osaka University Electron Spectrometer

PIC Particle-In-Cell

PPC Particles Per Cell

PPPL Princeton Plasma Physics Laboratory

PSF Point Spread Function

PSL Photostimulated luminescence

RHESSI Ramaty High Energy Solar Spectroscopic Imager

ROSS Rochester Optical Streak System

SCI Spherical Crystal Imager

SPC Single Photon Counter

TCC Target Chamber Center

TNSA Target Normal Sheath Acceleration

UFXRSC Ultrafast X-Ray Streak Camera

VFP Vlasov-Fokker-Planck

XPW Cross-Polarized Wave (Generation)

XRPHC X-Ray Pinhole Camera

ZVH Zinc Von Hamos (Spectrometer)

Abstract

Magnetic reconnection is a fundamental plasma process involving the transfer of magnetic potential energy to plasma kinetic energy through changes in the magnetic field topology. Results are presented of experimental measurements as well as numerical modeling of relativistic magnetic reconnection driven by short-pulse, high-intensity lasers that produce relativistic plasma along with extremely strong magnetic fields. Evidence of fast magnetic reconnection was identified by the plasma's x-ray emission patterns, changes to the electron energy spectrum, optical probing techniques, and by measuring the time over which reconnection occurs, while numerical modeling suggests the process occurs within the relativistic regime wherein the magnetic energy density exceeds the electron rest mass energy density. Accessing these conditions in the laboratory may allow for further investigation to provide insight into previously inaccessible regimes relevant to space and astrophysical plasmas.

Chapter 1

Introduction

1.1 Magnetic Reconnection

For several decades, the effect of magnetic fields on the dynamics of laser produced plasmas has been of great interest (see [1] and references therein). Quasi-static magnetic fields in the vicinity of a laser focal spot can reach mega-gauss or even giga-gauss magnitudes – approximately the magnetic field strength experienced in the atmospheres of some neutron stars [2]. The interplay of magnetic fields with the plasma in LPI significantly influences the overall plasma dynamics, as it can affect the transport and enable the transfer of potential energy and kinetic energy.

A particularly important phenomenon is magnetic reconnection, which results in a topological rearrangement of magnetic fields in a plasma, whereby the field lines break and reconnect while converting magnetic potential energy to kinetic energy of particles in the plasma. While the theory of reconnection is covered in more depth in Section 2.5, a brief overview of the physics is given below.

The basic geometry of magnetic reconnection is demonstrated in Figure 1.1. Magnetic field lines (frozen to the plasma in the case of large magnetic Reynolds number R_M) are incident from above and below the *separatrix* (i.e., *diffusion region*, reconnection region, or *midplane region*), wherein the field lines reconnect and are expelled outward perpendicularly. While resistive magnetohydrodynamics (MHD) may be used to describe reconnection in some contexts, collisionless or "Hall" MHD must be used when ion and electron motion is allowed

to diverge.

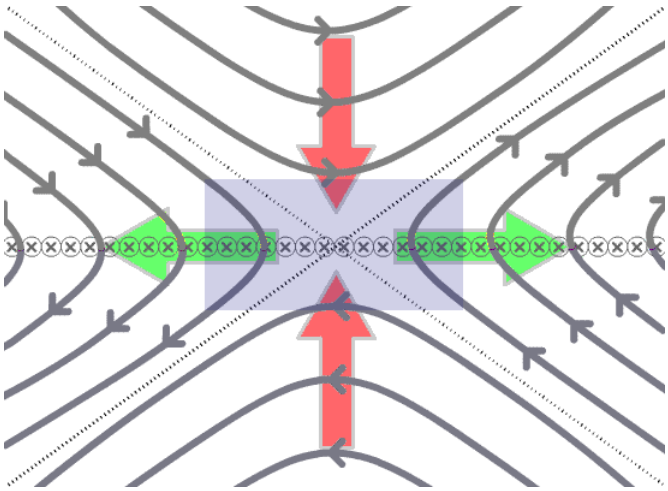

Figure 1.1: A cross-sectional view of magnetic reconnection in a geometry with four magnetic domains and a separatrix in the mid-plane. Plasma flows in from below and from above, carrying oppositely oriented magnetic field lines. The field lines reconnect in the midplane *diffusion region* (shaded rectangle), resulting in expelled plasma and newly formed field lines in the horizontal directions.

The horizontally expelled magnetic fields are associated with *jets* of plasma which can reach super-thermal energies. In the mid-plane, an out-of-plane electric field is produced by the current configuration and by various small-scale spatial and temporal effects.

1.2 Magnetic Reconnection in Nature

Magnetic reconnection is a ubiquitous phenomenon in nature. It has been identified as causing the generation of solar flares [3, 4], and as affecting the energy transfer between these solar flares and planetary magnetospheres [5, 6]. A more extreme example is that of the Crab Nebula, a supernova remnant and pulsar wind nebula in the Taurus constellation; here, observations of extremely energetic γ rays indicate the acceleration of ultra-relativistic electron-positron pairs over the span of days, which is widely attributed to magnetic reconnection occurring in the relativistic regime [7] in an electron-positron plasma.

1.2.1 Solar Flares

Solar flares represent the most powerful, explosive phenomenon within our solar system, and indeed the concept of magnetic reconnection has been used to explain their origin and behavior [8]. As the solar atmosphere is impossible to probe directly, the magnetic field dynamics are inferred from measurements of the electromagnetic spectrum (including X-rays and gamma rays), as well as from tracking the coronal plasma behavior, as the magnetic fields are frozen to the plasma in this regime wherein the magnetic Reynolds number R_M, the estimate of the relative effects of advection or induction of a magnetic field to that of magnetic diffusion, significantly exceeds unity.

A solar flare is a short-lived bright flash of electromagnetic radiation originating near the Sun's surface, comprised of a broad emission spectrum and capable of releasing up to 6×10^{25} J of energy [9]. The flare also ejects plasma of electrons, ions, and neutral atoms through the solar corona and into space; such ejections from the Sun reach the Earth within one or two days.

A flare occurs when accelerated particles interact with the coronal plasma, the acceleration itself being caused by magnetic reconnection. The reconnection occurs within solar *arcades*: closed loops of magnetic field lines, which collide and reconnect, releasing massive amounts of energy in the process. The process also results in a helix of disjointed field lines, which rapidly expand outward forming a *coronal mass ejection*: a massive burst of plasma and magnetic energy emitted from the solar corona which typically accompany solar flares [10].

Visual evidence of magnetic reconnection occurring between these closed coronal loops of magnetic field lines has been gathered from satellites such as Lockheed Martin Solar and Astrophysics Laboratory's Atmospheric Imaging Assembly (AIA), which images the Sun through ten individual spectral channels covering extreme ultraviolet (EUV), ultraviolet, and visible light [11]. Additional X-ray imaging and spectroscopic acquisition have been enabled by NASA's Ramaty High Energy Solar Spectroscopic Imager (RHESSI) [12]. The dynamics of magnetic reconnection on the solar surface is demonstrated in Figure 1.2, showing the merging of discrete loops within a mid-plane where the loops disappear; in this same region,

an X-shaped structure formed and can reach temperatures of 10^7 K [4]. Newly formed hot loops are then formed into two groups, which are expelled from the mid-plane region due to magnetic tension forces.

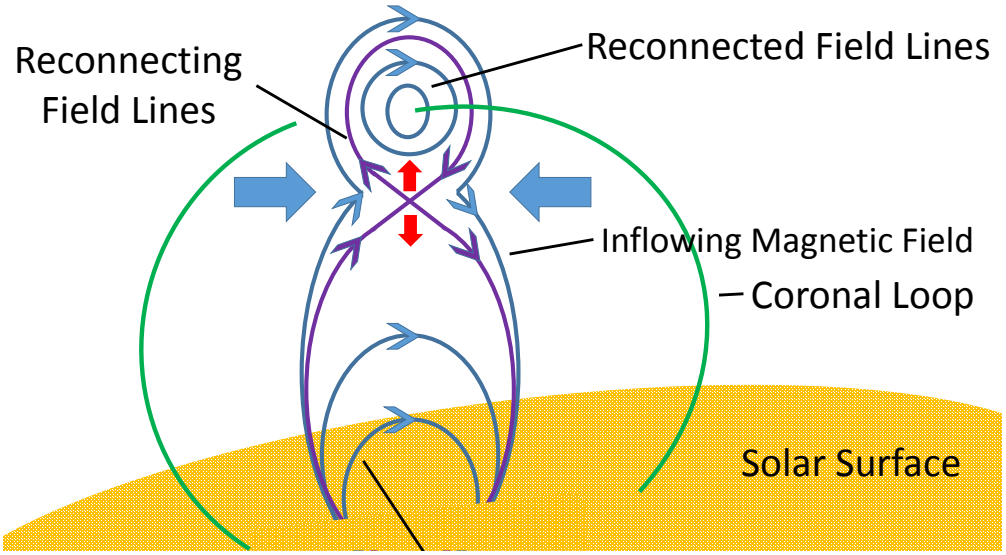

Figure 1.2: A diagram of solar flare generation. Discrete loops merge and reconnect within the mid-plane region, with inflowing plasma labeled with blue arrows and outflowing plasma labeled with red arrows. Newly formed loops are expelled into space via magnetic tension forces.

1.2.2 Planetary Magnetosphere

A planet's magnetosphere is the surrounding region in space where charged particles are confined by the planet's magnetic field. Within the Earth's magnetosphere is the magnetopause and magnetotail, defined as the boundary where the planetary magnetic field balances that from the solar wind, and the region contained within this boundary, respectively. The Earth's magnetic field lines may reconnect with those from the Sun; this allows the release of energy stored in the Earth's magnetic tail and injects charged particles into the magnetosphere, leading to the formation of auroral substorms. Figure 1.3 demonstrates the geometry of the Earth's magnetosphere.

Evidence of reconnection occuring in the Earth's magnetotail has been collected by the Wind spacecraft [6], which detected tailward-directed jets of protons. The spacecraft traveled

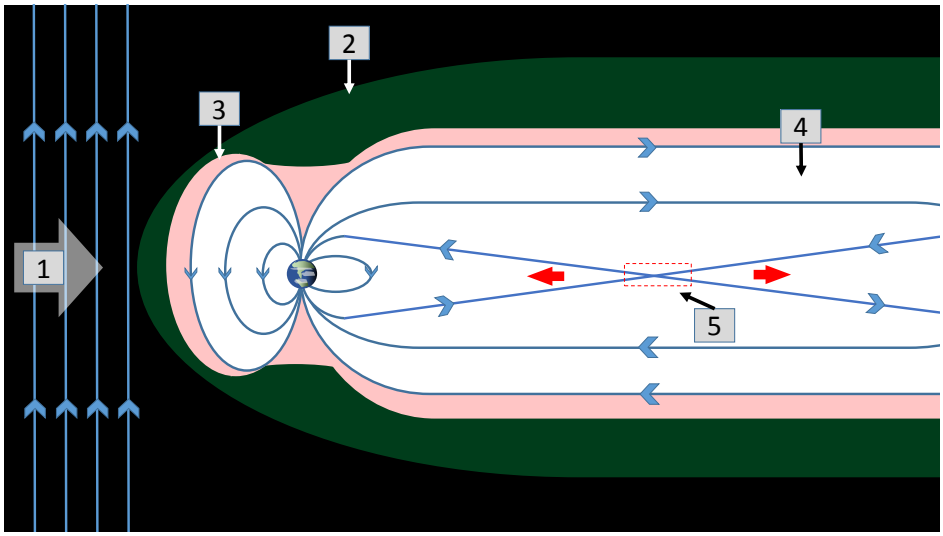

Figure 1.3: A diagram of the Earth's magnetosphere. (1) Solar magnetic field lines are incident from the left. (2) A bow shock forms, where the solar wind speed decreases. (3) The magnetopause, where pressure from the Earth's magnetic field balances the solar wind pressure. Magnetic reconnection occurs between the solar magnetic fields and the Earth's dayside magnetopause. (4) The magnetotail, being an extension of the Earth's magnetosphere. (5) An X-point forms in the magnetotail, where magnetic reconnection takes place. Jets of energetic particles are expelled from this region.

through the ion diffusion region of the X-line depicted in Figure 1.3 and detected a reversal of the proton flow.

1.2.3 High-Energy Astrophysical Systems

Generally, it is theorized that relativistic jets and pulsar winds emanating from gamma-ray bursts and blazars (compact quasi-stellar radio sources at the center of giant active galaxies) are emitted by hydro-magnetic processes. A rotating compact astrophysical object or accretion disk has a strong magnetic field, which may serve to convert the rotational energy to relativistic outflows. Jets may be prone to MHD instabilities due to the tightly wound magnetic field, which may lead to energy conversion via magnetic reconnection [13]. Magnetic potential energy dissipation by magnetic reconnection has often been invoked to account for the non-thermal spectral signatures from pulsar wind nebulae [14], jets emanating from active galactic nuclei [15], and gamma-ray bursts [16].

The Crab nebula, a supernova remnant and nebula powered by pulsar wind, is a specific

astrophysical example of such a situation involving *relativistic* magnetic reconnection; characterized by the involvement of relativistic plasma and a large value of $\sigma \equiv B^2/\mu_0 n_e m_e c^2$ (the ratio of the magnetic energy of the reconnecting fields to the rest-mass plasma energy density).

At the center of the Crab nebula is the Crab pulsar: a 19-mile diameter neutron star rotating at 30.2 Hz, emitting broadband radiation pulses [17]. Astrophysical observations of the pulsar reveal gamma-ray bursts with short durations of $\sim 10^{5.5}$ seconds (compared to the nebula's dynamic timescale of years, high luminosities of $10^{36.6}$ ergs s^{-1}, and high photon energies of 100 MeV [18–21], which may be explained as resulting from randomly oriented relativistic plasma jets originating from magnetic reconnection events [7]. Another possibility for the observed phenomena is acceleration by the pulsar wind termination shock [22, 23]. However, because shock acceleration of particles is likely inefficient in magnetically dominated flows [24], reconnection may be responsible for high energy particle acceleration and high energy radiation production in these systems.

By performing measurements of relativistic reconnection in a laboratory setting, numerical models can be tested in this regime and astrophysical scalings can potentially be inferred.

1.3 Laboratory Reconnection

Magnetic reconnection is an important phenomenon in laboratory plasmas, as a plasma invariably tends to relax to a lower-entropy state via reorganization of the global magnetic field topology, one such vehicle being reconnection. In dedicated nuclear fusion research involving current-carrying plasmas (including the tokamak, reversed field pinch schemes, the spheromak, etc.), reconnection plays a large role in forming a basic equilibrium topology and in affecting the details of the discharge. Rapid changes in the plasma current configuration associated with rapid reconnection are common. As these changes can be undesirable (for example the case of *sawtooth relaxation* in tokamaks), extensive studies have been performed to determine the dynamics of these processes.

Because of the importance of this phenomenon, there have been a number of dedicated experiments designed to *drive* reconnection; i.e., by manufacturing a reconnection layer by

driving antiparallel magnetic fieldlines into a neutral current sheet. The benefit of dedicated experiments is in allowing fine-resolution probing of the plasma structure, which is often impossible in current-carrying fusion plasmas. Such dedicated experiments are often performed not to reproduce astrophysical conditions, but to explore the basic science of reconnection itself. Two means by which dedicated reconnection experiments are performed will be briefly described: the Magnetic Reconnection Experiment (MRX) device, built at Princeton Plasma Physics Laboratory (PPPL); and laser-plasma experiments, whereby two pulses are focused in proximity and generate antiparallel magnetic fields in the midplane.

1.3.1 Controlled Drive

Multiple dedicated experimental apparatuses for controlled drive reconnection exist, but the first dedicated device was the MRX machine. Built at PPPL in 1995 by Yamada et al. [25], the MRX generates a quadrupole magnetic field configuration, followed by a programmed magnetic fieldline evolution; antiparallel fieldlines merge according to a speed defined by an external electric field. As depicted in Figure 1.4, MRX uses toroidally-shaped flux cores; within these flux cores are coil windings, into which programmed currents are pulsed that generate annular plasmas. Following the plasma generation, the coils are again pulsed with currents which drive magnetic reconnection. By utilizing an array of high-frequency magnetic fluctuation probes, the evolution of the magnetic field lines can be monitored.

Experiments on the MRX have focused on connecting small-scale reconnection layer characteristics to global plasma properties [27]; the reconnection rate has also been calculated as a function of plasma parameters, and compared to models [28]. Two-fluid signatures have been identified during fast reconnection experiments on the MRX [29], lending support to the theory that Hall effects originating from two-fluid dynamics significantly contribute to the often-observed enhanced reconnection rate compared to that predicted by the Sweet-Parker model (presented in Section 2.5.1) [30] due to resistive effects.

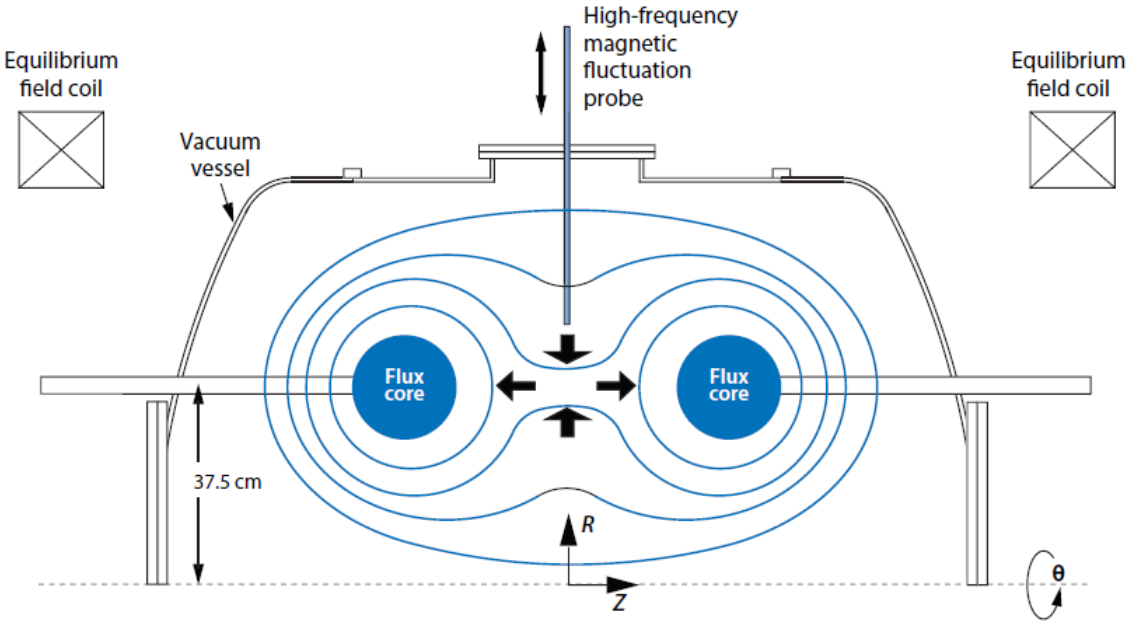

Figure 1.4: The Magnetic Reconnection Experiment (MRX) experimental schematic with magnetic contours, reproduced with permission from [26].

1.3.2 Laser-Plasma Experiments

The original work presented in this thesis is related to magnetic reconnection driven by two sources of laser-generated plasma, in a regime characterized by *short* pulses (of picosecond-scale duration or less) and relativistic focused intensity $O(10^{19}$ Wcm$^{-2})$. Preceding this work, experiments investigating laser-plasma based reconnection were limited to kJ/ns-class lasers, focused to moderate intensities of $O(10^{14-15}$ Wcm$^{-2})$.

Dual-laser driven reconnection experiments were first accomplished with pulses within the kiloJoule/nanosecond regime, focused to moderate intensities. The common configuration involved the irradiation of a thin metallic or plastic layer with the two beams focused with beam separation on the order of millimeters or less. In this regime, azimuthal magnetic fields are formed by the bulk ion motion or hot electron flows, and advect outward at hydrodynamic speeds while frozen to the plasma. In the midplane between the focal spots, the approaching magnetic fields are oppositely oriented, and driven reconnection occurs.

The main signatures of reconnection reported from these experiments involve one or

more of the following features: 1) a null region of the magnetic field in the midplane, 2) the formation of plasma outflows in the form of jets, 3) measurements of increased electron plasma temperatures in the midplane region, and 4) a change in the magnetic field topology consistent with reconnecting magnetic field lines.

P. M. Nilson, et al. (2006) [31] and L. Willingale, et al. (2010) [32] demonstrated clear evidence of reconnection at the VULCAN facility (Rutherford Appleton Laboratory). Two beams (1 ns pulse duration, $I = 10^{15}\mathrm{Wcm}^{-2}$) were focused with varying focal spot separation onto aluminum or gold planar targets. Optical probing demonstrated high velocity, collimated jets of plasma outflow from reconnection. Thomson scattering was used to determine the electron plasma temperature within the midplane region, and found evidence of that they were heated to high temperature by the reconnection process.

C. K. Li, et al. (2007) [33] utilized time-gated proton radiography to reveal quantitative field maps of changing magnetic field topology during reconnection between fields produced by up to 4 laser pulses.

Jiayong Zhong, et al. (2010) [34] produced two laser focal spots with $I \sim 5 \times 10^{15}\mathrm{Wcm}^{-2}$ focused onto an aluminum target. A copper foil was placed such that an outflow jet from the reconnection process would intercept the foil and cause heating. An X-ray pinhole camera recorded emissions from the copper foil, corresponding to jets with an Alfvenic speed of $400 \pm 50\mathrm{kms}^{-1}$.

Quan-Li Dong, et al. (2012) [35] reported collimated electron jets from reconnection between two $I \sim 5 \times 10^{15}\mathrm{Wcm}^{-2}$ pulses, with the reconnection region centered in a gap between the focal spots. The energy spectrum of the jet particles were found to exhibit a power-law scaling.

G. Fiksel, et al. (2014) [36] observed magnetic reconnection between colliding magnetized plasmas. The target configuration involved oppositely placed plastic targets, with the two 1.8 kJ / 2 ns pulses incident upon the inner faces of the targets. An external X-type magnetic field is applied between the targets, with $B_{max} = 8$ Tesla. Proton radiography measured the collision of magnetized ribbons, which stagnate and reconnect in the midplane.

M. J. Rosenberg, et al. (2015) [37] utilized proton probing to observe reconnection features such as fast outflow jets and the formation of a stable current sheet in strongly

driven laser-produced plasma experiments. The outflow jets were measured to be super-Alfvenic ($V \sim 20V_A$) indicating collisionless reconnection early in the reconnection process, while the absence of jets and the stability of the magnetic fields later in time imply a slowing down of the reconnection process, resulting in a change of the plasma conditions to collisional behavior. It was thus established that even in a strongly driven regime, powerful plasma inflows are not sufficient to force complete magnetic field reconnection.

M. J. Rosenberg, et al. (2015) [38] utilized proton probing to study asymmetric magnetic reconnection between two pulses arriving with a temporal delay between them. This effectively shifted the reconnection region toward the focal spot corresponding to late arrival, and resulted remarkably similar reconnection dynamics. The reconnection rate was seen to be nearly equal in both cases, which 2D PIC simulations confirmed.

A recent series of large-scale computational simulations of magnetic reconnection in the kiloJoule/nanosecond regime found that the reconnection is mediated by the Hall effect with significant pressure gradient contributions [39]. In the same work, it was found that electrons are accelerated to energies an order of magnitude greater than the ambient plasma thermal energy, and that the spectrum of accelerated electrons is that of a hard power law $dN/d\gamma = \gamma^{-p}$ where $p = 5.3$.

While laser-driven magnetic reconnection is a relatively new field, a large body of experimental, theoretical, and computational work has resulted due to its relevance to astrophysics and magnetic fusion devices [40, 41]. As can be seen, a commonality among these experiments is the use of nanosecond-duration pulses focused to non-relativistic intensities. This is sufficient to study many fascinating phenomena, and the experiments are less sensitive to slight beam-mistiming compared to the use of short pulses. The benefit of performing reconnection with short, relativistic pulses, however, is both to explore a new regime of reconnection, and the ability to make connections to astrophysical phenomena which involve relativistic plasma.

1.4 Thesis Overview

This thesis describes experiments conducted at three major laser/plasma science facilities (HERCULES, Omega EP, and Titan) involving magnetic reconnection driven by high-magnitude magnetic fields carried by relativistic electrons. First, a review of theoretical background material is given in Chapter 2 and an overview of the experimental methods is provided in Chapter 3. The research is organized with regard to radiation diagnostics of reconnection (Chapter 4), temporal duration measurements (Chapter 5), and particle diagnostic techniques (Chapter 6). Following these will be a summary of the results (Chapter 7).

Chapter 2

Theoretical Background

2.1 High Powered Lasers

Until the development of chirped pulse amplification (CPA) [42] by Gerard Mourou, *et al.*, in the 1980s, achievable focused laser intensities were limited to non-relativistic ($I\lambda^2 < 10^{18}$ $\mathrm{Wcm}^{-2}\mu m^2$) values due to the nonlinear self focusing effect in the laser amplification media. CPA allows for this limit to be bypassed by temporally stretching (and thus reducing the intensity of) the pulse before amplification, followed by subsequent recompression. This has since allowed laser intensities to exceed $10^{22}\mathrm{W/cm}^2$ [43].

Modern laser systems also utilize Optical Parametric Chirped-Pulse Amplification (OPCPA), a variation of CPA which takes advantage of crystalline materials lacking inversion symmetry; in this scheme, a pulse is amplified using a parametric nonlinearity and a pump wave following CPA temporal stretching. This method leads to several advantages as compared to the use of typical amplification methods, including the requirement for fewer amplification stages for the same extracted gain, amplification at a wider range of wavelengths, weaker thermal effects such as thermal lensing, and the reduction of power loss via amplified spontaneous emission [44–46].

2.1.1 Chirped Pulse Amplification

The intensity reached by high powered laser pulses is sufficient to lead to detrimental effects when propagating through amplification media, such as pulse distortion or damage to the gain media. To prevent this, repetitive CPA is employed. Before the laser is passed through a gain medium, the pulses are frequency-chirped and the pulse duration is increased using a *stretcher* such as a grating pair or an optical fiber. This effectively reduces the pulse's peak intensity to a point where deleterious effects during propagation through the gain media are avoided. Following amplification the pulse is sent through a *compressor* system such as another grating pair, which removes the chirp and temporally compresses the pulse to near its initial duration.

To achieve a short pulse, one must consider the spectral bandwidth. A Fourier analysis of an ideally compressed pulse results in a relationship between the pulse duration τ and the spectral bandwidth $\Delta\omega$:

$$\Delta\omega \cdot \tau \geq 2\pi C_B \tag{2.1}$$

where for a Gaussian pulse, C_B=0.441. A 40 fs pulse such as that from the HERCULES laser therefore requires 11 THz of frequency bandwidth, or 23.5 nm at 800 nm from $\Delta f = c\Delta\lambda/\lambda^2$. If the pulse is not ideal but instead has linear chirp whereby the frequency varies with time, then the time-bandwidth product is expressed as

$$\Delta\omega \cdot \tau = 2\pi C_B \sqrt{1 + (b/a)^2} \tag{2.2}$$

where $a = 2\ln(2)/\tau^2$ and b is the linear chirp. Thus, the pulse duration increases for $b > 0$ even if the bandwidth remains constant. This is the means by which increased pulse duration is achieved in CPA schemes; a chirp is introduced to a pulse, stretching its duration and therefore reducing its peak power. The pulse may then be further amplified while remaining below the damage threshold of the amplification media, followed by chirp removal and restoration of approximately the original pulse duration.

Chirp may be added to a pulse by transporting it through a dispersive medium such as an optical fiber, but a more convenient method is the utilization of a grating pair. This is

due to the fact that material dispersion is typically positive, while grating pairs impart negative dispersion – thereby allowing the possibility to compensate for dispersion accumulated throughout the laser chain.

On the HERCULES system, a double-pass Treacy grating pair [47] is used for beam compression; the group delay dispersion for this double-pass system is given by

$$\phi'' = -\frac{G\lambda}{\pi c^2} \frac{(\lambda/d)^2}{[1-(\sin\gamma - (\lambda/d)^2]^{3/2}} \tag{2.3}$$

where d is the grating line spacing, λ is the laser central wavelength, and G, γ, and θ are defined in Figure 2.1.

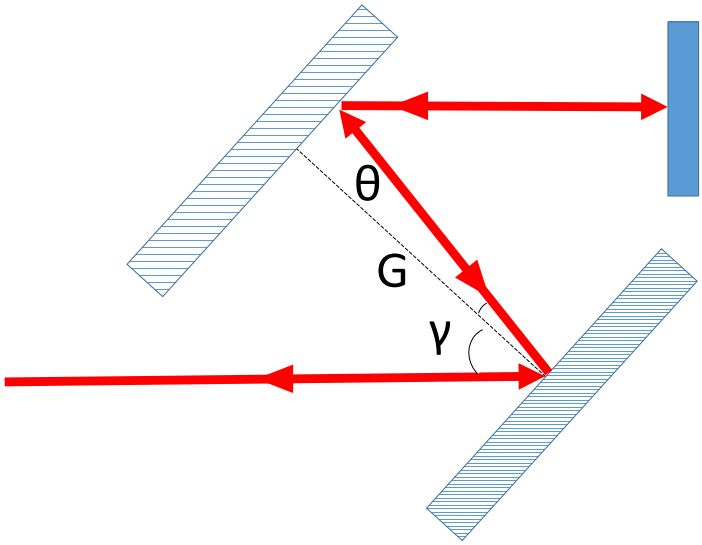

Figure 2.1: A basic schematic of the Treacy grating pair, with grating separation G, incident angle γ, and reflectance angle of θ.

2.2 Overdense Laser / Plasma Interactions

The process of short-pulse laser irradiation of initially solid-density targets (such as metallic foils, plastics, and glass) involves many physical mechanisms, and is not fully described by any given model. Thus, a variety of considerations are involved in describing the full interaction.

Upon irradiation by a short-pulse laser, an initially solid-density target will become ionized by the laser pre-pulse, creating a density *ramp* which extends from vacuum to solid density. When the density exceeds the *critical density* ($n_c = \omega_L^2 \epsilon_0 m_e / e^2$) corresponding to the laser, the plasma is known as *overdense*.

The main pulse interacts with this density ramp, transferring energy primarily to the generation of hot electrons almost entirely by a combination of *Brunel* absorption [48], *resonance* absorption [49], and ponderomotive acceleration [50]. The behavior of the expanding plasma will lead to the generation of strong magnetic and electric fields, which will also affect the transport of electrons through the target.

2.2.1 Resonance Absorption

Consider a light wave incident upon a plasma slab with density $n_e(z)$ and an angle θ between the propagation vector $\mathbf{k}$ and the density gradient direction $\hat{z}$. At the plasma-vacuum interface ($z = 0$), $(k_x, k_y, k_z) = (0, \frac{\omega}{c}\sin\theta, \frac{\omega}{c}\cos\theta)$ and the light wave propagates in the $z - y$ plane. The light wave propagation within the plasma depends on whether its electric field $\mathbf{E}$ is *in* or *out* of the plane of incidence.

If the electric field $\mathbf{E}$ lies within the plane of incidence ($\mathbf{E} \cdot \nabla n_e \neq 0$), the light is known as p-polarized and an oscillation of electrons along the direction of the density gradient exists. These oscillations can be resonantly enhanced by the plasma, with energy from the incident light being transferred to electron plasma waves; this is known as *resonance absorption* [49].

Following the derivation outlined by Kruer (1988, p. 39) [51], begin with the electric field expressed as $\mathbf{E} = E_y \hat{y} + E_z \hat{z}$. Poisson's equation yields

$$\nabla \cdot (\epsilon \mathbf{E}) = 0 \tag{2.4}$$

where $\epsilon - 1 - \omega_{pe}^2(z)/\omega^2$. Applying the product rule to Equation 2.4,

$$\nabla \cdot \mathbf{E} = -\frac{1}{\epsilon}\frac{\partial \epsilon}{\partial z} E_z \tag{2.5}$$

from which a resonant response is evident when $\epsilon = 0$ (*i.e.*, at the critical surface). At the critical surface, the charge density fluctuation imposed by the laser matches the frequency

at which the plasma resonantly responds. The energy transfer to the excited plasma wave can be calculated to be

$$I_{abs} = f_A \frac{\epsilon E_{FS}^2}{2} \tag{2.6}$$

where E_{FS} is the electric field magnitude in free space, and f_A is the fraction of absorbed energy of the incident beam into excited waves at the critical density, given approximately by $f_A \approx \phi^2(\tau)/2$ where $\phi(\tau)$ is the resonance function. The latter is dependent on the angle of incidence θ and the plasma density scale length $L = n_e/\frac{\partial n_e}{\partial x}$:

$$\phi(\tau) \approx 2.3\tau \exp(-2\tau^3/3), \tau \equiv (\omega L/c)^{1/3} \sin\theta. \tag{2.7}$$

If the density profile is approximated as linear, the absorption is maximized at an angle given by $\theta_{opt} = \sin^{-1}[0.8(c/\omega L)^{1/3}]$.

2.2.2 Brunel Absorption

While resonance absorption is relevant for relatively long plasma density gradients, it breaks down in the case of very steep gradients. In this case, the resonantly driven plasma wave with field amplitude E_p at the critical surface will be approximately matched by the incident laser field E_L; electrons undergo oscillations in the direction of the plasma gradient with amplitude $\approx eE_L/m_e\omega^2 = v_{osc}/\omega$; if this length is less than the scale length L of the plasma, then the conditions for resonant excitation are not met.

Despite this, electrons in the sharp density gradient *can* extract energy from the laser field. Brunel described this as *not-so-resonant resonance absorption* [48] as follows: a thermal electron near the edge of the steep plasma/vacuum interface may be dragged from the Debye sheath and into vacuum by the laser field during its cycle; when the cycle reverses, the electron is accelerated into the plasma. The electron may propagate sufficiently deep within the plasma that the laser field is shielded (at depths greater than the skin depth c/ω), so that the electron keeps its imparted energy and distributes it to the plasma through collisions.

Gibbon (2007, p. 153) [52] outlines a *capacitor approximation* model for the absorption, in which the magnetic field of the incident wave is ignored. Electrons acquire a velocity

$v_d \approx 2v_{osc}\sin\theta$ from the laser field, where v_{osc} is the electron quiver velocity. The fractional absorption rate is found to be

$$\eta_\alpha = \frac{4a_0}{\pi}\frac{\sin^3\theta}{\cos\theta} \tag{2.8}$$

where $a_0 = v_{osc}/c$. Improvements to this model involve taking into account laser field reflectivity and relativistic electron velocities. With $\gamma = (1 + v_d^2/c^2)^{1/2}$ and the electron kinetic energy equal to $U_k = (\gamma - 1)m_e c^2$, an implicit solution is derived:

$$\eta_\alpha = \frac{1}{\pi a_0} f\left[(1 + f^2 a_0^2 \sin^2\theta)^{1/2} - 1\right]\tan\theta, \tag{2.9}$$

with $f \equiv 1 + (1 - \eta_\alpha)^{1/2}$. Despite that this solution is implicit, limiting forms can be found. Assuming strong irradiance such that $f a_0 \sin\theta >> 1$, then

$$\eta_{real} = \frac{4\pi\alpha'}{(\pi + \alpha')^2} \tag{2.10}$$

where $\alpha' = \sin^2\theta/\cos\theta$. This function peaks at an angle $\theta_{opt} = 73.06°$.

2.2.3 Thermoelectric Effect

Associated with the electron plasma currents induced by LPI are magnetic fields which may assume large magnitudes up to O(MG).

One such mechanism is the *Biermann battery* effect (*i.e.,* the thermoelectric effect), whereby non-parallel gradients in electron plasma temperature and density result in a time-varying magnetic field [53]:

$$\frac{\partial B}{\partial t} = \frac{\nabla T_e \times \nabla n_e}{e n_e}. \tag{2.11}$$

These typically assume magnitudes O(MG) and result in strong magnetic pressure which may pinch and elongate the plasma in the vicinity of the focal spot. The geometry for the Biermann battery effect is demonstrated in Figure 2.2.

This effect occurs on hydrodynamic timescales, and can continue long after the laser pulse has ended. The magnitude of the field may be estimated as follows (assuming the density

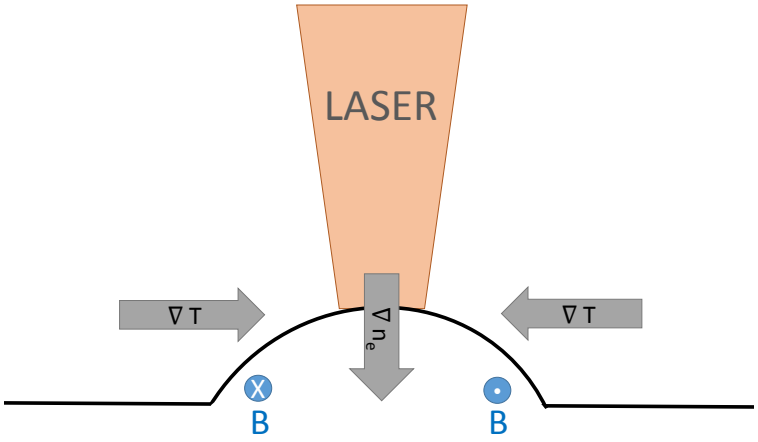

Figure 2.2: A diagram depicting the Biermann battery mechanism of magnetic field generation, whereby non-parallel gradients in plasma density and temperature induce a time-varying azimuthal magnetic field.

gradient is primarily directed along the target normal) [54]:

$$B \approx 2 \left(\frac{\tau}{\text{ps}}\right) \left(\frac{k_B T_e}{\text{keV}}\right) \left(\frac{L_T}{\mu\text{m}}\right)^{-1} \left(\frac{L_{n_e}}{\mu\text{m}}\right)^{-1} \text{MGauss} \tag{2.12}$$

where L_T is the transverse temperature gradient and L_{n_e} is the transverse density gradient.

2.2.4 Relativistic Surface Electrons

In the case of a relativistically focused ($I\lambda^2 > 10^{18} W cm^{-2} \mu m^2$), short-pulse laser incident upon a sharp plasma density gradient, an azimuthal magnetic field is generated but by a distinctly separate mechanism. Laser energy is absorbed into a nearly isotropically expanding, relativistic electron population, which travels into the target as well as into the vacuum [55]. The initial vacuum-propagating electrons set up a sheath field which confines further outward-generated electrons to the target surface. While a cold *return* current cancels out the hot electron current propagating into the target, un-neutralized current sheets propagate along the target surface. A surface return current is formed from the denser regions of the plasma, resulting in oppositely directed surface current sheets. A magnetic field

is generated between the sheets, and expands radially along with the fast surface electrons at near the speed of light [56].

A simple, 2D model for the magnetic field generation can be formulated as follows (following the derivation presented in [56]): a circular loop with radius r sits a distance z_0 above the target surface, with the center axis aligned with the focal spot. Further, target-normal displacement current is neglected and azimuthal symmetry is assumed. Ampere-Maxwell's equation applied to this loop yields $2\pi r B_\theta = \mu_0 \epsilon_0 \int_S \partial_t \mathbf{E} \cdot d\mathbf{S} = \frac{2\pi}{c^2} \partial_t \int_0^r E_z(r', z, t) r' dr'$, where ∂_t is the partial time derivative. By invoking Gauss' law within a cylinder with the previous circular loop defining one end and the other at $z = 0$, $B_\theta(r, z, t) = -\mu_0 \int_z^\infty j_r(r, z', t) dz'$. In this geometry, B_θ is thus approximately constant until the electrons slow to non-relativistic speeds. In 3 spatial dimensions, however, B_θ is expected to fall off more rapidly (as r^{-1}).

The PIC simulations discussed in [56] indicate that the azimuthal magnetic field occupies a thickness equal approximately to the plasma scale length (or for the case of zero scale length, $\approx$ the plasma skin depth), and its structure assumes the form

$$B(r,t) = \begin{cases} B_0 & \text{for } r < r_0 \\ B_0 r_0 / r & \text{for } r_0 \leq r \leq r_s(t) \\ 0 & \text{for } r > r_s(t) \end{cases} \tag{2.13}$$

where B_0 is the maximum magnetic field magnitude, which is constant until a radius r_0 equal to approximately the focal spot radius. Beyond this value, the magnetic field varies as $1/r$ as $r_s(t) = ct$. A maximum stagnation radius r_s is estimated in [56] as $r_s \approx r_0 \exp\left[2 f U_p / (\pi^3 m_e c^2 n_c r_0^2 \lambda_0)\right]$, where $f U_p$ is the fraction of the laser energy transferred to the magnetic field via hot electron generation, and λ_0 is the laser wavelength. Typical values for a sub-picosecond laser pulse focused to relativistic intensity are $B_0 = O(100\text{ MG})$ and $r_s = O(100\ \mu\text{m})$.

2.2.5 Hot Electron Generation

In addition to heating a large population of electrons to a temperature T_e, most laser absorption mechanisms result in additional heating of a fraction of these to energies greatly

exceeding T_e. This is thought to be due to the stochastic nature of the acceleration mechanism, involving fluctuations in the electron trajectories, or due to more than one acceleration mechanism acting at the same time. The result is a bi-Maxwellian electron distribution featuring thermal electrons with temperature T_e and *hot* electrons with a higher temperature T_h.

In the case of *long* pulses, the laser and plasma are assumed to have reached a pressure balance, implying that the plasma density profile at the critical surface adapts according to the laser pressure and temperature at this point. This assumption is reasonable since, unlike the case of *short* pulse lasers, the ions have time to respond to the laser pressure during the timescale of absorption.

Particle-in-cell (PIC) simulations (Forslund, Kindel and Lee, 1977 [57]) with pressure balance conditions pre-imposed resulted in a hot electron temperature scaling of

$$T_h \approx 14(I_{16}\lambda_\mu^2)^{1/3}T_e^{1/3}\text{keV} \tag{2.14}$$

where T_e is the Maxwellian electron temperature and I_{16} is the laser intensity normalized to 10^{16} Wcm^{-2}, T_e is the cold, bulk electron temperature in keV, and λ_μ is the laser wavelength in μm. For long pulse lasers, this expression agrees well with experiments over a large range of $I\lambda^2$ for moderate intensities ([58]).

In the case of *short*-pulse lasers, the timescale of the interaction is too short for a pressure balance to be reached, and the density interface is much steeper. As the laser has access to a high density electron plasma, which yields a variety of absorption mechanisms, the description of hot electron generation is similarly complex. However, empirical scaling laws have been developed for the hot electron temperature.

For the case of a short-pulse laser incident upon a steep density profile ($L < 0.1\lambda$), PIC simulations (Gibbon and Bell, 1992 [59]) with fixed ions yield the following expression for the hot electron temperature where Brunel absorption is the primary heating mechanism:

$$T_h \approx 7(I_{16}\lambda_{\mu m}^2)^{1/3}\text{keV}. \tag{2.15}$$

For relativistic intensities (i.e., above 10^{18} Wcm^{-2}), the hot electron temperature may be

related to the ponderomotive potential Φ_p of the standing wave at the plasma/vacuum interface; this may be deduced from considering the $\mathbf{J} \times \mathbf{B}$ absorption mechanism [48], whereby

$$\begin{aligned} T_h &\approx mc^2(\gamma - 1) \\ &\approx 511 \left[(1 + 0.73 I_{18} \lambda_\mu^2)^{1/2} - 1\right] \text{keV} \end{aligned} \tag{2.16}$$

at normal incidence. Further complications may arise if *hole-boring*, a laser-driven deformation of the ion density profile in the plasma, occurs simultaneously; in this scenario, the relativistic $\mathbf{J} \times \mathbf{B}$ heating may be accompanied by additional absorption mechanisms along the sides of the hole [52].

2.3 Generalized Fluid Equations

A fundamental feature of MHD is that if the ideal Ohm's Law applies, two fluid elements that are linked by a magnetic field line at $t = 0$ remain linked for all time (*i.e.*, the magnetic field is frozen to the plasma). The ideal Ohm's law is written

$$\mathbf{E} + \mathbf{v} \times \mathbf{B} = 0. \tag{2.17}$$

A number of effects may lead to the violation of Ohm's Law, generally related to small spatial or temporal scales [60]. When such effects occur in a localized region, the magnetic field lines may reconnect. Taking into account the various violations of the ideal Ohm's Law for a non-relativistic plasma, one form of the generalized Ohm's Law is written:

$$\mathbf{E} + \mathbf{v} \times \mathbf{B} = \eta \mathbf{J} + \frac{1}{ne} \mathbf{J} \times \mathbf{B} - \frac{1}{ne} \nabla \cdot \overleftrightarrow{P} + \mathscr{R}. \tag{2.18}$$

This equation is derived from the electron momentum equation, with $\mathbf{E}$ and $\mathbf{B}$ equal to the electric and magnetic fields, $\overleftrightarrow{P}$ equal to the anisotropic pressure tensor, and $\mathbf{J}$ equal to the electron current. On the right hand side, the first term is due to collisional or anomalous resistivity, the second term is the Hall term and is due to two-fluid effects, the third term is due to large gradients of the electron pressure, and the last term represents frictional and

inertial effects.

In laboratory plasmas such as the spheromak [61], the Hall term is the most significant, while electron fluid velocity gradients contributes the least. This is also the case for the solar corona [62]. But when discussing high-energy astrophysical phenomena, there are two significant differences: 1) the plasma is relativistic, and thus Equation 2.18 no longer applies, and 2) the plasmas are typically electron-positron plasmas, in which case the Hall term vanishes due to the equal masses of the plasma components.

The relativistic, generalized Ohm's Law is presented based on a derivation performed by Kandus, A. *et al.* [63], derived for a multi-component plasma, utilizing a general metric, and in the presence of an arbitrary electromagnetic field. It is expressed in the form of a propagation equation for the electric 3-current $\mathcal{J}$, relating it to the electric field. In the following expression, $\Theta = \nabla^a u_a = D^a u_a$ (the average expansion or contraction of the timelike velocity field u_a, with D being a tensor derivative operator), $\sigma_{ab} = D_{\langle bu_a \rangle}$ (changes in its shape under constant volume), $\omega_{ab} = D_{[bu_a]}$ (rotational behavior of u_a), $v^a_{(i)}$ is the velocity relative to the u_a frame, $\hat{n}_{(i)} = \gamma_{(i)} n_{(i)}$ (the number density), $\hat{M} = \hat{\mu} + \hat{p}$ where μ is the energy density and $\hat{p}$ is the isotropic fluid pressure. Finally, Z is the species charge, E and B are the electric and magnetic fields measured at a fixed position, and $\mathcal{G}$ represents the increase or decrease in the number density of the system (more details on these variables and a detailed derivation are presented in the citation). Hatted variables denote a hidden multiplicative Lorentz factor.

$$\begin{aligned}
\dot{\mathcal{J}}^{\langle a \rangle} = &-\frac{4}{3}\Theta \mathcal{J}^a - (\sigma^a_b + \omega^a_b)\mathcal{J}^b + e\sum_i Z_{(i)} \left(\frac{\hat{n}_{(i)}}{\hat{M}_{(i)}}\right) \rho_{(i)} E_a + e\sum_i Z_{(i)} \left(\frac{\hat{n}_{(i)}}{\hat{M}_{(i)}}\right) \epsilon^a_{bc} \mathcal{J}^b_{(i)} B^c \\
&- e\sum_i Z_{(i)} \left(\frac{\hat{n}_{(i)}}{\hat{M}_{(i)}}\right) \left(\dot{\hat{p}}_{(i)} v^a_{(i)} + D^a \hat{p}_{(i)}\right) - \sum_i Z_{(i)} \hat{n}_{(i)} \dot{u}^a + e\sum_i Z_{(i)} \left(\frac{\hat{n}_{(i)}}{\hat{M}_{(i)}}\right) \mathcal{G}^{\langle a \rangle}_{(i)} \\
&+ e\sum_i Z_{(i)} \left[\mathcal{Q}_{(i)} + \left(\frac{\hat{n}_{(i)}}{\hat{M}_{(i)}}\right) \left(\mathcal{G}_{(i)} - E_b \mathcal{J}^b_{(i)}\right)\right] v^a_{(i)} - e\sum_i Z_{(i)} D_b \left(\hat{n}_{(i)} v^b_{(i)} v^a_{(i)}\right) \\
&+ e\sum_i Z_{(i)} \hat{n}_{(i)} \left(\frac{1}{3}\Theta v^2_{(i)} + \sigma_{bc} v^b_{(i)} v^c_{(i)}\right) v^a_{(i)}. \quad (2.19)
\end{aligned}$$

where $\dot{\mathcal{J}}^{\langle a\rangle}$ is the orthogonally projected time derivative of the 3-current, provided global electric neutrality holds. Familiar terms may be easily identified in the right hand side of Equation 2.19. The first two terms are related to the relative movement of the observer, representing changes in the 3-current by inertial forces. The third term represents the effect of the self-consistent electric field. The fourth term leads to the Hall effect, while the fifth term represents the effects of isotropic pressure variations (embodying the Biermann battery effect). The sixth term vanishes when global electrical neutrality is satisfied, while the seventh term represents the effect of particle collisions leading to momentum transfer from one species to another. The eighth term originates from particle creation/annihilation processes, while the ninth term represents spatial variations in the particle density and velocity, and the tenth and final term accounts for relative inertial effects.

Equation 2.19 is general, allowing for the description of multi-component systems with different particle species (including non-baryons and photons).

The equation can be simplified to describe a relativistic, two-fluid plasma. Introducing the variables $\hat{M} = \hat{M}_+ + \hat{M}_-$ and $\hat{\Delta} = \hat{M}_+ - \hat{M}_+$, we arrive at:

$$\begin{aligned}
\dot{\mathcal{J}}^{\langle a\rangle} = &-\frac{4}{3}\Theta\mathcal{J}^a - (\sigma^a_b + \omega^a_b)\mathcal{J}^b + \frac{4e^2\hat{n}_E^2}{\hat{M}^2 - \hat{\Delta}^2}E^a + \frac{2e\hat{n}_E[\hat{M}(Z_+ + Z_-) - \hat{\Delta}(Z_+ - Z_-)]}{(\hat{M}^2 - \hat{\Delta}^2)(Z_+ - Z_-)}\epsilon^a_{bc}\mathcal{J}^b B^c \\
&- \frac{2[\hat{M}(\hat{\dot{p}}_+ Z_+ - \hat{\dot{p}}_- Z_-) - \hat{\Delta}(\hat{\dot{p}}_+ Z_+ + \hat{\dot{p}}_- Z_-)]}{(\hat{M}^2 - \hat{\Delta}^2)(Z_+ - Z_-)}\mathcal{J}^a - \frac{2e\hat{n}_E}{\hat{M}^2 - \hat{\Delta}^2}\left[\hat{M}(D^a\hat{p}_+ - D^a\hat{p}_-) - \hat{\Delta}(D^a\hat{p}_+ + D^a\hat{p}_-)\right] \\
&\frac{2e\hat{n}_E}{\hat{M} + \hat{\Delta}}\mathcal{G}^{\langle a\rangle}_{ext} - \frac{4e\hat{n}_E}{\hat{M}^2 - \hat{\Delta}^2}\mathcal{G}^{\langle a\rangle}_{-} + \frac{2Z_+\mathcal{G}_{ext}}{(Z_+ - Z_-)(\hat{M} + \hat{\Delta})}\mathcal{J}^a - \frac{2\left[\hat{M}(Z_+ + Z_-) - \hat{\Delta}(Z_+ - Z_-)\right]\mathcal{G}_-}{(Z_+ - Z_-)(\hat{M}^2 - \hat{\Delta}^2)}\mathcal{J}_a \\
&- \frac{(Z_+ - Z_-)\mathcal{G}}{n_E}\mathcal{J}^a + \frac{2[\hat{\Delta}(Z_+^2 - Z_-^2) - \hat{M}(Z_+^2 + Z_-^2)]}{(\hat{M}^2 - \hat{\Delta}^2)(Z_+ - Z_-)^2}E^b\mathcal{J}_b\mathcal{J}^a - \frac{Z_+ + Z_-}{e(Z_+ - Z_-)}D^b\left(\frac{1}{n_E}\mathcal{J}_b\mathcal{J}^a\right) \\
&+ \frac{Z_+^3 - Z_-^3}{e^2\hat{n}_E^2(Z_+ - Z_-)^2}\left(\frac{1}{3}\Theta\mathcal{J}^2 + \sigma^{bc}\mathcal{J}_b\mathcal{J}_c\right)\mathcal{J}^a \quad (2.20)
\end{aligned}$$

where $\mathcal{G}_{\lceil\S\rfloor\sqcup}$ represents the effect of interactions external to the system. This is the relativistic, generalized Ohm's Law, with respect to an Eckart frame, applied to a plasma comprised of two relativistic, charged fluids. The right-hand side terms can be related to their Newtonian simplifications as was done for Equation 2.19.

This expression can be further simplified, for example, by assuming a plasma comprised of one positively and one negatively charged species. In the special case of a particle-antiparticle plasma, and by noting $Z_{\pm} = \pm 1$ and $\hat{M}_{+} = \hat{M}_{-}$, we arrive at

$$\dot{\mathcal{J}}^{\langle a \rangle} = -\frac{4}{3}\Theta\mathcal{J}^{a} - (\sigma_{b}^{a} + \omega_{b}^{a})\mathcal{J}^{b} + \frac{4e^{2}\hat{n}_{E}^{2}}{\hat{M}}E^{a} - \frac{2\hat{\dot{p}}}{\hat{M}}\mathcal{J}^{a} - \frac{4e^{2}\hat{n}_{E}^{2}}{\hat{M}}\mathcal{G}_{-}^{\langle a \rangle} - \hat{M}^{-1}E^{b}\mathcal{J}_{b}\mathcal{J}^{a} + \frac{1}{2e^{2}\hat{n}_{E}^{2}}\left(\frac{1}{3}\Theta\mathcal{J}^{2} + \sigma^{bc}\mathcal{J}_{b}\mathcal{J}_{c}\right)\mathcal{J}^{a}, \quad (2.21)$$

which contains no Hall effect due to the equal particle masses and opposite but equal charges. The only relativistic corrections are an additional component of the Biermann battery term, and a contribution from Joule-heating.

2.4 K_{α} Emission

K-shell emissions have been used to diagnose hot electron spectra and electron angular distributions in high-intensity laser-plasma interactions [64–67], as well as to image the trajectories taken by hot electrons utilizing X-ray imaging systems [68–70]. Their emission is induced by inelastic collisions between fast electrons (with energies exceeding the K-shell binding energy) and other electrons in the K-shell. The K-shell vacancy is short-lived (typically lasting O(fs)) and decays via both radiative and non-radiative de-excitation mechanisms. For mid-Z elements such as copper, there is competition between K-shell fluorescence and the Auger effect [71]. The K-photons of interest in this Thesis are those from copper, the shell diagram for which is provided in Figure 2.3.

The rate of excitation and corresponding K_{α} production can be modeled theoretically and computationally simulated with a hybrid Vlasov-Fokker-Planck-Maxwell code combined with a Bethe model for ionizing collisions [72].

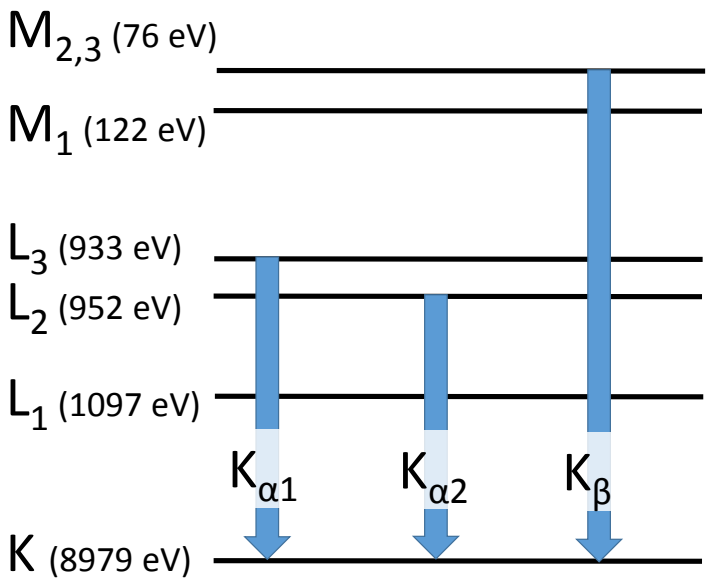

Figure 2.3: A shell-model diagram for a copper atom, demonstrating the energy level transitions which produce K_α and K_β X-rays.)

2.4.1 Collisional Excitation

An electron population with the distribution function $f_e(\mathbf{x}, p, \theta, \phi, t)$ impinges on an ion population (atomic number Z) with density n_i. The rate of single and double hole K-shell excitations per volume are given respectively by Equations 2.22 and 2.24 ([72]):

$$R_{K_1}(\mathbf{x}, t) = 2n_i^* \int \int_\Omega \sin(\theta) \mathrm{d}\theta \mathrm{d}\phi \int_0^\infty p^2 f_e \sigma_K(Z, p)\, v(p) \mathrm{d}p \tag{2.22}$$

$$R_{K_2}(\mathbf{x}, t) = \vec{n}_{K_1} \int \int_\Omega \sin(\theta) \mathrm{d}\theta \mathrm{d}\phi \int_0^\infty p^2 f_e \sigma_K(Z, p)\, v(p) \mathrm{d}p \tag{2.23}$$

where $\sigma_K(Z, p)$ is the cross section for electron excitation for the first electron in the K-shell, $n_i^* = n_i - \bar{n}_{K_1}$ is the ion density minus the density of atoms with single holes in the K-shell, and $\vec{n}_{K_1} = \bar{n}_{K_1} - \bar{n}_{K_2}$.

Per unit volume $\bar{n}_K$, the time derivative of total K-shell vacancies is equal to

$$\frac{\mathrm{d}\bar{n}_K}{\mathrm{d}t} = R_{K_1} + R_{K_2} - \bar{n}_K/\tau_K \tag{2.24}$$

where τ_K is the lifetime of the excited state.

2.4.2 K_α Generation

A relativistically correct expression for ionization cross sections based on the binary encounter Bethe model was produced by Guerra et al. [73].

This modified binary encounter Bethe model (MRBEB) ionization cross section is given by

$$\begin{aligned}\sigma_{\mathrm{MRBEB}} = \frac{4\pi a_0^2 \alpha^4 N}{(\beta_t^2 + D\beta_b^2)2b'} \Bigg\{ \frac{1}{2}\left[\ln\left(\frac{\beta_t^2}{1-\beta_t^2}\right) - \beta_t^2 - \ln(2b') \right] \left(1 - \frac{1}{t^2}\right) \\ +1 - \frac{1}{t} - \frac{\ln t}{t+1}\frac{1+2t'}{(1+t'/2)^2} + \frac{b'^2}{(1+t'/2)^2}\frac{t-1}{2} \Bigg\}\end{aligned} \tag{2.25}$$

where the reduced units are given by

$$\begin{aligned} t &= T/B \\ t' &= T/mc^2 \\ b' &= B/mc^2 \\ \beta_t^2 &= 1 - \frac{1}{(1+t')^2} \\ \beta_b^2 &= 1 - \frac{1}{(1+b')^2} \end{aligned} \tag{2.26}$$

In Equations 2.25 and 2.26, T is the temperature of the impinging electrons, B is the binding energy of the electron to be ionized, D is an empirical function of Z given in [73], N is the occupation number, a_0 is the Bohr's radius ($= 5.29 \times 10^{-11}$m), R is the Rydberg energy ($= 13.6$eV), α is the fine structure constant, c is the speed of light in the medium,

and m is the electron mass. Figure 2.4 depicts the representative qualitative behavior of σ_{MRBEB} as a function of T/mc^2 for a range of K-shell binding energies and constant target atomic number.

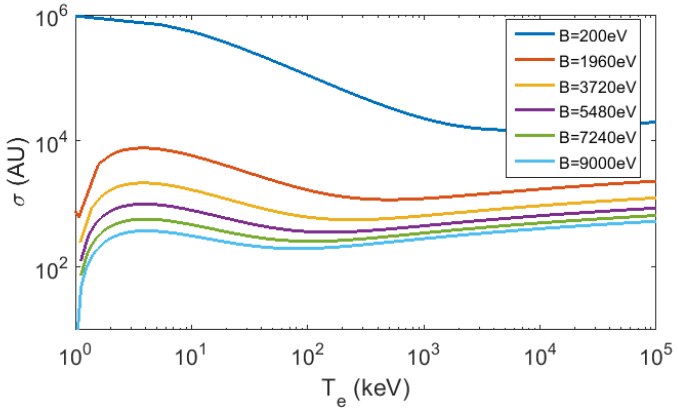

Figure 2.4: The qualitative behavior of σ_{MRBEB} as a function of electron energy for a range of K-shell binding energies.

For electrons incident upon a copper target, the absolute K-shell ionization cross section has been experimentally and theoretically determined as a function of incident electron energy [74].

2.4.3 M-Shell Depletion

Energetic electrons from laser-plasma interactions may reflux through the target, causing volumetric heating to temperatures in excess of 100 eV; such heating may collisionally ionize the M-shell, resulting in partial depletion of $M \rightarrow K$ transitions. The resultant suppression of K-shell filling from the M-shell causes a temperature-dependent shift of the K_β/K_α ratio.

For copper targets, the variation of K_β/K_α as a function of local electron temperature has been calculated ([75]) using the simulation software PrismSPECT ([76]). The ratio, which is typically normalized to the cold material value of $K_\beta/K_\alpha = 0.14$, is depicted in Figure 2.6.

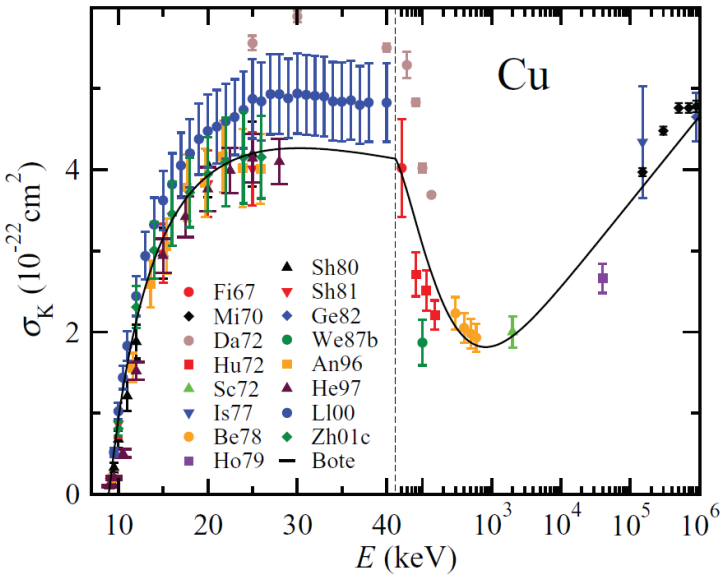

Figure 2.5: The K-shell ionization cross section section versus incident electron energy (reproduced from [74]). The solid curve is the result of distorted-wave Born approximation (DWBA) calculations, while the data points are experimentally measured.

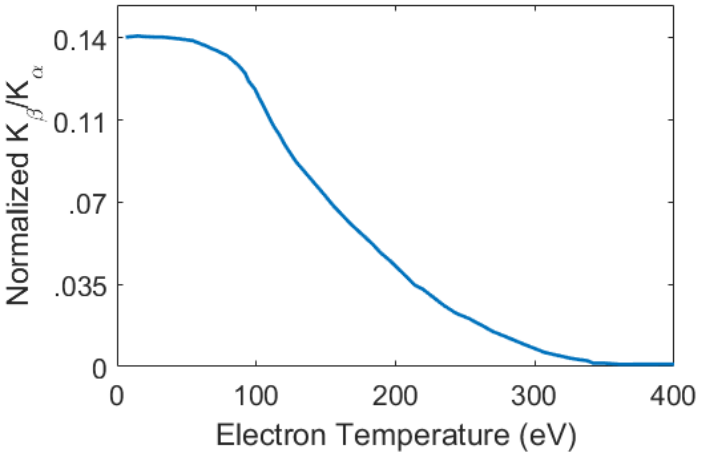

Figure 2.6: The K_β/K_α ratio as a function of bulk local electron temperature.

2.5 Theory of Magnetic Reconnection

Much plasma activity observed in astrophysics and space physics is dominated by magnetic field behavior, such as solar flares, auroral substorms, and γ-ray bursts. These activities are characterized by releases of magnetic energy, and the mechanism of this release is usually thought to be provided by magnetic reconnection (MR). MR is the topological rearrangement

of magnetic field lines and associated conversion of magnetic potential energy to plasma kinetic energy. As well as numerous examples of MR's significant role in astrophysical phenomena, it also occurs in laboratory plasmas; one such example is in the generation of sawtooth oscillations in magnetic confinement fusion plasmas.

Traditionally, MR was described as occurring solely in the MHD regime; here, the magnetic field lines are frozen to the plasma and magnetic flux is conserved. The frozen magnetic field line condition breaks down during timescales much shorter than the plasma diffusion time, and within a small diffusion region the magnetic field lines break and reconnect. In the regime of collisionless plasmas, the MHD treatment must account for two-fluid physics: electrons and ions behave differently, but the magnetic field lines remain frozen to the electron plasma; additionally, the frozen field lines condition can also be violated by electron inertia and strong pressure gradients.

2.5.1 Sweet-Parker Model

Steady-state reconnection, also known as the Sweet-Parker model, was the first formulation of MR. In 1956, Peter Sweet presented the idea that by forcing together two plasmas with oppositely oriented magnetic fields, resistive diffusion may occur at small spatial scales [30]. Attending this conference was Eugene Parker, who then further developed the model [8].

The Sweet-Parker model describes time-independent MR in the framework of resistive MHD, wherein oppositely oriented magnetic field lines reconnect within a diffusion region (see Figure 2.7), with plasma flowing into and out of this region.

In this time-independent model, two anti-parallel magnetic fields flow into the diffusion region (width 2δ and length $2L$) at speed v_{in} in a plasma with density ρ and electrical conductivity σ. Within this diffusion region, magnetic field lines reconnect and are expelled outward at v_{out}. The model assumes that the outflow speed is the Alfven speed, $v_A = B/\sqrt{\mu_0 \rho}$, which is a result of magnetic potential energy being converted to plasma kinetic energy via resistive heating and magnetic tension forces. Further, it is assumed that mass is a conserved quantity, so that $v_{in} L = v_A \delta$ (from the continuity equation); and that the

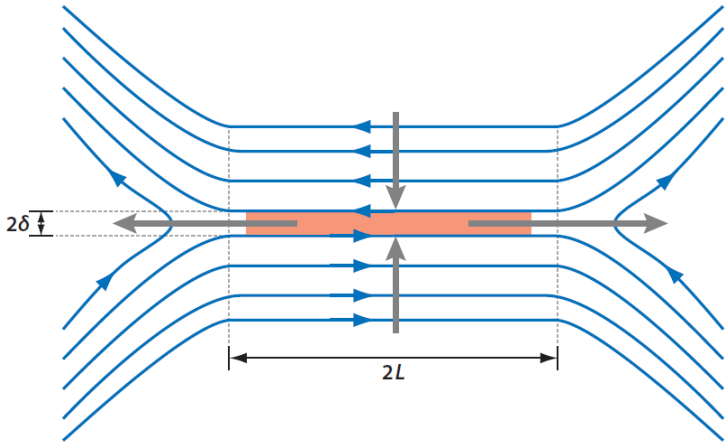

Figure 2.7: The geometry in Sweet-Parker reconnection, reproduced with permission from [26]. Anti-parallel magnetic field lines frozen to the plasma flow into the diffusion region (with width 2δ and length $2L$) from above and below, in which they reconnect; newly reconnected field lines are expelled to the left and right.

electric field $\mathbf{E}$ is given by Ohm's Law from resistive MHD:

$$\mathbf{E} = -\mathbf{v} \times \mathbf{B} + \frac{\mathbf{J}}{\sigma}. \tag{2.27}$$

This is normal to the plane in Figure 2.7 and constant. From Equation 2.27 from which we may approximate $v_{in}B/c \approx J/\sigma$, and writing $J \approx B/(\mu_0\delta)$ from Faraday's Law, we can write

$$\frac{\delta}{L} = \frac{v_{in}}{v_{out}} = S^{-1/2} \tag{2.28}$$

where S is the Lundquist number, equal to the ratio of the global Ohmic diffusion time ($\tau_D = L^2/\eta$) to the global Alfven time ($\tau_A = L/v_A$). From Equation 2.28, we see that the Poynting flux into the diffusion region, $v_{in}LB^2/mu_0$, is of the same order as the rate of Ohmic dissipation within the region, $J^2\delta L/\sigma$, as well as the kinetic energy out of the region, $\rho v_A^3 \delta/2$. The magnetic reconnection takes place on the hybrid time-scale $\tau_A^{1/2}\tau_D^{1/2}$.

The major issue with the Sweet-Parker model lies in the fact that most astrophysical phenomena observed are characterized by a very large Lundquist number, so that the reconnection rate predicted is very slow. To dissipate the incoming magnetic potential energy, the diffusion region width must be sufficiently small such that the current density is correspond-

ingly large; however, a smaller diffusion region width corresponds to a lower flux of plasma outflow, limiting the reconnection rate. The prediction of slow reconnection rates is generally not found to agree with astrophysical observations, and reconnection rates exceeding the Sweet Parker predictions are easily generated in the laboratory.

2.5.2 Petschek Model

As was stated in the previous Section, the Sweet-Parker model predicts slow reconnection rates due to the very large aspect ratio of the reconnection layer (L/δ) and correspondingly low inflow velocities. In 1964, Harry Petschek proposed a new mechanism whereby the inflow and outflow regions are disjointed by standing shock waves (Figure 2.8), with most of the inflowing plasma being deflected by the shocks and only a small percentage entering the diffusion region ([77]).

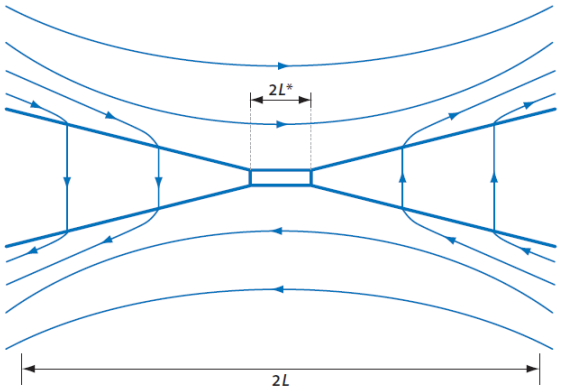

Figure 2.8: The geometry in Petschek reconnection, reproduced with permission from [26]. Slow mode shocks turn most of the inflowing plasma, with only a small percentage reaching the diffusion region.

To allow for faster reconnection rates, Petschek derived a family of mathematical solutions for this configuration in which the current sheet length L is replaced by a shorter length L', with the limiting value of $L'/L = (8\ln[S/\pi\sqrt{S}])^2$ yielding a maximum reconnection rate of $v_{inflow}/v_A = \pi/(8\ln S)$. This reconnection speed is sufficiently fast to account for most astrophysical phenomena.

Until recently it was widely thought that Petschek reconnection was only possible if the plasma resistivity or viscosity is artificially localized [78,79] to prevent the current sheet from

elongating. It is now clear that plasmoid formation, formed due to the secondary tearing instability [80], can produce the localization of current required for Petschek-like reconnection to occur (even if the plasma resistivity and viscosity are not initially localized) [81]. This mechanism is expected to be significant when plasmoids are formed along the current sheet, and produces peak reconnection rates of 0.01-0.02.

2.5.3 Collisionless Reconnection

To account for two-fluid effects (by which electron and ion behavior must be separately accounted for), Ohm's Law must be expressed in a way that allows $v_e \neq v_i$:

$$\mathbf{E} + \mathbf{v} \times \mathbf{B} - \frac{\mathbf{J} \times \mathbf{B}}{en_e} = \eta \mathbf{J}, \tag{2.29}$$

where $\mathbf{J} = (\mathbf{v}_i - \mathbf{v}_e)en_e$ (assuming singly charged ions and a quasi-neutral plasma) and assuming $\mathbf{v} \approx \mathbf{v}_i$. The Hall effect is represented by the $\mathbf{J} \times \mathbf{B}$ term. Whereas in the Sweet-Parker and Petschek models the net current is entirely normal to the plane of reconnection, in the regime wherein the Hall term dominates the electron flow corresponds to an in-plane current. The geometry for collisionless reconnection is shown in Figure 2.9.

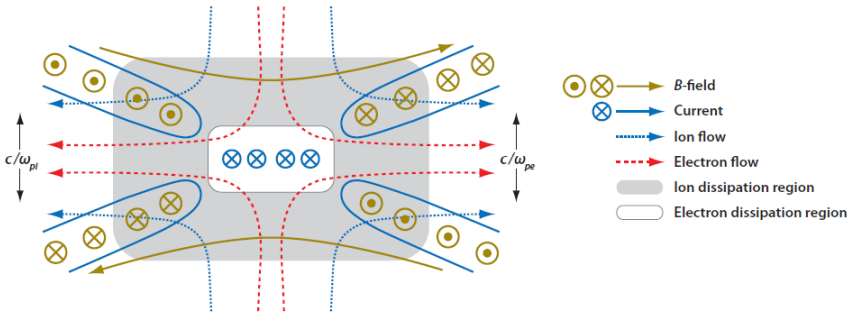

Figure 2.9: The geometry in collisionless reconnection, reproduced with permission from [26]. The ions decouple from the electron plasma at a distance $c/2\omega_{pi}$ from the neutral line, while the electrons continue inward and the magnetic field lines reconnect within a thin diffusion region.

On scales less than the ion skin depth ($\delta_i = v_A/\omega_{ci}$), $\mathbf{E}$ is supported by the Hall term or the resistive term of Equation 2.29. Hall reconnection is expected to be significant when the length of the current sheet L is comparable to the mean free path of electrons (i.e., when

one is within the collisionless regime).

While reconnection can be very fast in this model ($\approx 0.1 v_A$), not all astrophysical systems are in the collisionless regime. Examples of systems in which collisionless reconnection is expected to occur are stellar coronae and compact accretion disks.

2.5.4 Relativistic Reconnection

Magnetic reconnection enters the relativistic regime when the energy available per particle exceeds the rest mass energy. Since the energy source of reconnection is the magnetic field, the reconnection becomes relativistic if the *magnetization parameter* [82],

$$\sigma = \frac{B^2}{\mu_0 m_e n_e c^2}, \tag{2.30}$$

exceeds unity. A consequence of this is that the Alfven velocity of the plasma approaches c,

$$\frac{v_A}{c} = \sqrt{\frac{\sigma}{1+\sigma}}. \tag{2.31}$$

While many features of relativistic reconnection remain the same compared to the nonrelativistic case, there are some significant distinctive features. The astrophysical phenomena in which relativistic reconnection occur are highly magnetized, compact objects such as neutron stars and black holes, both in the magnetospheres and in the objects' relativistic outflows.

A simple model of suprathermal particle acceleration in the vicinity of the reconnection X-point can be developed [83]. In this model, the plasma converges to the reconnection region, generating a target-normal electric field via the Hall effect $\mathbf{J} \times \mathbf{B}$, and due to contributions from other terms in the generalized relativistic Ohm's law which sustain the electric field even in the X-point where $B \to 0$. Particles are thus accelerated along the region of $B = 0$, by the Lorentz force until they exit the reconnection region with a final energy dependent on how closely they approached the X-point.

Consider the region where $E > B$. Assuming a Harris sheet configuration with a guide field $\mathbf{B} = B_{0x} \tanh(z/\lambda)\, \mathbf{i} + B_n \tanh(|x/L|^s (x/|x|))\, \mathbf{k}$, where s is a structure parameter representing the magnetic field topology about the X-point. In the region where $E_y > B_z =$

$B_n \tanh(|x/L|^s(x/|x|))$, the particles are accelerated to relativistic energies, with the energy gain of the particle estimated as

$$U \approx \int ecE_y dt = \int_{x_{in}}^{x_{out}} ecE_y \frac{dx}{v_x}. \tag{2.32}$$

Here, x_{in} and x_{out} represent the positions where the particle enters and leaves the acceleration region. While it is assumed that $v_y \approx c$, the velocity v_x in the region where $E_y > B_z$ can be expressed as

$$v_x = c\frac{B_z}{E_y} \approx c\frac{B_n}{E_y}\left(\frac{x}{L}\right)^s \ll c. \tag{2.33}$$

By combining Equations 2.32 and 2.33 to express the energy gain as a function of the particle's injection point and assuming $x_{in} \ll L$ and $x_{out} \approx L$, we have

$$U \approx \begin{cases} U_0 \frac{1}{s-1}\left(\frac{L}{x_{in}}\right)^{s-1} & \text{for} \quad s > 1 \\ -U_0 \log\left(\frac{x_{in}}{L}\right) & \text{for} \quad s = 1 \end{cases} \tag{2.34}$$

where $U_0 = eE_y^2 L/B_n$. Taking $N(U)dU$, the number density of the accelerated particles, to be proportional to $|dx_{in}/dU|$, the energy spectrum may be expressed

$$N(U) \propto \begin{cases} \left(\frac{U}{U_0}\right)^{s/(s-1)} & \text{for} \quad s > 1 \\ \exp\left(-U/U_0\right) & \text{for} \quad s = 1. \end{cases} \tag{2.35}$$

Thus, for values of $s > 1$, the accelerated particle spectrum may be approximated by a power-law spectrum with a power index of $s/(s-1)$. PIC simulations of relativistic reconnection commonly yield values of $s = 1-2$ [84]. Similar spectral shapes are found in PIC simulations of driven reconnection and from measured "striped" pulsar wind emissions [85].

The condition of $E > B$ during relativistic reconnection generates very efficient particle acceleration [86]. In relativistic reconnection, the high velocity of the inflowing plasma implies a very high acceleration rate. This makes the mechanism a good candidate for explaining high-energy astrophysical phenomena, such as active galactic nuclei or gamma ray bursts which are seen to produce cosmic rays of $10^{19} - 10^{20}$ eV. The relativistic nature

of the reconnection is significant as the strong magnetic fields trap particles within the acceleration region long enough to reach high energies, while the fast inflowing velocity maintain a sufficiently high acceleration rate to prevent losses from synchrotron emission.

Synchrotron losses are the general limiting factor for astrophysical electron acceleration. It has been shown that by balancing the force of acceleration with the synchrotron radiation reaction drag, the condition of $E < B$ limits the photon energy to 100 MeV [87]. This limit is exceeded in observations of gamma ray flares [82, 88], suggesting that the acceleration occurs within a reconnection region wherein $E > B$ [89].

2.5.5 LPI Experiments: Long Pulses

Recently, magnetic reconnection has been studied in the laboratory within the context of laser-driven, high energy-density plasmas ([31–38, 90]). Two kJ/ns class lasers have been focused onto solid foils, producing expanding and colliding plasma bubbles which are each accompanied by megagauss-magnitude toroidal magnetic fields generated via the thermoelectric ($\nabla n \times \nabla T$) effect or hot electron flow [91]. This experimental regime is characterized by a high Lundquist number and large system size compared to the electron and ion inertial lengths, justifying scalings with astrophysical systems [92].

Recent 2D and 3D PIC simulations of magnetic reconnection within this regime ([39]) demonstrate that electrons may be accelerated by the reconnection fields to energies exceeding an order of magnitude larger than the thermal energy. Further, a nonthermal electron population with a power-law spectrum was observed, due to the randomly distributed electron injection into the X-points and the finite width of the current sheet.

As this class of experiments is associated with current sheet dimensions on the order of the ion inertial length (the scale at which electrons and ions decouple), the regime of reconnection is that of Hall (*i.e.*, collisionless) reconnection.

2.5.6 LPI Experiments: Short Pulses

The first experiments in this regime were conducted as described in this thesis. In the case of femtosecond or picosecond duration, multi-terawatt pulses, the interaction with an initially

solid density foil is expected to lead to different plasma characteristics and thus potentially different reconnection dynamics.

With focused intensities exceeding the relativistic threshold, an initial population of electrons is formed with a relativistic, Maxwellian velocity distribution which expands approximately isotropically. The expansion of fast electrons into vacuum rapidly sets up a strong target-normal electric field, confining a large population of fast electrons to spread radially along the target surface. A return current forms underneath this radially expanding sheet (originating from the dense plasma), resulting in an azimuthal magnetic field with O(100 MG) magnitude and expansion velocity $\approx c$.

In this regime, ion motion is negligible during the timescale of the interaction, with the reconnection being driven by the fast electrons. Thus, the situation is that of electron magnetohydrodynamics (EMHD) [93].

Recently, 3D PIC simulations have been run for fast magnetic reconnection driven by relativistic femtosecond lasers within a near critical-density plasma [94] (a regime different from that explored in this thesis). Electron pressure tensor gradients and electrostatic turbulence were found to dominate the reconnection process, as deduced from the generalized Ohm's law; this is due to the fact that laser energy was continuously injected into the plasma, generating intense electrostatic fluctuations propagating in the direction of the pulses. A strong longitudinal electric field is formed in the reconnection region, which accelerates electrons with large energy gains.

Chapter 3

Methods

3.1 Experimental Facilities

The experiments herein discussed were performed in three separate experimental facilities. The first was the ultra-intense HERCULES laser at the University of Michigan's Center for Ultrafast Optical Science (CUOS), the second was the Omega EP Laser System at The Department of Energy's Laboratory for Laser Energetics, and the third was the Titan Laser at Lawrence Livermore National Laboratory (LLNL)'s Jupiter Laser Facility (JLF). Many similar diagnostics were used at these facilities, in which case a more general treatment will be given. In addition to experimental diagnostics, computational modeling was important in interpreting the experimental results.

3.1.1 HERCULES Laser System

The HERCULES laser is a chirped pulse amplified (CPA) Ti:Sapphire laser system capable of delivering 9 J, 30 fs pulses (yielding a power of 300 TW) at a central wavelength of 810 nm. It achieved a record focused intensity of 10^{22}W/cm^2 in 2008 [43]. A block diagram for the HERCULES laser is given in Figure 3.1.

The laser consists of multiple stages of amplification. A Kerr-lens, mode-locked oscillator produces seed pulses with bandwidth-limited duration of 12 fs, at a rate of 75 MHz and with 4 nJ energy per pulse. The pulses pass through a Pockels cell, which uses a series of

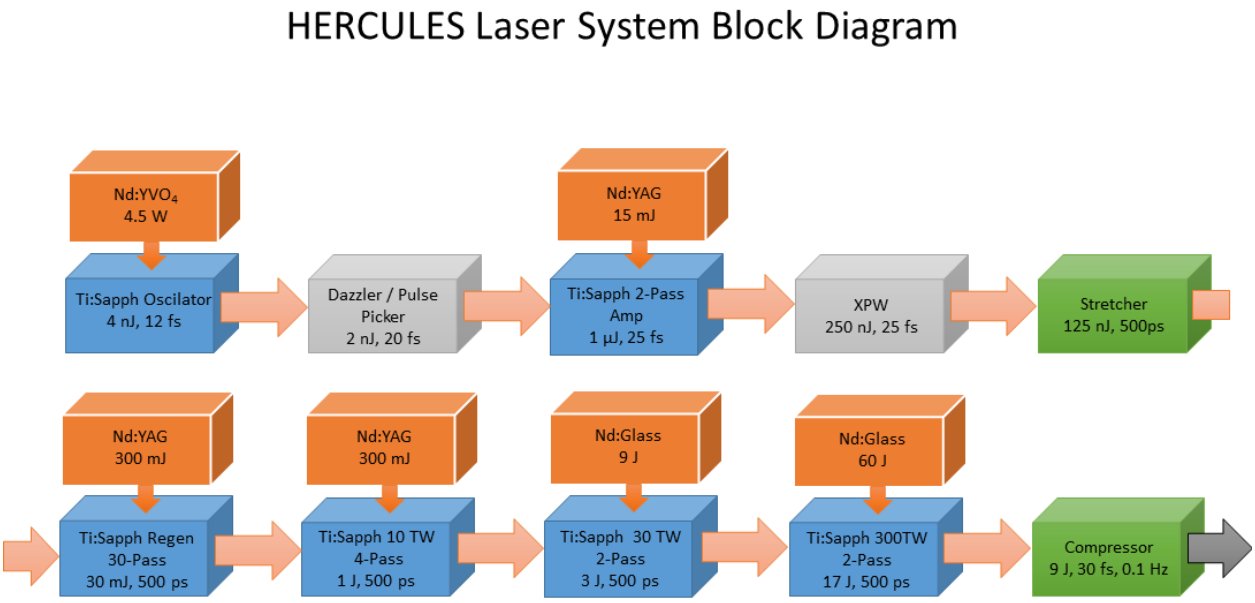

Figure 3.1: A block diagram of the HERCULES laser, indicating the amplification stages (blue), corresponding pump lasers (orange), the stretcher and compressor (green), as well as the Dazzler / Pulse Picker and XPW stage (gray). The final pulse is delivered to one of two experimental chambers.

polarization rotators to opto-electronically switch out pulses, reducing the pulse rate to 10 Hz. The selected pulses are then amplified to 1 μJ to prepare for entering the Cross-Polarized Wave Generation (XPW) stage [95]. The XPW stage relies on the intensity dependence of pulse polarization rotation via four-wave mixing. This enables the reduction of Amplified Spontaneous Emission (ASE) since the pulse must reach a sufficiently high intensity in order for its polarization to rotate, allowing the high-intensity portion of the pulse to pass through a polarizer while attenuating the low intensity, ASE pre-pulse. Since the intensity of the generated XPW has a cubic dependence upon the input beam, the effect is extremely successful in improving the contrast of a femtosecond pulse's temporal and spatial profiles. A two-crystal XPW scheme was used on HERCULES to optimize the conversion efficiency.

The contrast-enhanced pulse is now stretched (chirped) to a duration of 500 ps to allow

further amplification while remaining beneath the damage threshold of the amplification media. It then makes 25 passes through the Regenerative Amplifier (Regen), during which it is amplified by a factor of 10^6. A large contribution to the ASE prepulse is made during the Regen amplification, but is ameliorated by the reduction in required Regen gain due to the pre-amplification in the XPW scheme (with a loss in energy). After Regen amplification, the nanosecond pulse contrast (defined as the ratio of the pulse energy nanoseconds before the peak to the peak energy) was measured to be reduced from 10^{-8} to 10^{-11} by XPW [96].

The pulse then enters a series of multi-pass Ti:Sapphire amplifiers, which amplified the pulses to peak energies of 1 J, 3 J, and 17 J, respectively. Back reflections in these amplifiers can be destructive, so Pockels cells, spatial filters, and Faraday isolators were used to protect each stage. The pulse (now chirped and amplified) then entered a Treacy compressor, which recompressed the pulse to a FWHM duration of 40 fs. While the post-compressor bandwidth equaled 25 nm (implying a bandwidth-limited pulse duration of 37 fs), higher order dispersion experienced in the system increased the optimal pulse duration to 40 fs. These pulses were then delivered to the experimental chambers at an available shot rate of 0.1 Hz, as a 10 cm diameter circular beam polarized horizontally and p-polarized in the laboratory frame.

3.1.2 Omega EP Laser System

The Omega EP Laser System consists of four beamlines, two of which have the capability to operate with pulse durations of 1-100 ps at an operational central wavelength of 1054 nm. In addition to this short-pulse capability, all four beams can operate in long-pulse mode with durations of 1-10 ns. The long pulse, on-target energies can reach 2.5 kJ for 1-ns pulses and 6.5 kJ for 10 ns pulses [97].

Beam Lines (BL) 1 and 2 can produce pulses with durations 1-100 ps, and may also be used in long-pulse mode; BL 3 and 4 may only operate in long pulse mode. A block diagram of the laser sources subsystem for BL 1 and 2 is found in Figure 3.2. Different architectures are required to generate short-pulse versus long-pulse beams on Omega EP. The short-pulse source is based on Optical Parametric Chirped-Pulse Amplification (OPCPA) in order to achieve the required bandwidth.

The short pulse beams begin with a commercial mode-locked oscillator (Time Bandwidth

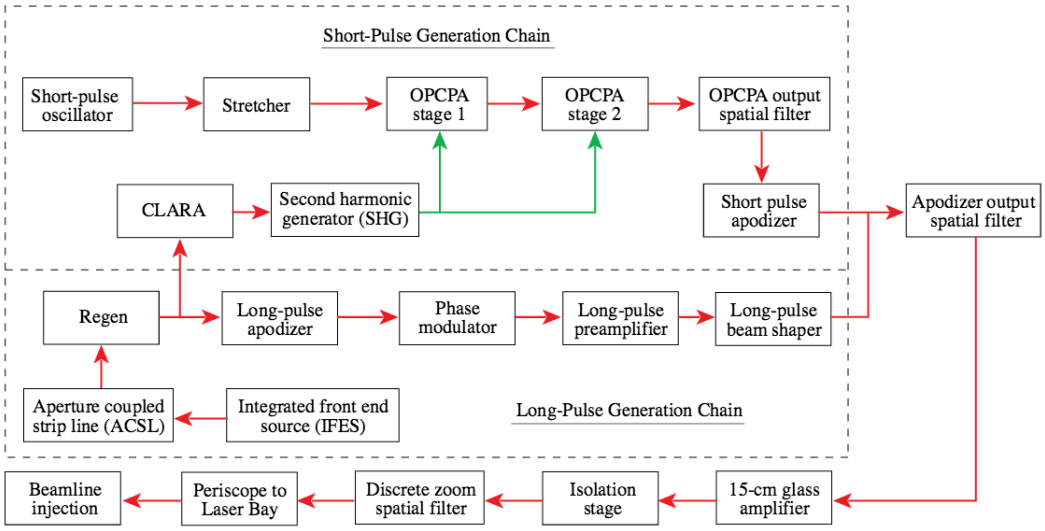

Figure 3.2: (Reproduced with permission from the Omega EP System Operations Manual [97]). A block diagram of the Omega EP Laser Sources subsystem for BL 1 and 2. These sources support both short pulse (1 to 100 ps) and long-pulse (1 to 10ns) beam generation. The green arrows represent the path for a frequency doubled beam.

Products Inc.), which produces pulses with ≈200 fs duration. These are then stretched to ≈2.4 ns FWHM in an optical system utilizing diffraction gratings to chirp the pulse. The resulting beam is spatially shaped and then amplified by an optical parametric amplifier. This OPCPA stage is key to short-pulse performance, providing broad gain bandwidth, high gain over a small optical volume, and reduced ASE. The bandwidth of the pulse is preserved, and a gain of 10^9 is achieved. The signal exiting from the OPCPA stage is amplified further with a 15 cm Nd:glass amplifier and then injected to another stage for further amplification. Following final amplification, the beam is directed to a system of four compressor gratings which use deformable mirrors to correct aberrations in the compressor optics as well as aberrations from short-pulse transport.

Following recompression with tiled-grating assemblies, the beams are wavefront corrected by a deformable mirror, and reflected from a partially transmissible mirror, the transmission through which enters a diagnostic area and the reflection from which is directed toward the experimental area. For the experiments herein described, the two short-pulse beams were utilized with 20 ps pulse durations and either 500 J or 1 kJ of energy.

3.1.3 Titan Laser System

Titan is one of five laser systems at JLF. Commissioned in 2007, it offers a synchronized short-pulse PW-class beam and long-pulse kJ beam for laser-plasma interaction (LPI) experiments. Its short-pulse capabilities include a 1053 nm beam with 0.7-200 ps pulse width and up to 300 J of energy at a central wavelength of $\lambda = 1053$ nm, and its long-pulse capabilities include the generation of a $\lambda = 1053$ nm beam with 0.35-20 ns pulse width with up to 1 kJ of energy. It is also possible to frequency-double the pulse to a wavelength of 527 nm. With a focused diameter of ≈ 10 μm, intensities of 10^{21}W/cm^2 and a nanosecond energy prepulse contrast of 10^{-5} are possible [98].

Titan's front end includes a custom pump laser and two stages of OPCPA; the beam is stretched in an Offner stretcher to 1.6 ns, amplified through the Janus amplifier chain (which has a B-integral limit of 750 J at this pulse duration), and is recompressed using a pair of 40×80 cm multilayer dielectric diffraction gratings. The compressor utilizes an angled two-pass system which yields small vertical spatial chirp and allows for a large beam size (up to 25 cm).

The single short-pulse beam was split before final amplification using a striated mask to avoid imparting diffraction patterns, and then independently co-timed by guiding the beam halves to individual translation stages. For the experiments described in this thesis, a pulse duration of either 1 ps or 10 ps was used, with a total of either 120-160 J or ≈240 J delivered on-target, respectively.

3.2 Laser Diagnostics

3.2.1 Diffraction Limited Focusing

A beam that is focused to its theoretical minimum focal spot size is known as diffraction limited. This theoretical limit is given by $r = 1.220 f\lambda/D$, where r is the radius of the smallest spot to which a collimated beam with wavelength λ and diameter D can be focused by an optical element with focal length f. To avoid B-integral accumulation (an intensity-dependent measure of the light's self phase modulation) through focusing optics which may

undesirably increase the pulse duration, the use of reflective focusing optics is nearly universal in short-pulse experiments.

On the HERCULES laser, the beam was focused with a protected gold coated Off-Axis Paraboloid (OAP) mirror with an f-number of $f_{\#} \equiv f/D = 3$. Dielectrically coated glass paraboloids with f-numbers of 2 were used both on Omega EP and Titan, with protective glass blast shields to prevent damage from plasma debris. The use of metallic OAPs on HERCULES was beneficial due to their relative low cost despite their superb performance when aided by wavefront correction techniques.

Realistically, imperfections in the focusing optics or slight aberrations in the beam itself limit the minimum achievable focal spot size, although steps may be taken to further approach the limit. One such step is the use of corrective optics, such as a deformable mirror (DM) which is used to compensate for aberrations in the beam that introduce focusing limitations. The DM used in the HERCULES solid target experimental chamber, manufactured by Xinetics, was comprised of a thin dielectric mirror with 177 piezoelectric actuators which precisely deformed the mirror surface; this allowed local path-length variations in the pulse wavefront to be introduced, compensating for aberrations in the incoming beam. To determine the optimal deformation, a Shack-Hartmann HASO wavefront sensor (manufactured by Imagine Optics) was used, which measured the aberrations in the wavefront after being focused by the OAP. The correction algorithm recorded the wavefront response to ± 5 V perturbations on each actuator, decomposed the wavefronts as Zernike polynomials, and calculated a voltage profile for the ultimate correction. The software routine monitored the response of the wavefront as it iterated through several approximations of this profile, until it converged to an optimal form. This process allowed dramatic improvements to the wavefront and corresponding focal spot, typically increasing the focused intensity by an order of magnitude. Figure 3.3 (c)-(d) demonstrates the wavefront and calculated focal spot before and after this correction process.

The focal spot produced by the f/3 OAP was also directly measured by inserting a $30\times$ microscope objective into the focus, producing an image onto a filtered CCD camera. This is depicted in Figure 3.3(a)-(b) before and after wavefront correction, demonstrating a near diffraction limited focal spot of 3.8 μm.

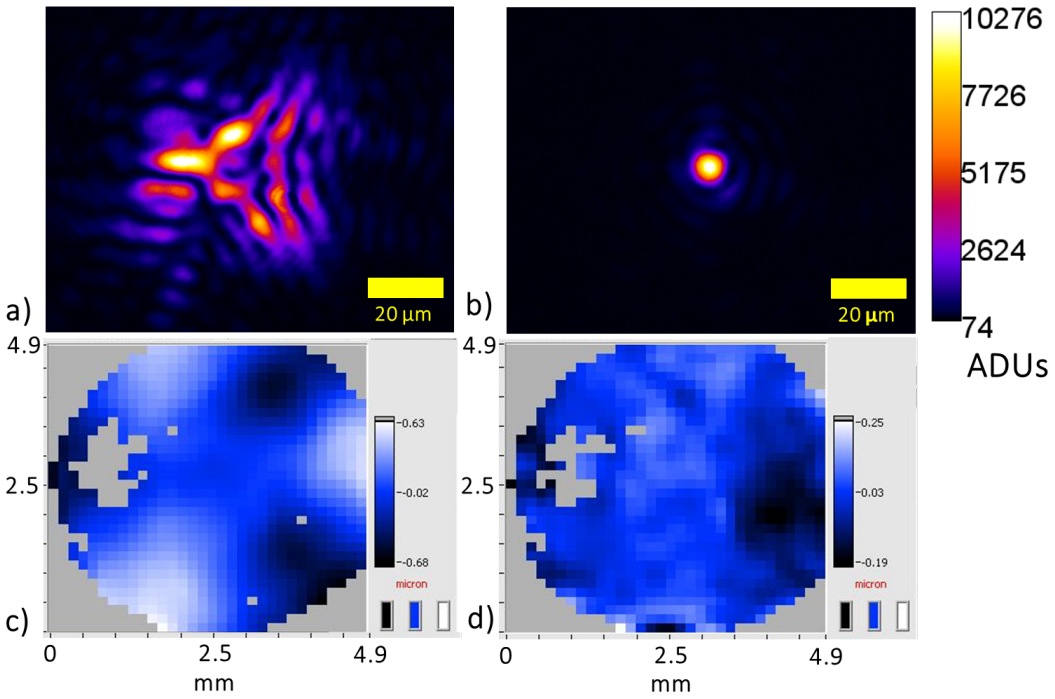

Figure 3.3: The HERCULES f3 focal spot imaged with a 30× magnification imaging system, before (a) and after (b) wavefront correction. Figures (c) and (d) depict the wavefront of the beam before and after correction, respectively, as measured by the HASO.

For the split-beam configuration on HERCULES, the internal stresses within the metallic OAP caused the cleaving procedure to introduce unrecoverable warping to the parabolic surface; due to this, near diffraction limited focal spots were impossible. However, by aligning the two OAP halves with the previous wavefront correction applied, an optimal focal spot FWHM of was obtained. These focal spots are shown in Figure 3.4, and show that Spot 1 included 37.5% of the total beam energy and focused to an area of 174 μm^2, while Spot 2 included 62.5% of the total beam energy and focused to an area of 337 μm^2, yielding a comparable intensity for both beam halves of $\approx 2 \times 10^{19}$ Wcm^{-2}.

The OMEGA EP laser system utilized DMs for each of the two short-pulse beams used in the experiments conducted for this thesis. After DM correction, a diagnostic pick-off is taken of the beam's near field, which is then sent to a high-resolution Shack-Hartmann wavefront sensor and the far-field irradiance is calculated based on scalar diffraction theory. An R80 value (the radius at which 80% of the focused energy is contained) of ≈13 μm were typical for the two beams; Figure 3.5 demonstrates a typical focal spot.

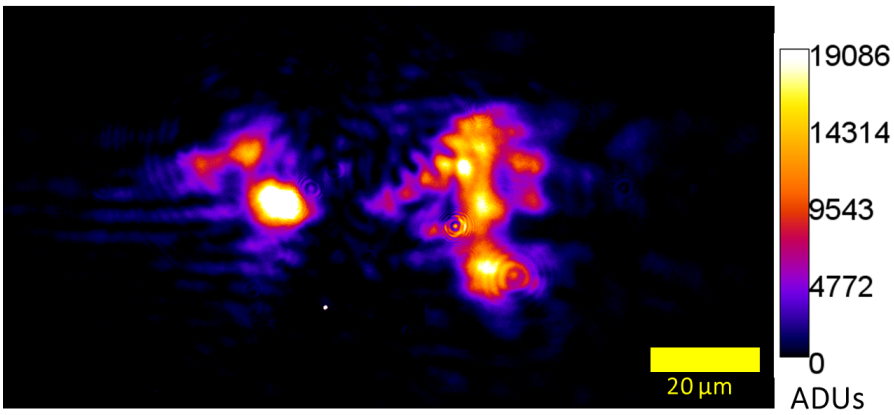

Figure 3.4: The HERCULES f3 focal spots with a cleaved OAP. Spot 1 (S_1) has 60% of the energy in Spot 2 (S_2); spot 1 has an approximate FWHM area of 174 μm^2, while Spot 2 has an approximate FWHM area of 337 μm^2. Both spots therefore had approximately equal peak focused intensities of $\approx 2 \times 10^{19}$ Wcm^{-2}
given the slightly imbalanced beam energies.

DMs were also utilized on the Titan laser, allowing a nominal focal spot of $\approx 8\mu$m FWHM. A fine mesh was placed at focus and imaged to determine the approximate focal spot size, which tended to be slightly above this nominal value.

The main advantage of the HERCULES configuration is that since the focal spot is corrected based on the wavefront after the final focusing optic, corrections may be made to aberrations introduced by the focusing optic itself. On both the Omega EP and Titan laser systems, the DMs correct the wavefront as measured earlier in the system.

3.2.2 Pulse Duration Measurements

Measuring the duration of a short laser pulse is not a trivial matter, and typically one must rely on optical autocorrelation techniques. Figure 3.6 demonstrates a 2nd order autocorrelator scheme such as was used at the HERCULES laboratory to determine the femtosecond-scale pulse duration; here, the incoming beam is split with a beamsplitter, sending one half down a fixed distance and the other over a variable distance (to ensure final temporal overlap of the beams). The two beam halves are sent to a reflective optic and are recombined into a 2nd order harmonic generating crystal (such as BBO) such that a slight angle existed

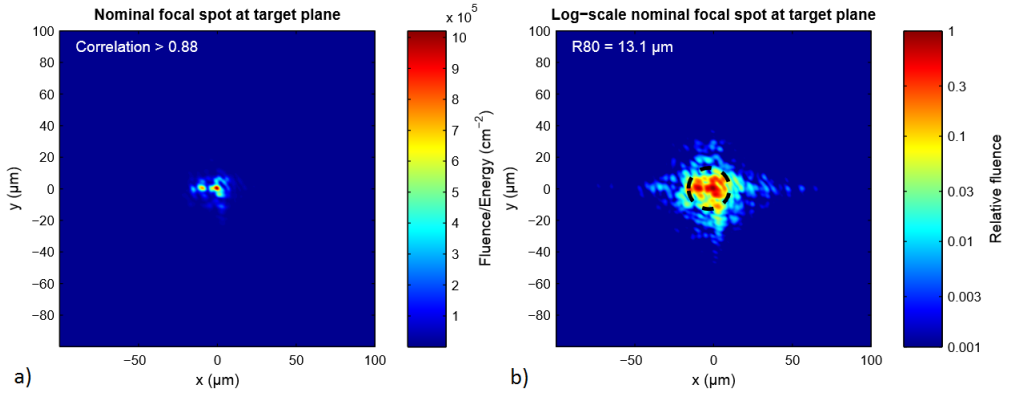

Figure 3.5: Calculated focal spot from Omega EP's short-pulse beam (BL 1) after correction, shown on a linear (a) and logarithmic (b) scale.

between the two incident beams.

The second harmonic light produced was imaged onto a CCD, enabling the calculation of the pulse duration based on the width of the trace. The compressor grating separation was then varied to find the minimal pulse duration, which was measured to be 39 fs with XPW under vacuum (as shown in Figure 3.6).

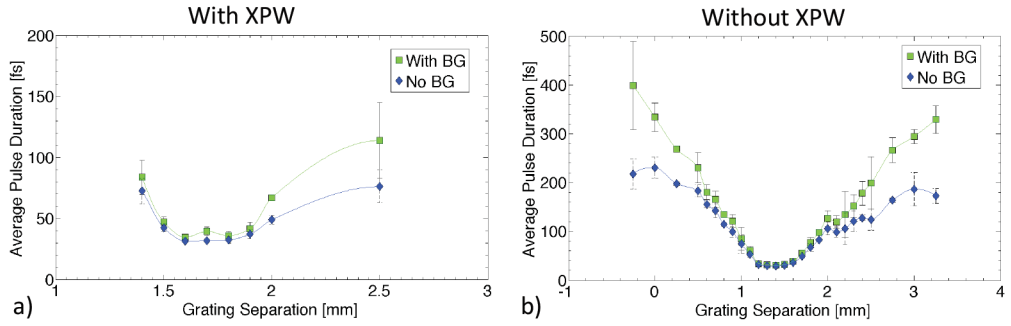

Figure 3.6: Second order autocorrelations of the HERCULES laser pulse in vacuum with (a) and without (b) XPW installed. The traces are shown with and without the background (BG) removed. An optimal pulse duration with XPW is measured to be 39 fs with XPW and approximately 30 fs without XPW.

The Omega EP laser utilizes an ultrafast streak camera based on the Rochester Optical Streak Camera (ROSS) platform [99] to measure pulse widths in the 8-300 ps range, yielding a resolution of a few picoseconds. The Titan laser system utilizes 2nd and 3rd order autocorrelation to optimize the temporal duration of their 1ps pulse, and either autocorrelation or streak camera techniques for longer pulses. Streak cameras will be covered in Section 3.3.

3.2.3 Pulse Contrast

Fine control of the plasma conditions encountered by the main pulse are paramount for conducting LPI experiments; this can be accomplished by control of the laser pre-pulse. Pre-pulse is defined as the light preceding the main pulse in time; the ratio of the energy or intensity of this preceding light to that of the main pulse is defined as the energy or intensity contrast, respectively. A laser pulse will typically have a pre-pulse nanoseconds in duration preceding the main pulse, primarily originating from ASE within the laser cavity, and additional pre-pulse picoseconds before the main pulse originating from leakage through Pockels cells which select individual pulses from a chain of input beams with relatively high repetition rate. Control over a laser's prepulse is crucial to performing LPI experiments, both for pulse profile consistency and for allowing one to access regimes which require sufficiently suppressed pre-plasma.

On the HERCULES laser, XPW was used to improve the nanosecond pre-pulse contrast (defined as the ratio of the pulse energy nanoseconds before the peak to the peak energy). The effect of using XPW was a measured reduction in nanosecond pre-pulse intensity contrast from 10^{-8} to 10^{-11} by XPW [96], as determined with third order autocorrelation. Figure 3.7 demonstrates the temporal profile featuring this improvement. Although not utilized for the experiments described herein, a double plasma mirror (DPM) setup was available which offers a contrast improvement of an additional 3 orders of magnitude [100].

On the Omega EP laser, the nanosecond pre-pulse contrast is measured on a shot-to-shot basis using a calibrated fast photodetector, shown in Figure 3.8 (a); a temporal resolution of 200ps, dynamic range of 10^9, and temporal range $> 1\mu$s are typical. A nanosecond pre-pulse energy contrast of 10^{-6} is typical; an example of a such a measurement from a 20ps, 1kJ beamline is displayed in Figure 3.8 (b).

On the Titan laser, a water cell diagnostic is utilized to measure the nanosecond pre-pulse contrast on a shot-to-shot basis. These operate by allowing a pre-pulse to travel through the water cell and reach a photodiode detector, while the more intense component of the beam ionizes the water at a known intensity and reflects the remaining light, thus protecting the diode.

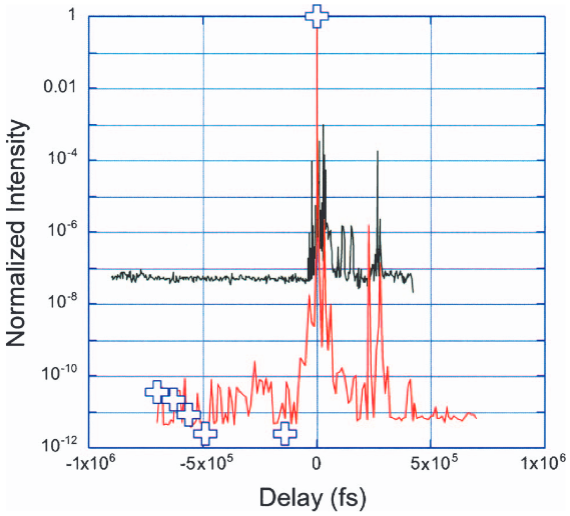

Figure 3.7: (Reproduced from V. Chvykov, *et al.* [96]. Third-order autocorrelation with without XPW (black curve) measured with the regenerative amplifier only, and measured with XPW at 10 TW (red) and 50 TW (crosses).

For magnetic reconnection experiments, the requirements upon the laser contrast are somewhat relaxed compared to, for example, thin-film ion acceleration experiments. This is because the target materials in the former case are generally relatively thick (tens of microns), and a moderate pre-plasma scale lengths can actually be advantageous if high laser energy coupling efficiency is a priority.

3.3 Radiation Diagnostics

3.3.1 Spherical K_α Crystal

A spherically bent Quartz crystal was utilized as a primary diagnostic on each experimental platform. They each had a $2d$=3.08 Å lattice spacing, designed specifically to reflect only light at the copper K_α wavelength of 0.154 nm. A high aberration limited spatial resolution (10 μm on Omega EP and 15 μm on HERCULES and Titan) allows detailed images to be formed of the copper K_α radiation emitted during an LPI experiment. The crystal forms part of a Rowland circle (the diameter of which equals the radius of curvature of the crystal); if the source of emission is placed at a point other than at the center of this circle, then a simple imaging system is formed allowing for the creation of a magnified image; this geometry is

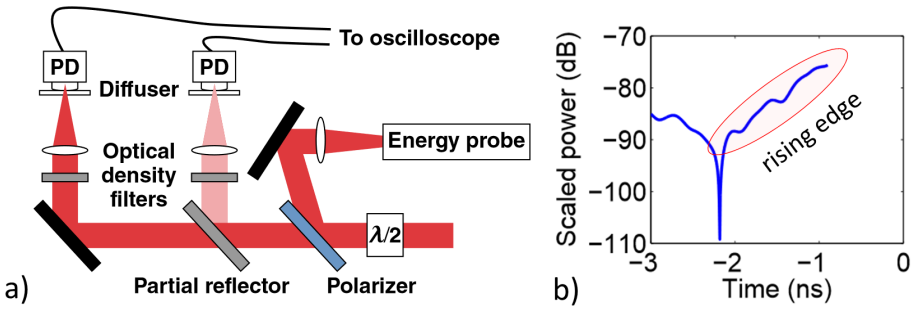

Figure 3.8: (a) The on-shot Omega EP nanosecond pre-pulse contrast measurement diagnostic is comprised of 2 fast photodetectors [101]. An example of a power contrast measurement from Omega EP is given in (b), scaled to the peak power.

shown in Figure 3.9.

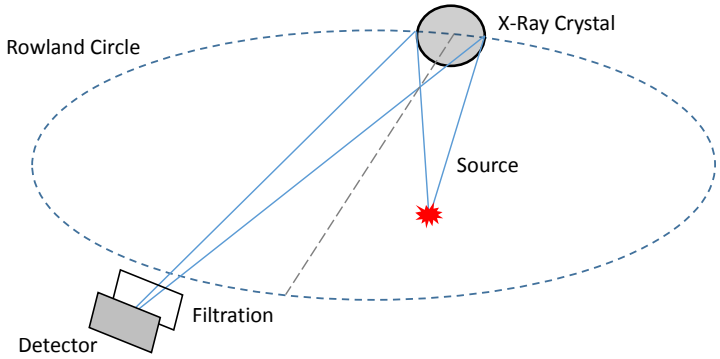

Figure 3.9: The Rowland circle geometry with a spherical crystal imager placed at the perimeter of the circle, the source of emission placed at a distance $> R$ where R is the crystal's radius of curvature, and a magnified image formed at a point exterior to the circle. A similar geometry is used for the experiments described here.

K_α crystals are used as a diagnostic of the hot electron dynamics, measuring the emissions caused by their propagation through a target. In the experiments described here, the K_α emission intensity is assumed to be directly correlated to the location of hot electron currents, increasing in intensity if the electrons are directed into the target or if the number of hot electrons is increased.

The efficiency of a spherically bent X-ray crystal with near-normal incidence is given by

$$\eta = \frac{R_{\mathbf{int}}}{(\Delta\lambda/\lambda)\tan\theta} \tag{3.1}$$

where $R_{\mathbf{int}}$ is the crystal's integrated reflectivity, $\Delta\lambda/\lambda$ is the relative spectral linewidth of the X-rays, and θ is the Bragg angle. K_α crystals are characterized by a narrow spectral width such that $\lambda/\delta\lambda >> 1$ [102].

3.3.2 X-Ray Streak Cameras

A streak camera is a device which detects the variation in a source of light's intensity over time, designed for either optical light or X-rays. A generalized streak camera operates as follows (illustrated in Figure 3.10: incident light with some time variation enters a slit and strikes a photocathode, where they produce electrons via the photoelectric effect. The electrons are accelerated in a photocathode ray tube and a transverse electric field deflects them; a fast modulation in this electric field introduces a time dependent sideways deflection of the electrons. This deflection is recorded as the electrons strike a phosphor screen and a CCD records the resultant spatial streak. One may then calculate the temporal profile of the initial incident light by correlating the position on the CCD with time.

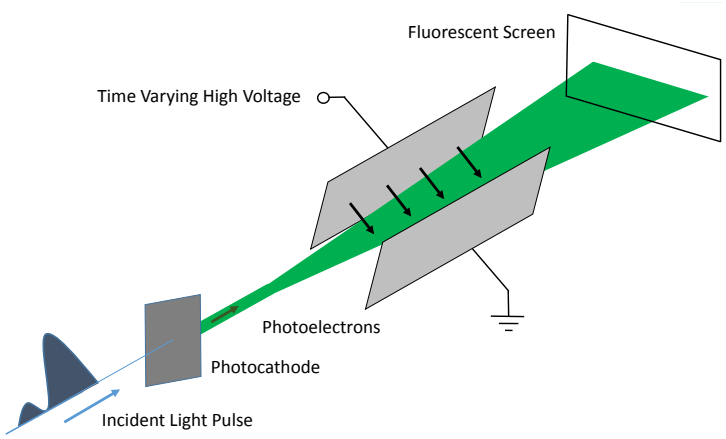

Figure 3.10: A conventional streak camera. A pulse of light is incident upon a photocathode, upon which photoelectrons are produced which pass through a time varying electric field. This field induces a spatial deflection of the electrons in a manner which depends upon the time of emission. By detecting the spatial distribution of these electrons with a fluorescent screen, the temporal profile of the initial light pulse may be reconstructed.

The sources of temporal dispersion in an X-ray streak camera are combined to give the total temporal resolution,

$$\Delta t = \left[(\Delta t_{phys})^2 + (\Delta t_{tech})^2\right]^{1/2} \tag{3.2}$$

where $\Delta t_{phys} = \Delta x_{slit} v$ (v equaling the sweep speed) and $(\Delta t_{phys})^2 = \Delta t_C^2 + \Delta t_K^2 + \Delta t_L^2$, where Δt_C is the transit time dispersion due to Coulomb dispersion, Δt_K^2 is the transit time in the cathode/mesh region, and Δt_L is the transit time in the region of electron focusing optics. Δt_K is the most dominant term and is given by

$$\Delta t_K \approx \frac{3 \times 10^{-8}[(E_0 + \Delta kT/2)^{1/2} - (E_0 - \Delta kT/2)^{1/2}]}{E_{field}} \tag{3.3}$$

Here, E_0 is the energy of electrons in eV, ΔkT is the FWHM energy spread of the electrons in eV, and E_{field} is the strength of the accelerating field in V/cm.

To ensure co-timing between the two Titan short-pulse beams, a 2 mm diameter scattering sphere was placed at target chamber center (TCC) and a collection lens was positioned as to image any light scattered from the sphere onto the slit of an optical streak camera. The resultant streaked images of the scattered light allowed both the optimization of the pulse durations and the overlap of the two pulses in time.

An Ultrafast X-Ray Streak Camera (UFXRSC) was utilized at the Omega EP facility. It was used both to monitor the relative arrival time of the two short-pulse beams, and to measure the duration of the copper K_α emission from the target mid-plane. The UFXRSC has a high temporal resolution of 10 ps and detects incident X-rays. A photocathode comprised of potassium bromide (KBr) sputtered onto beryllium was used for general measurements such as beam co-timing, while a cesium iodide (CsI) photocathode was used for streaking incident copper K_α X-rays due to its higher quantum efficiency at this wavelength.

Whereas most X-ray streak cameras have accelerating electric field strengths of $E_{field} \approx$ 10 kV/cm, the UFXRSC uses a pulse charged photocathode, allowing electric field strengths of $E_{field} = 250$ kV/cm; from Equation 3.3 this allows a time resolution of nearly 500 fs [103].

3.3.3 X-Ray Pinhole Cameras

An X-ray pinhole camera operates by the mechanism of camera obscura, whereby a small aperture is placed in proximity to the object and an image is formed opposite to the aperture. The basic geometry is illustrated in Figure 3.11. The X-ray pinhole camera (XRPHC) is a common diagnostic in LPI experiments due to their ease of use. They may provide useful data such as the total X-ray brightness and the spatial extent of the source.

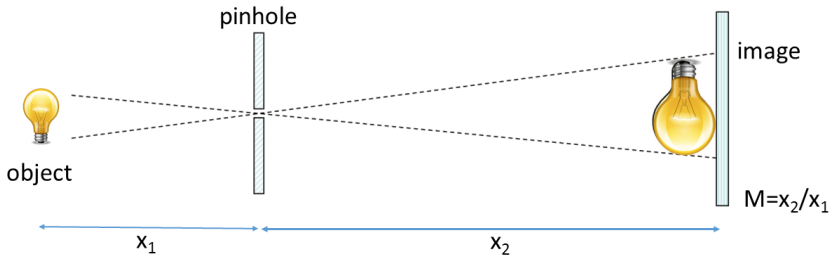

Figure 3.11: A simple diagram demonstrating a pinhole camera. An aperture is placed a distance x_1 from the object, and an inverted image is formed a distance x_2 from the aperture. A magnification of $M = x_2/x_1$.

The aperture size of an XRPHC is optimized for a particular photon energy distribution and object/image distances; for these parameters there is one aperture size that minimizes the width of the image point spread function (PSF) (thereby maximizing the resolution). If the aperture is too large, ray-optic 'spread' dominates, whereas if the aperture is too small, diffraction effects dominate. For broadband X-ray emission from LPI experiments, an aperture size of 5-50 μm is typical, with a FWHM resolution ranging over the same distances; Figure 3.12 demonstrates the FWHM PSFs corresponding to varying aperture sizes and photon energy distributions.

In practice, an array of closely spaced pinholes may be used, so that an array of images is formed; by variably filtering these images, an approximate emission spectrum may be reconstructed. Additionally, a Mylar filter and magnet pair are often used at the entrance of the camera to block charged particles while allowing relatively uninhibited transmission of X-rays.

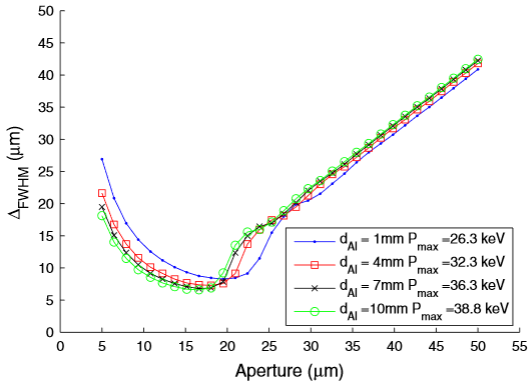

Figure 3.12: (Reproduced from [104].) The FWHM of the PSF of a pinhole as a function of slit aperture size for varying peak X-ray energies (selected by varying the aluminum filter size d_{Al}).

3.3.4 X-Ray Framing Camera Detector

An X-ray framing camera combines concepts from X-ray pinhole cameras and X-ray streak cameras. An array of pinholes is utilized, through which X-rays form images onto a photocathode. A high voltage pulser is used to accelerate the resulting photoelectrons, after which time the photoelectrons separate in space as a function of their energy while propagating through a drift-space. The photoelectrons then proceed onto a time-gated micro-channel plate, which produces an array of images of the same original emission but with an effective temporal displacement between the frames.

DIXI, a variation on the X-ray framing camera detector which has an additional high voltage sweep, was utilized on Titan. This resulted in 38 frames with 50 ps intervals. The device was sensitive to X-rays of energies between 2 - 17 keV [105].

3.3.5 Single Photon Counter

Single photon counting is a technique in which individual photons are counted using a single-photon detector. The detector may be configured to yield an electronic signal proportional to an incident photon's energy, thus allowing the reconstruction of a radiation source's emission spectrum. The efficiency of such a device is limited by its quantum efficiency and sources of electronic loss in the system. To be within the single photon regime, a rule of thumb is that the probability of a double-hit (more than one photon striking a single pixel) described by

Poisson statistics is less than 15% [106].

If a CCD is used as the single-photon detector, the pixel values may be binned and the spectrum reconstructed via

$$\frac{dN_x}{d(\hbar\omega)} = \frac{a}{k_1(\hbar\omega)QE(\hbar\omega)T(\hbar\omega)}\frac{dN_c}{d(\hbar\omega)} \times \frac{dN_{SPE}}{dN_c} \tag{3.4}$$

where $k_1(\hbar\omega)$ is the probability that a single photon results in a single pixel event, dN_{SPE}/dN_c is the number of single-pixel events for each number of counts obtained from a reconstruction algorithm, $dN_c/d(\hbar\omega) = \alpha = 0.11$ counts per eV^{-1}, $QE(\hbar\omega)$ is the CCD quantum efficiency, $T(\hbar\omega)$ is the efficiency of the CCD filtration, and a is a normalization factor to ensure the reconstructed spectrum yields the number of counts as recorded by the CCD.

On OMEGA EP, a single photon counter was utilized in the configuration depicted in Figure 3.13. The SPC diagnostic used a Spectral Instrument series 800 CCD camera mounted 14 m from TCC in single photon counting mode to measure the K-shell emission from 5-25 keV. The CCD was shielded by 20 cm of Pb, and Cu filters were utilized to optimize the signal.

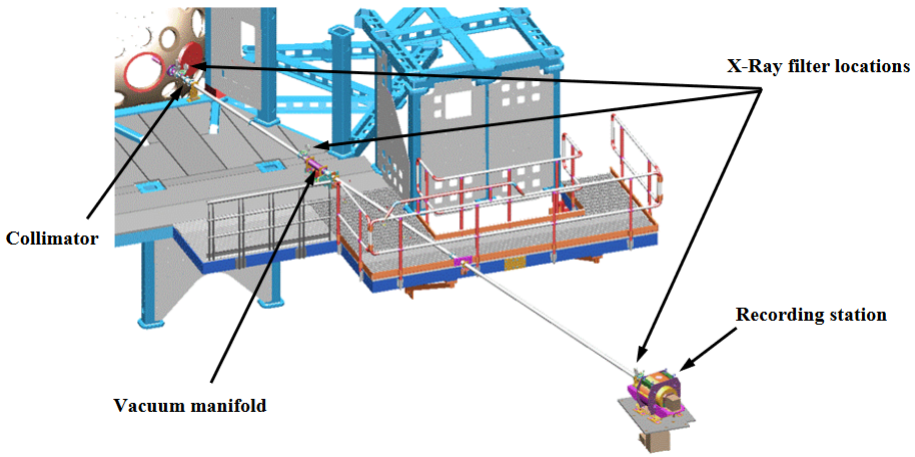

Figure 3.13: The configuration of the SPC used on OMEGA EP (reproduced from [107]).

3.3.6 Charged Particle Spectrometers

Charged particles generated during a LPI experiment (ranging in energy up to 100s of MeV) can be captured and their energy determined. The temperature (assuming the typical approximation of a Maxwell-Boltzmann distribution of energies) of a plasma component such as electrons or one of a number of potential ion species can be indicative of the LPI phenomena that led to their generation.

Many charged ion detector designs rely on static magnetic and electric fields to disperse the particles as a function of their charge-to-mass ratio. Commonly this is achieved using a permanent magnet and a high voltage parallel-plate capacitor, as in the Thomson Parabola [108]. Electron spectra may be easily measured using only parallel plate magnets, which deflect the electrons as a function of their energy. Another method is the utilization of a fluorescent material such as LANEX which produces a well characterized luminous response to electron bombardment [109]; this may be used in conjunction with variable filtering to deduce the spectrum.

To measure the spectra of relativistic electrons in the OMEGA EP and Titan experiments, the Electron-Proton-Positron Spectrometer (EPPS) was utilized (designed by LLNL [110]). Depicted in Figure 6.7 (a), this is a compact unit comprised of a lead/tantalum outer shield which encloses a permanent magnet pair. Image plates (sheets of photostimulable phosphor material [111]) are inserted into the detection plane, where charged particles passing through the entrance slit are deflected as a function of their energy. The spectrometer has a side to which positive particles are deflected (primarily protons and positrons) and another to which electrons are deflected. Figure 6.7 (b) illustrates its dispersion characteristics.

To determine the angular dependence of an electron beam or plume emission, the Osaka University Electron Spectrometer (OU-ESM) was also utilized for the OMEGA EP experiments. This was a five-channel electron spectrometer utilizing magnet pairs for energy-dependent deflection, with view angles covering 25° in 5° increments. The deflected electrons were recorded with BAS-MS image plates detectors. A schematic for this device is demonstrated in Figure 3.15, and the electron dispersion is presented in Figure 3.16.

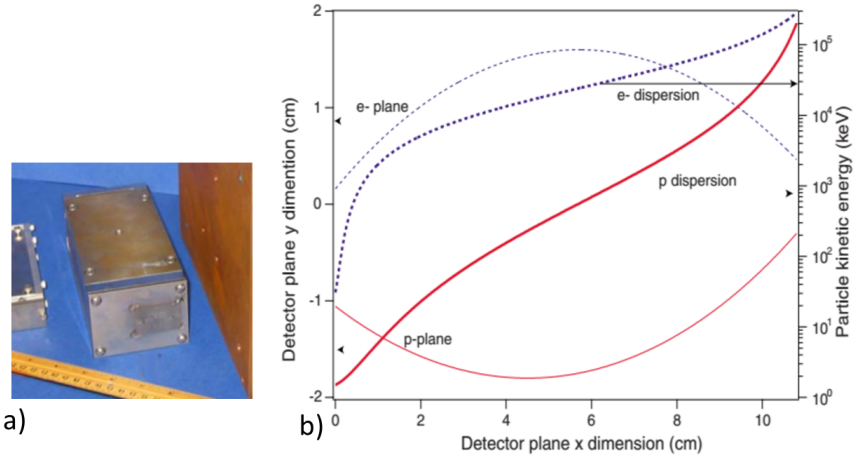

Figure 3.14: (Reproduced from [110].) Subplot a) illustrates the EPPS device, which is 2.5 in. wide, 3 in. tall, and 5 in. long (without additional shielding). Subplot b) demonstrates the dispersion planes and corresponding dispersion energies for electrons and protons; electrons and protons with energies from 0.1 to 100 MeV are measured.

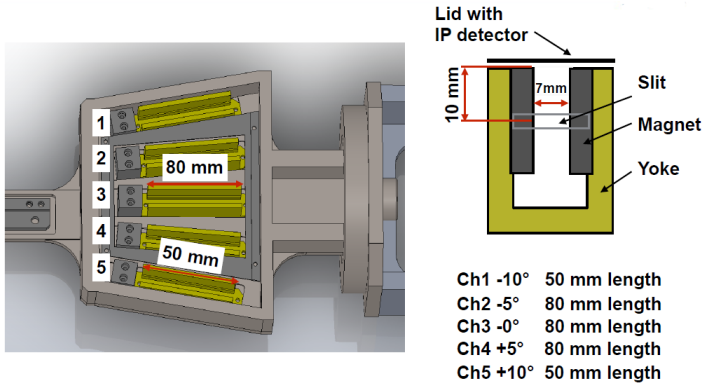

Figure 3.15: A schematic illustrating the OU-ESM. Five channels covering a total of 25° intercept escaping electrons, in which they are deflected by strong magnetic pairs onto BAS-MS image plate detectors.

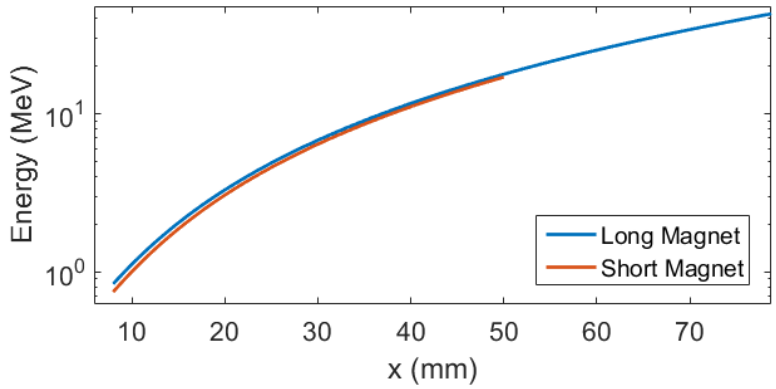

Figure 3.16: Electron dispersion charts for the OU-ESM with 0.45 T magnet pairs.

Image plate data for electrons must be corrected for the energy-dependent sensitivity of the fluorescent material; this is well documented, for example in plots such as Figure 3.17 [112]. Response to higher energy electrons can be found in citations such as [113].

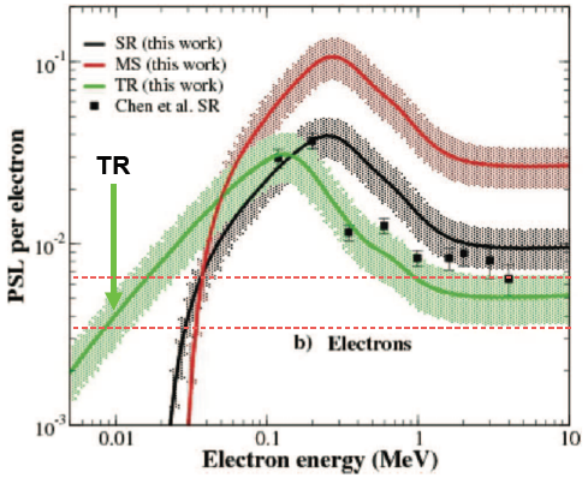

Figure 3.17: The PSL response of various image plate varieties to electron bombardment (reproduced from [112]). The three image plate varieties (BAS-TR, BAS-MS, and BAS-SR) are produced by Fuji and are characterized by different sensitivities.

3.3.7 Optical Probes

Optical probes are utilized heavily in plasma diagnostics, yielding such information as the local plasma density and the magnetic field structure of a plasma. At the OMEGA EP facility, a 4ω optical probe is used (utilizing the fourth harmonic of $\lambda = 1054$ nm pulses) [114].

The probe is 10 ps in duration, providing a temporal resolution on the hydrodynamic timescale, with an energy of 20 mJ which overcomes the background plasma emission at 263 nm.

The probe, after interacting with the plasma of interest, is split into multiple diagnostics such as interferometry, angular filter refractometry (AFR) (used to study plasma density profiles up to 10^{21} cm^{-3}), and polarimetry (used to measure laser-generated magnetic fields). These diagnostic legs are illustrated in Figure 3.18.

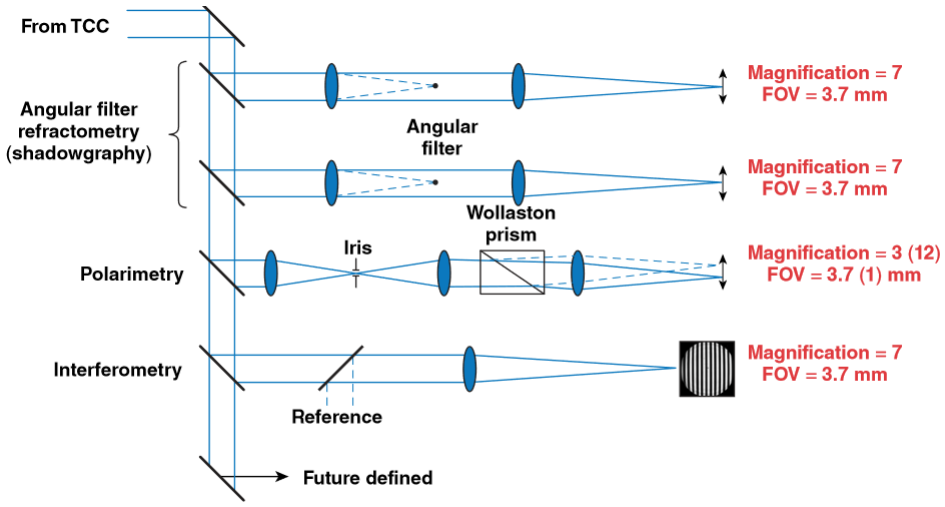

Figure 3.18: (Reproduced from [115].) The 4ω beam is split into multiple channels after interacting with the plasma of interest, allowing simultaneous AFR, polarimetry, and interferometry.

The AFR diagnostic leg measured the refraction of the probe beam through the plasma by relating the angle of defraction to the transverse gradient of the phase accrued by the ray according to

$$\theta_\alpha = \frac{\lambda_p}{2\pi}\frac{\partial\phi}{\partial\alpha} \tag{3.5}$$

where $\alpha = x$ or y is the spatial component of the refraction measured in the x-y plane, λ_p is the probe wavelength, and ϕ is the total phase accumulated by the probe ray passing through the plasma. The probe phase may be related to the plasma density, with refractive

index $n = (1 - n_e/n_{cr})^{1/2}$, yielding

$$\phi(x, y) = \frac{\pi}{\lambda_p n_{cr}} \int_{-\infty}^{\infty} n_e(x, y, z) dz, \tag{3.6}$$

where n_e is the plasma density and n_{cr} is the plasma's critical density for the probe laser wavelength. This may be inverted to solve for the density as a function of probe phase.

The AFR diagnostic measures the probe phase by mapping the refraction onto contours in the image plane introduced with an angular filter placed in the Fourier plane. The experimental AFR images are then analyzed using a series of calibration angles, and the density of the plasma in these regions may be interpolated.

The polarimetry leg of the 4ω diagnostic suite measures the rotation of the probe's linear polarization incurred as the beam passed through the magnetic fields of the plasma, with the phase difference related to the rotation α via

$$\alpha \approx \frac{e}{2m_e c} \int \frac{1}{n_c} n_e \mathbf{B} \cdot \mathbf{dl}. \tag{3.7}$$

Here, $\mathbf{B}$ is the magnetic field vector and $\mathbf{dl}$ is the path length vector. A quartz Wollaston prism is utilized to measure the polarization rotation by splitting the beam into orthogonal polarization components s and p, which are then imaged onto a CCD.

Two images representing the two polarization components of the laser are thus produced on the CCD, which are then carefully overlapped and combined in the form $(P - S)/(P + S)$, with a pre-determined scale factor utilized to convert the subtracted pixel value to polarization rotation angle.

3.4 Computational Modeling

Computational simulations are crucial to understanding the mechanisms involved in LPI experiments; they may provide insights regarding methods of energy absorption and transfer, field generation and interaction, and surface wave phenomena. There exist a large number of simulation schemes for modeling laser-produced plasma behavior, depending on the physics of interest and the timescales involved. Over nanosecond time scales, magnetohydrodynamic

(MHD) simulation methods are typically used to model phenomena such as shock dynamics; collective behavior in high density plasmas may be modeled with a Vlasov-Fokker-Planck (VFP) method if collisional physics plays a significant role; finally, PIC methods are typically utilized for small systems when the timescale of interest is small. Particle-in-cell (PIC) codes were used extensively to model the experiments described in this thesis.

3.4.1 OSIRIS

PIC codes model a plasma as kinetically evolving individual "super-particles" (representations of multiple physical particles); this re-scaling of the number of particles is possible because the Lorentz force depends only on the charge to mass ratio, so that a super-particle follows the same trajectory as an actual particle. The number of real particles per super-particle (or particles-per-cell (PPC)) is set sufficiently high to calculate the physical processes of interest with acceptable statistics.

The generalized PIC method involves the following steps: 1) the equations of motion are integrated, 2) the charge and current are interpolated onto the field grid, 3) the fields are calculated at the grid points, and 4) the particle motion is calculated from Maxwell's equations. For numerical stability and to resolve the physical and temporal scales of interest, parameters such as the spatial and temporal resolution as well as the number of super-particles must be chose such as to satisfy the Nyquist theorem, satisfy that the sampling rate exceed twice the maximum frequency of interest, and satisfy the Courant condition ($\Delta_t^{-2} \leq \Delta_x^{-2} + \Delta_y^{-2} + \Delta_z^{-2}$ in normalized units).

The PIC code OSIRIS [116] was the primary simulation tool utilized to model the experiments described in this thesis. OSIRIS is a fully explicit, multi-dimensional, massively parallel, relativistic simulation code developed by the OSIRIS Consortium. OSIRIS can be run in up to three spatial dimensions, albeit with heavy computing requirements. Many two and three dimensional OSIRIS simulations were run for the experiments herein described, using the University of Michigan's Advanced Research Computing - Technology Services as well as NASA's Pleiades Supercomputer.

Chapter 4

Radiation Measurements of Reconnection

4.1 Introduction

Magnetic reconnection has been observed in a variety of astrophysical phenomena, and has been re-created in the laboratory with the use of devices such as the MRX (see Section 1.3.1). The use of lasers to create conditions for magnetic reconnection was first accomplished in the recent past (see Section 1.3.2), using kiloJoule/nanosecond pulses focused to moderate intensities. However, the extremely energetic class of astrophysical phenomena involving relativistic effects have been inaccessible in the laboratory.

The experiments presented in this thesis extend the previous work on dual-laser driven reconnection to scenarios involving lasers focused to relativistic intensities. These are characterized by the generation of relativistic electrons emanating from the focal spot, and it is these electrons (along with the corresponding large magnetic fields) which form the inflow to the midplane where reconnection occurs.

Described in this Chapter are the results of X-ray emission measurements collected during experiments at the HERCULES, Titan, and the Omega EP laser facilities. A variety of X-ray emission diagnostics were employed, with the primary diagnostic being an imaging X-ray crystal (see Section 3.3.1) designed for the copper K_α wavelength of 1.54 Å.

It will be shown that these diagnostics provide confident indications that magnetic reconnection is driven in this relativistic regime, and results from a 3-D particle-in-cell (PIC) simulation will be presented to support the experimental findings.

A diagram indicating the magnetic and electric field orientations relevant to the regime of the experiments described in this thesis is given in Figure 4.1.

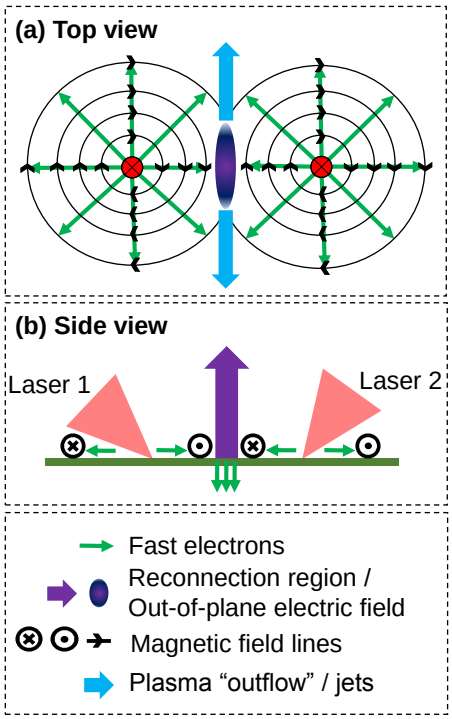

Figure 4.1: A top (a) and side (b) view of the interaction of two relativistic, short pulse lasers with a solid target. The corresponding relativistic surface electrons and associated azimuthal magnetic fields are shown, along with the target-normal electric field generated in the midplane. Electrons are accelerated into the target under the influence of this field, and along the outflow directions by motion of the newly reconnected magnetic field lines.

4.2 Previous work

Dual-laser driven reconnection experiments were first accomplished with pulses within the kiloJoule/nanosecond regime, focused to moderate intensities. The common configuration involved the irradiation of a thin metallic or plastic layer with the two beams focused with a separation $O(100\ \mu\text{m})$. In this regime, azimuthal magnetic fields are formed by the Biermann battery effect (see Section 2.2.3) or hot electron flows, and advect outward at hydrodynamic speeds while frozen to the plasma. In the midplane between the focal spots, the approaching magnetic fields are oppositely oriented, and driven reconnection occurs.

The main signatures of reconnection reported from these experiments involve one or

more of the following features: 1) a null region of the magnetic field in the midplane, 2) the formation of plasma outflows in the form of jets, 3) measurements of increased electron plasma temperatures in the midplane region, and 4) a change in the magnetic field topology consistent with reconnecting magnetic field lines.

A review of previous work in the kiloJoule/nanosecond regime was presented in Section 1.3.2. There it was seen that the majority of measurements probing the magnetic field structure in laser-plasma reconnection experiments have utilized proton probing, wherein a short-pulse, high-intensity beam is used to generate target normal sheath acceleration (TNSA) protons which propagate through the plasma during reconnection. Their deflection is recorded on radiochromic film and the magnetic field through which they have passed may be reconstructed as a function of the proton energy (thereby providing temporal resolution).

For the experiments outlined in this thesis, proton probing was not used. This is due to both the complications of short-pulse co-timing as well as the lack of availability of a third short duration beam at the laser facilities used. Thus, a unique aspect of the experiments outlined in this Thesis is the utilization of a spherically bent X-ray crystal to detect evidence of reconnection.

4.3 Experimental rationale

An integral component in the magnetic reconnection process is the formation of a strong, target-normal electric field localized in the midplane. Associated with this field is a population of electrons which are accelerated into the density gradient. These electrons have been observed in simulations to acquire energies much higher than the ambient plasma's thermal energy [39], and their effect on the plasma may be used as an indicator that reconnection occurs.

For the HERCULES, Omega EP, and Titan experiments discussed in this thesis, the primary diagnostic approach to detecting signatures of reconnection is the use of a spherically bent X-ray crystal. Electrons driven into the target within the midplane may easily be accelerated to tens or hundreds of kiloVolts by the reconnection electric field [39]. As they propagate into the plasma, they undergo collisions and may excite atomic transitions.

Thus, an imaging X-ray crystal designed to focus only a small range of wavelengths surrounding copper's K_α emission is able to detect the X-ray emission signatures of reconnection. Copper foil targets were also irradiated on Omega EP which had a 90-degree bend, located such that outflowing electrons with an emission angle ≤ 21.8 degrees above the target surface would heat the copper, resulting in detectable K_α emission.

Another radiation diagnostic employed was an X-ray pinhole camera (XRPHC). Utilized on Omega EP, the device imaged onto a charge injection device (CID) which is sensitive to photons with energies of 2-6 keV [117]. In addition to verifying the focal spot separation, the XRPHC signal may be compared to images formed by the K_α crystal. If K_α emission is detected from the midplane but no appreciable signal is detected by the XRPHC within the same region, it is strong evidence that the observed signal is emitted by a process other than collisional heating of two colliding plasmas (which results in bright, broadband X-ray spectra).

To compliment the XRPHC, a single photon counting spectrometer (SPC) (Spectral Instrument series 800 CCD) was utilized during the Omega EP experiments to measure K-shell emissions from 5 - 25 keV. This may allow for an estimate of the copper K-photon spectrum and yield compared to lower-energy electrons. To achieve better resolution between the K_α and K_β, an X-ray crystal spectrometer oriented in the von Hamos configuration and specifically designed to measure K-lines from copper and zinc was utilized on Omega EP. This allowed comparisons between the K_β and K_α yield, providing estimates of the temperature of the plasma from which the K-photons originate (see Section 2.4.3).

A generalized chamber schematic is provided in Figure 4.2, demonstrating the two-beam geometry for the configuration in which the target front-side is imaged.

These measurements of X-ray emissions provide significant evidence for magnetic reconnection. To support the findings, results from a 3-D PIC simulation will be provided to demonstrate that reconnection occurs when driven by short-pulse-generated relativistic electrons. The formation of a target-normal electric field and acceleration of electrons into the midplane will also be demonstrated.

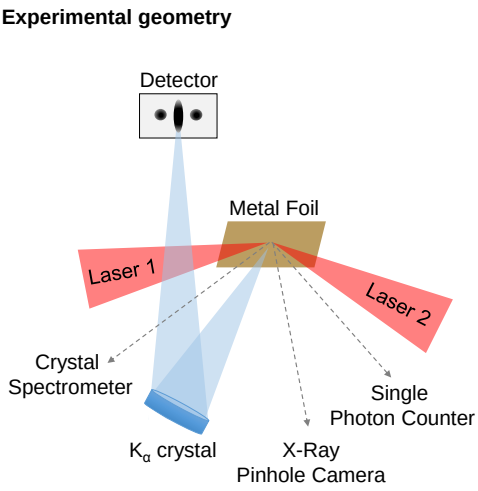

Figure 4.2: A generalized chamber schematic for the experiments discussed in this Chapter. A spherical X-ray crystal is used to image K_α emission onto a CCD (HERCULES) or image plate (Omega EP and Titan).

4.4 Experimental setup: HERCULES

The HERCULES laser facility at the University of Michigan, a Ti:Sapphire system with wavelength of $\lambda = 800$ nm and pulse durations of 40 fs FWHM was utilized. The amplified spontaneous emission (ASE) contrast was reduced with the Cross-Wave Polarization (XPW) [118] correction technique to 10^{-11}. An f/3 paraboloidal mirror was split along its symmetry axis with one half vertically motorized to allow two wavefront-corrected laser foci to be separately adjusted between $0 - 400\mu$m. With a 4 inch diameter, 100 TW beam incident upon the paraboloid, focal spot S_1 had an approximate FWHM area of 174 μm^2 containing 37.5% of the beam energy, while focal spot S_2 an approximate FWHM area of 337 μm^2 and 62.5% of the beam energy. Both spots therefore had approximately equal focused intensities of $2{\times}10^{19}$ Wcm^{-2}. The chamber schematic is shown in Figure 4.3.

A spherically bent, quartz crystal crystal (2131 Miller indices) with a $2d = 3.082$Å lattice spacing was utilized to image the copper K$_\alpha$ emission of 8.04 keV, with Bragg angle of 88.7°. The crystal was positioned 242 mm from the target and created an image at 1260 mm, yielding a magnification of 5.2 onto an Andor iKon-M BR-DD CCD. The CCD had 13 μm pixels and at a quantum efficiency of 45% for copper K_α photons, yielding a final spatial resolution of 15 μm. A lead and acrylic aperture was positioned to block the line-of-sight of

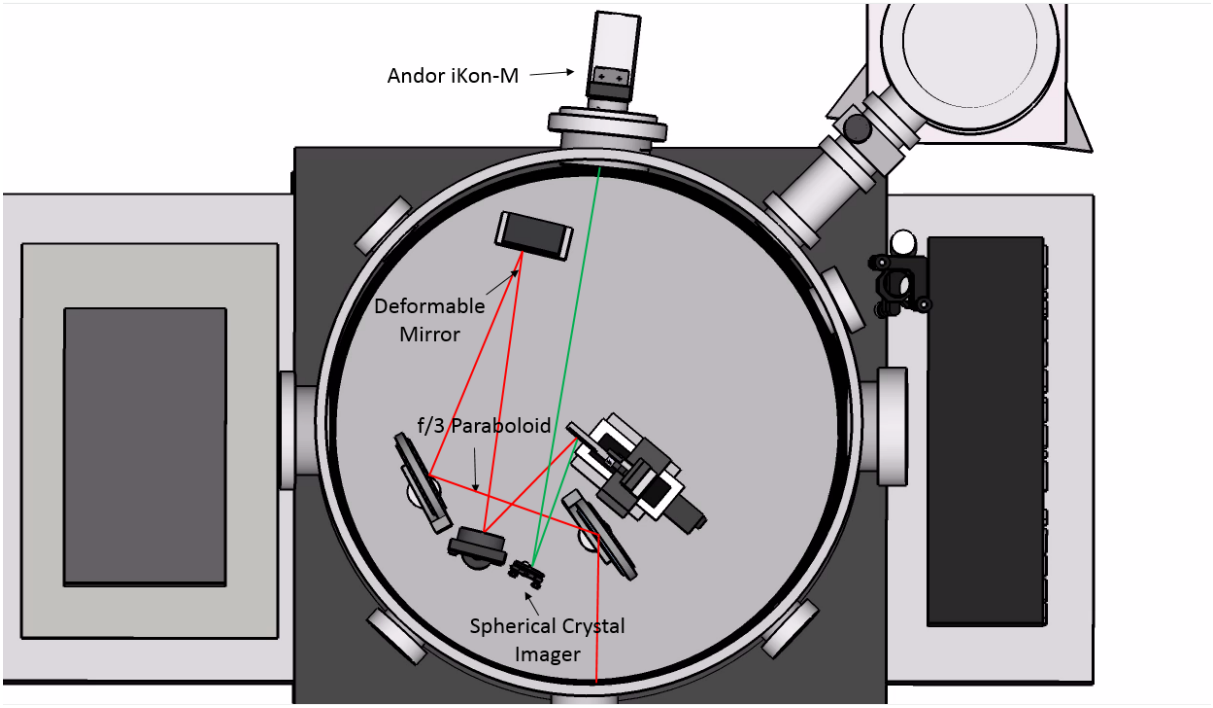

Figure 4.3: The HERCULES chamber schematic for the dual-beam experiments.

the target.

A variety of diagnostics were employed to ensure both beam quality and interaction strength. A leak-through of the main pulse was directed outside the experimental chamber, where multiple beam-splitters directed the beam to a near-field monitor, far-field monitor, and energy diode. These diagnostics respectively monitored wavefront quality, beam pointing fluctuations, and relative laser energy shot-to-shot.

An X-ray *p-i-n* diode inside the chamber and gamma-ray detector (scintillator and fast photomultiplier tube) housed outside the chamber monitored the front and backside radiation caused from collisional ionization and bremsstrahlung. Each shot-run began with a focusing procedure whereby the two overlapped laser pulses irradiated bulk copper with varied target positions along the beam propagation axis, such that the radiation diagnostics revealed an optimal focal plane position for strongest interaction.

4.5 Experimental setup: Omega EP

The Omega EP facility generated two 20 ps pulses with energies of either 500 J/pulse or 1 kJ/pulse and focal spot distributions with FWHM radii of 13±1 μm ($I = 1.2 \times 10^{18}$ or 2.5×10^{18} Wcm^{-2}). The Omega EP experiments were intended to compliment the results from HERCULES, given its wider range of available diagnostics and longer pulse duration at similar focused intensity (making time resolved measurements possible).

A spherically bent X-ray crystal was utilized on Omega EP as the primary diagnostic for observing evidence of reconnection. Nearly identical to that used on the HERCULES facility, the quartz crystal had a 50 cm radius of curvature, $2d = 3.082$ Å lattice spacing, and 2131 Miller indices. To protect the crystal from laser damage and debris, a 50 μm aluminized mylar blast shield was used. The crystal imager imaged with a magnification of ≈ 10 onto an image plate (IP) positioned in the opposing diagnostic port, satisfying the Bragg condition of 1.31°. The IP utilized a lead collimator to minimize X-ray background, and the line-of-sight was blocked. The final image resolution was 10 μm.

Depending on the experiment, the X-ray crystal viewed either the front or the rear of the target surface, slightly off-axis.

Three individual X-ray pinhole cameras (XRPHC) were employed. The devices imaged onto a charge injection device (CID) which detects photons between 2-6 keV [117]. Each XRPHC was filtered by 1.5 mm of beryllium. The pinhole-to-image distance was 648 mm, and the pinhole-to-target distance was 162.5 mm, resulting in a final magnification of 4. The pinhole diameter was 10 μm.

To compliment the XRPHC, a single photon counting spectrometer (SPC) (Spectral Instrument series 800 CCD) was utilized during the Omega EP experiment to measure the K-shell emission from 5-25 keV.

Figures 4.4, 4.5, and 4.6 depict the three experimental geometries utilized on Omega EP, displaying 2-D projections of the spherical chamber, listing the diagnostics utilized and their angular positions in spherical coordinates, and the incoming beam angles. The identifying acronyms for the diagnostics are defined in Table 4.1.

Table 4.1: Omega EP Diagnostic Acronyms

SCI	Spherical Crystal Imager
UFXRSC	Ultrafast X-Ray Streak Camera
EPPS	Electron Proton Positron Spectrometer
IP	Image Plate
SPC	Single Photon Counter
XRPHC	X-Ray Pinhole Camera
OU-ESM	Osaka University Electron Spectrometer
ZVH	Zinc Von Hamos (Crystal Spectrometer)
UFXRSC	UltraFast X-Ray Streak Camera

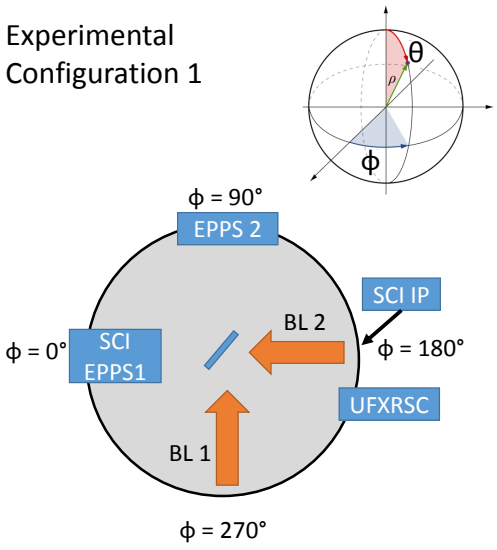

Ten-inch-manipulator (TIM) Diagnostics

Diagnostic Description	TIM	Port	Theta	Phi
SCI	10	2	27	0
UFXRSC	11	9	39	189
EPPS 1	12	45	90	0
SCI IP Holder	13	87	153	180
EPPS 2	14	48	90	90

Fixed Diagnostics

Diagnostic Description	Port	Theta	Phi
SPC	91	92.25	196.65
XRPHC 39	39	74	253
XRPHC 47	47	95.13	60
XRPHC 52	52	90	215.1

Incoming Beam Angles (From Target Normal)

Beam	Theta	Phi
BL 1	-55	55
BL 2	-55	-55

Target Orientation Angles

Theta	Phi
52	230

Figure 4.4: The diagnostic positions and beam pointing conditions for Experimental Configuration 1. The acronyms are defined in Table 4.1.

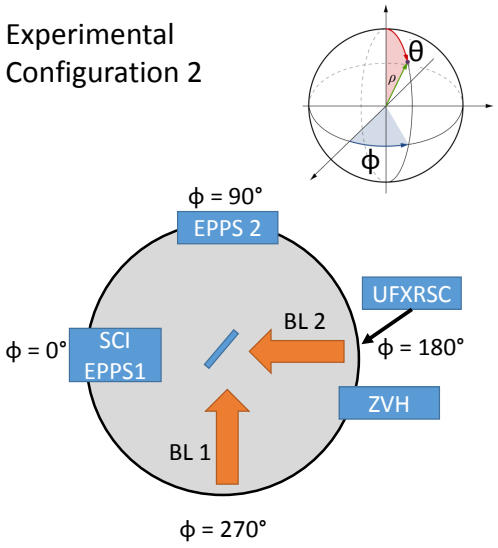

Ten-inch-manipulator (TIM) Diagnostics

Diagnostic Description	TIM	Port	Theta	Phi
SCI	10	2	27	0
ZVH	11	9	39	189
EPPS 1	12	45	90	0
UFXRSC	13	87	153	180
EPPS 2	14	48	90	90

Fixed Diagnostics

Diagnostic Description	Port	Theta	Phi
SPC	91	92.25	196.65
XRPHC 39	39	74	253
XRPHC 47	47	95.13	60
XRPHC 52	52	90	215.1

Incoming Beam Angles (From Target Normal)

Beam	Theta	Phi
BL 1	-55	55
BL 2	-55	-55

Target Orientation Angles

Theta	Phi
52	230

Figure 4.5: The diagnostic positions and beam pointing conditions for Experimental Configuration 2.

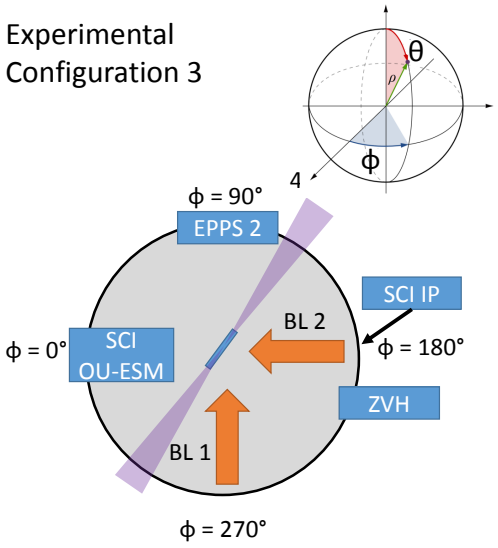

Ten-inch-manipulator (TIM) Diagnostics

Diagnostic Description	TIM	Port	Theta	Phi
SCI	10	2	27	0
ZVH	11	9	39	189
OU-ESM	12	45	90	0
SCI IP Holder	13	87	153	180
EPPS 2	14	48	90	90

Fixed Diagnostics

Diagnostic Description	Port	Theta	Phi
SPC	91	92.25	196.65
XRPHC 39	39	74	253
XRPHC 47	47	95.13	60
XRPHC 52	52	90	215.1

Incoming Beam Angles (From Target Normal)

Beam	Theta	Phi
BL 1	-26.1	33
BL 2	66.8	-56
4ω	90	90

Target Orientation Angles

Theta	Phi
35.9	222.7

Figure 4.6: The diagnostic positions and beam pointing conditions for Experimental Configuration 3.

For experimental configurations 1 and 3, 50 μm thick copper foils were used. The foils utilized during experimental configuration 1 had a 90-degree bend in the foil in order to intercept outflowing electrons. For experimental configuration 2, a specialized target manufactured by General Atomics' Inertial Fusion Technologies Program was utilized. The composition of these targets are described in Figure 4.7. The primary intention of using this target geometry in Experiment 2 was in extracting the temporal duration of the midplane K_α emission, which is the subject of Chapter 5. Experimental configuration 3 was utilized to observe the plasma with an optical probe.

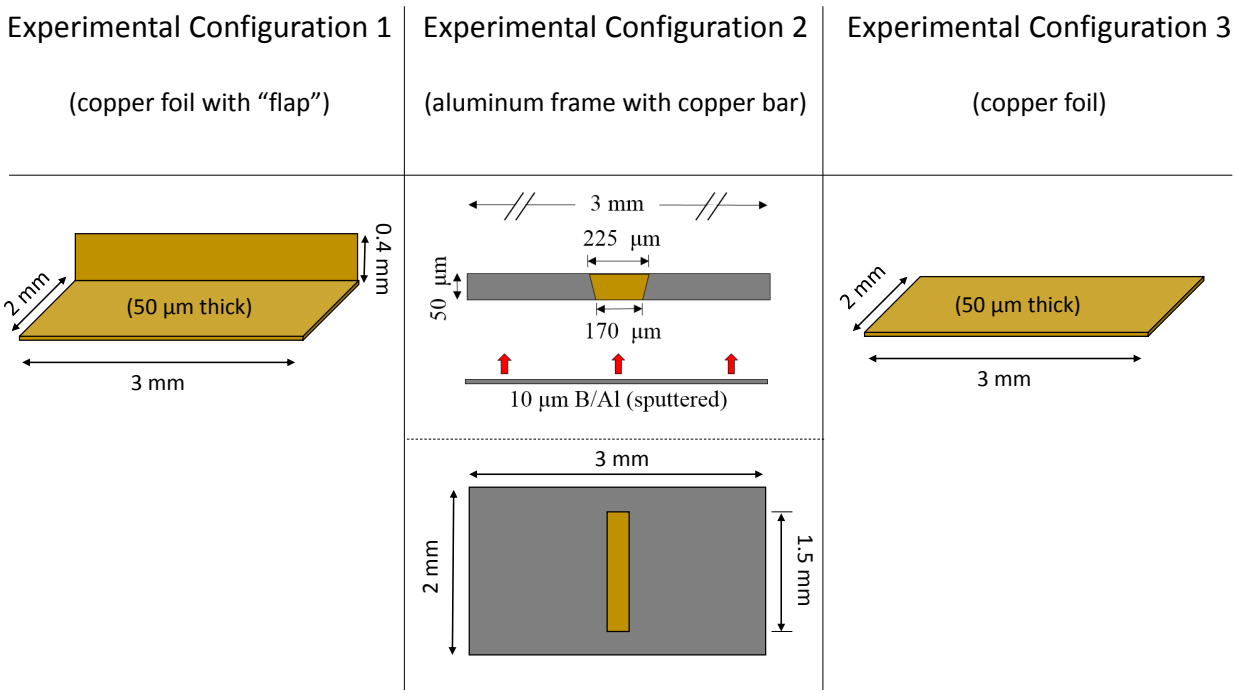

Figure 4.7: The target geometries utilized in Experimental Configurations 1, 2, and 3 of the Omega EP experiments.

4.6 Experimental setup: Titan

The Titan laser was used with pulse durations of both 0.7 ps and 10 ps, with corresponding nominal energies of 140 J and 240 J, respectively. The energy was split into two pulses and focused by two separate f/3 paraboloids, resulting in nominal focused intensities of 6×10^{19} Wcm^{-2} and 7×10^{18} Wcm^{-2}, with a 15 μm FWHM focal spot size.

An image of the experimental chamber is provided in Figure 4.8, along with the two target orientations utilized during the experiment.

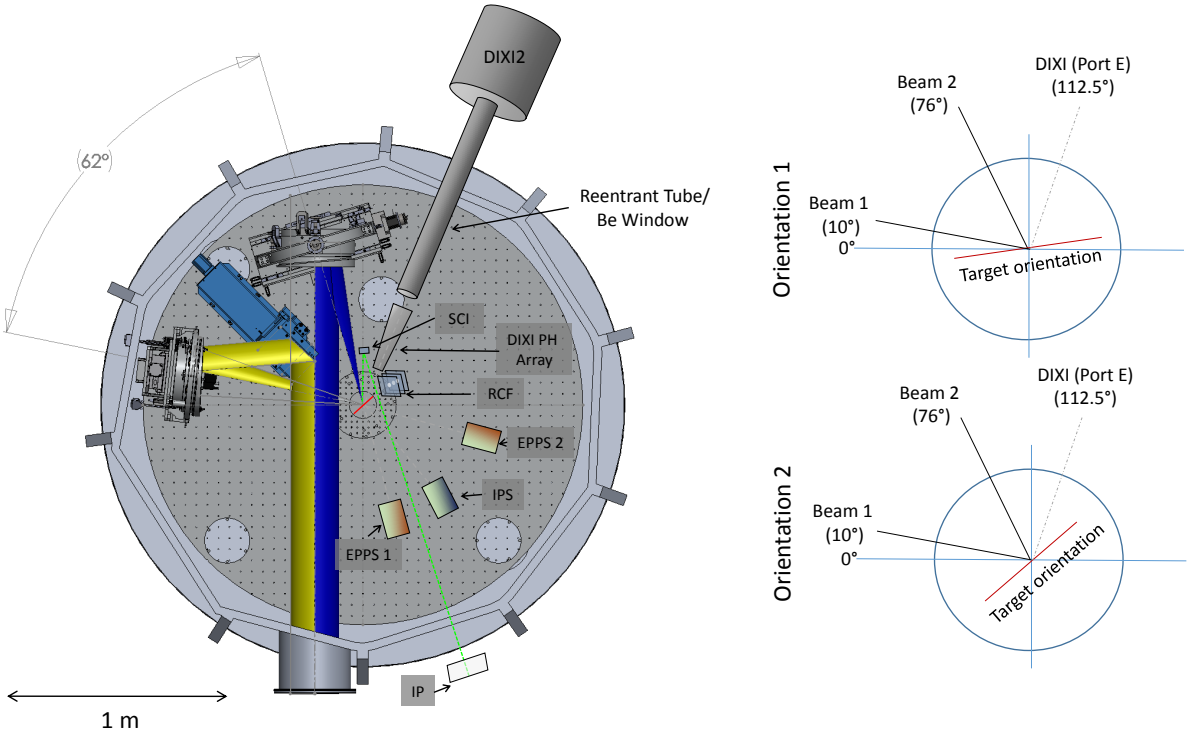

Figure 4.8: The Titan chamber configuration demonstrating the two-beam configuration. The two target configurations utilized are demonstrated on the right.

The spherical X-ray crystal utilized on HERCULES was also used on Titan, with an object distance of 230 mm and an image distance of 1168 mm. The crystal was protected by a 12.5 μm polyethylene blast shield. A BAS-MS image plate filtered with 12.5 μm of copper was used as the detector.

4.7 Results

4.7.1 K_α Images

The two HERCULES beams were scanned in separation from $0 - 500$ μm, resulting in K_α images featuring two bright sources corresponding to local plasma heating, and centered between these an extended, enhanced region of K_α emission. Representative images are shown in Figure 4.9.

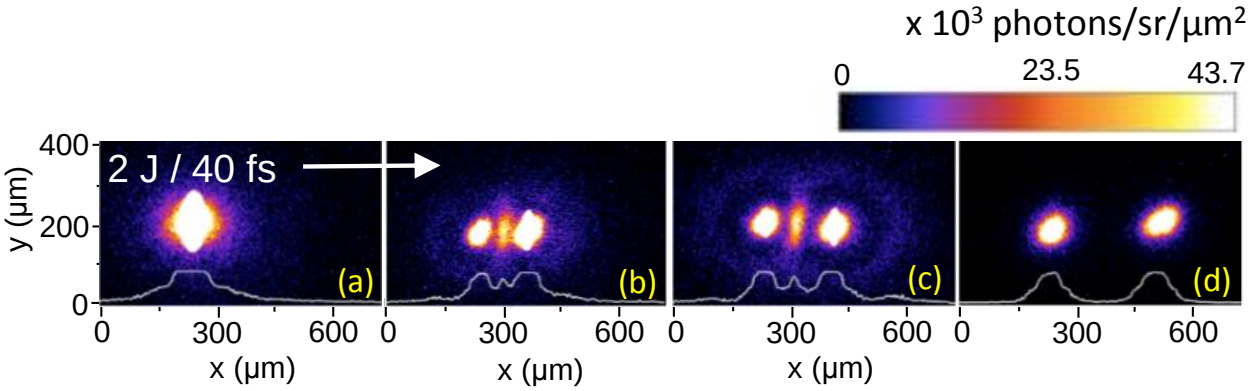

Figure 4.9: Copper K_α images resulting from a separation scan performed on the HERCULES laser. The focal spot separations (from left to right) are 0 μm, 140 μm, 160 μm, and 300 μm.

The copper K_α emission additionally revealed weak halos of K_α surrounding each focal spot (R = 210 μm), experimentally observed previously in femtosecond, relativistic laser-plasma interactions [119]. The enhanced mid-plane reconnection is significantly more intense (10×) than the summation of the two individual halos within this region (found by blocking either half of the beam's near-field before entering the target chamber), indicating an increased electron current into the copper target in the mid-plane due to the formation of the reconnection current sheet. The results are shown in Figure 4.10.

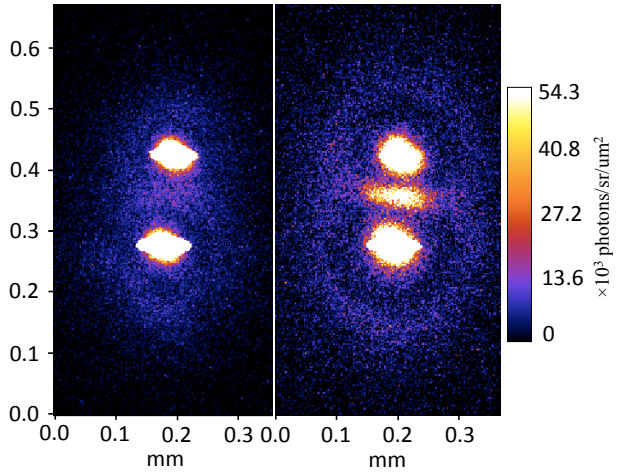

Figure 4.10: (Left) The summation of K_α images corresponding each beam half alone. (Right) The K_α image corresponding to both beams simultaneously fired.

The dimensional characteristics of the current sheet may reveal properties of the re-

connection process. Figure 4.11 plots the full-width-at-half-maximum (FWHM) width and length of the current sheet as a function of beam separation.

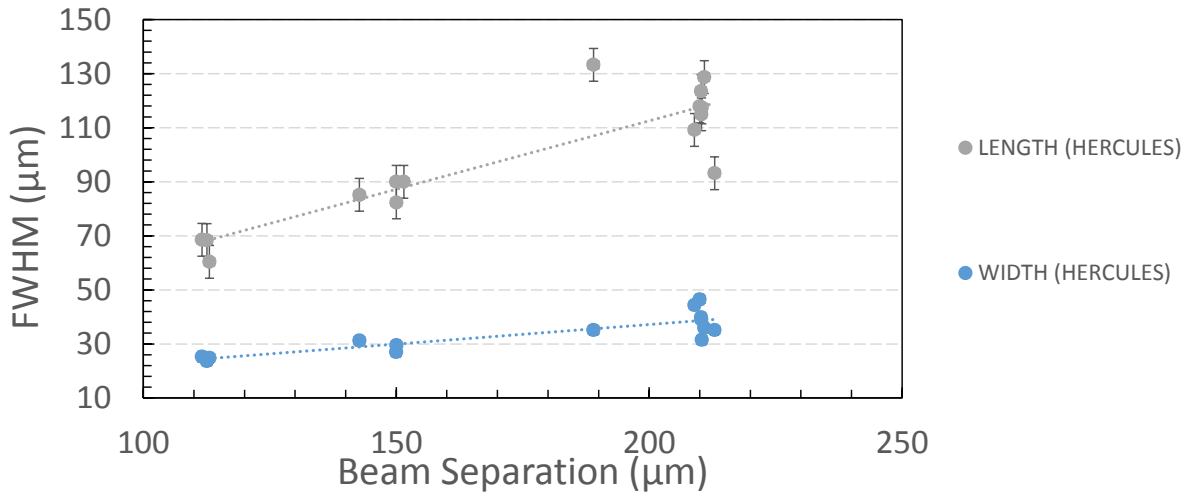

Figure 4.11: The FWHM dimensions of the current sheet as measured from the K_α images collected on the HERCULES laser.

Both dimensions of the current sheet increase approximately linearly with separation. The increasing width may be related to the electron bounce width as it crosses the current sheet and is deflected by the alternating magnetic fields. The increasing length may correspond to the increasing radius of curvature of the magnetic field lines, which is a characteristic length scale of the reconnection event.

The relative efficiency of the reconnection can be implied by integrating the midplane signal. The result of comparing this to the total averaged K_α signal emitted from the interaction sites is plotted in Figure 4.12.

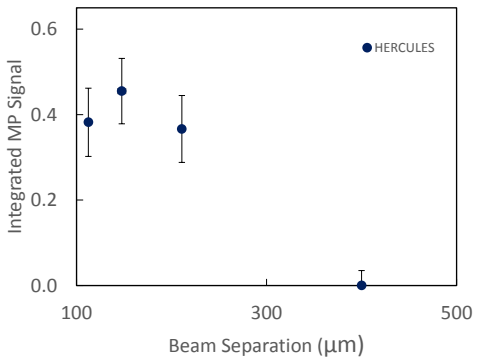

Figure 4.12: The integrated K_α signal from the midplane regions observed during the HERCULES focal spot separation scan. The values are normalized to the averaged integrated K_α from the interaction sites, which was measured by filtering the CCD until the focal spot regions did not result in saturation.

At sufficiently large separations, reconnection is suppressed by the combination of the 1/r dependency of the azimuthal magnetic field magnitude and the falloff in current density at the midplane. For sufficiently small separations, reconnection is likely suppressed due to more severe electron profile density perturbations in the vicinity of the reconnection region, which may disrupt the evolution of the current sheet (this is reflected in the simulation results to be presented). An optimal separation is found near a separation of 150 μm, where the suppressing effects are balanced.

Shots were taken on Omega EP with a similar beam and target geometry. K_α images were collected at Omega EP using Experimental Configuration 1. The spherical crystal imaged from a glancing angle, producing skewed images (Figure 4.13 a). The perspective was corrected by utilizing a bi-cubic interpolation (Figure 4.13 b).

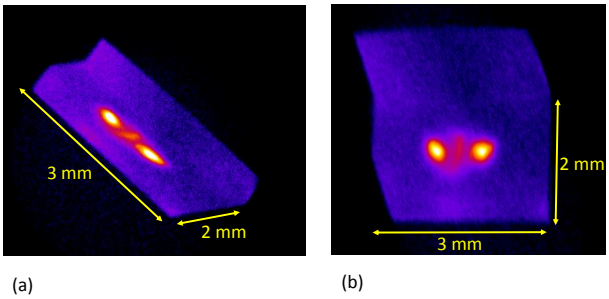

Figure 4.13: (a) The K_α image produced by the spherical crystal. (b) The processed image correcting for the skewed perspective.

Applying the correction for photostimulated luminescence (PSL), the results from experiments with 500 J and 1 kJ with a 20 ps pulse duration is plotted in Figure 4.14.

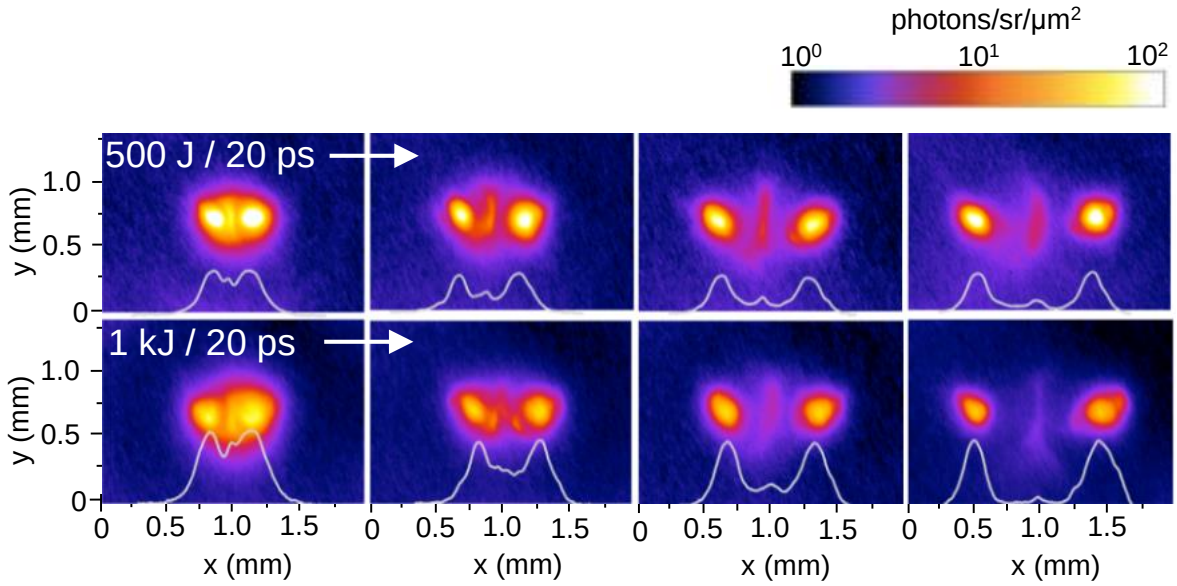

Figure 4.14: K_α images collected during a focal scan at Omega EP. The top row represent shots taken with 500 J/pulse, while the bottom row correspond to 1 kJ/pulse. The scans are plotted on a logarithmic scale.

The dimensional features and integrated midplane signals are measured and reported in Figure 4.15 and Figure 4.16.

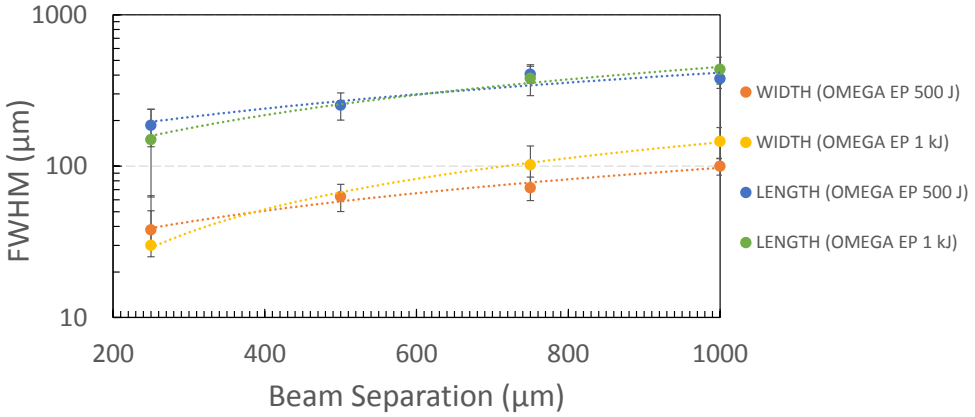

Figure 4.15: The FWHM dimensions of the current sheet as measured from the K_α images collected on the Omega EP laser, for both 500 J/pulse and 1 kJ/pulse.

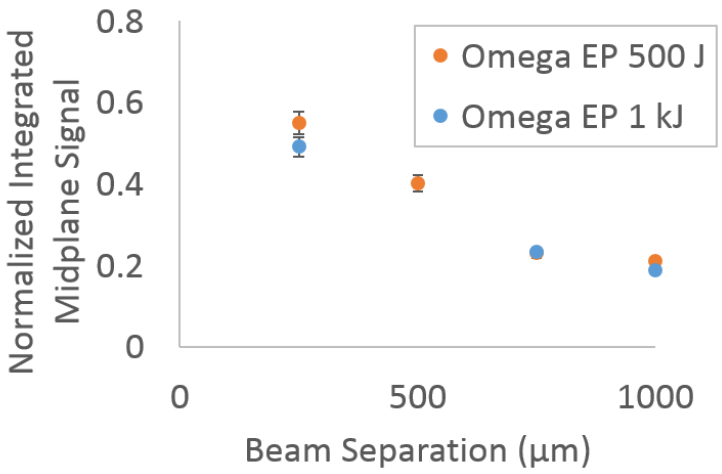

Figure 4.16: The integrated K_α signal from the midplane regions observed during the Omega EP focal spot separation scans. The values are normalized to the averaged integrated K_α from the interaction sites in order to determine the efficiency of reconnection. In real units and assuming a crystal integrated reflectivity of $\rho = 0.04$ (as for the HERCULES crystal), the average integrated emission from the focal spot region for the 500 J/pulse case is 6×10^9 photons and in the 1 kJ/pulse case is 5×10^9 photons.

From the dimensional analysis, an increasing trend in current sheet width and length can be seen similar to the HERCULES laser parameters. The integrated midplane signal decreases with increasing separation, but was not seen to decrease for small separations. Further decreasing the focal separation would be expected to reveal an optimal separation for maximized midplane signal.

The similarity of the integrated midplane signals presented in Figure 4.16 between the two beam energies can potentially be explained by a saturation of K_α emission, whereby the increased flux of reconnection electrons does not lead to a significantly increased K_α emission. Alternatively, it is possible that the increased beam energies lead to higher magnitude reconnection electric fields, which may accelerate electrons to energies sufficiently high such that K_α emission has a suppressed cross section (see the discussion in Section 2.4).

No emission was observed from the 90° bend in the copper foil target (depicted in Figure 4.7), indicating that either the outflow electrons are too few to cause significant emission, that they are insufficiently energetic (< 8.04 keV), or that the outflow is directional and inclined significantly from the target plane, at an angle ≥ 22 degrees. Previous kiloJoule/nanosecond magnetic reconnection experiments ([31,32]) found that the outflow jets are highly collimated

an angled $\sim 30^\circ$ from the target surface.

During Experimental Configuration 3 on Omega EP, the spherical crystal viewed the 50 μm copper target from the rear. This also revealed two-spot and midplane features. By calculating the relative mid-plane signal from the target front-side and back-side (for constant focal separation), it was estimated that the K_α photons emanate from depths of $\gtrsim 10$ μm from the front-side. Associating this point with the CSDA (continuously slowing down approximation) electron range, it is roughly estimated that electrons are accelerated to energies of $\gtrsim$100 keV by the reconnection electric field.

The spherical X-ray crystal was utilized on the Titan system. Due to progressive damage to one of the focusing paraboloids, beam energy was not constant shot-to-shot. Since the paraboloid's reflectivity was not measured after each shot, the reflectance of the damaged mirror was measured at the conclusion of the experimental campaign to be 20%, and a linear degradation assumed.

The shift of the midplane is seen to correspond to the ratio of beam energies, as shown in Figure 4.17, expected to occur in the region where the azimuthal magnetic fields generated from either interaction site are equal in magnitude (*i.e.*, the location of the magnetic null).

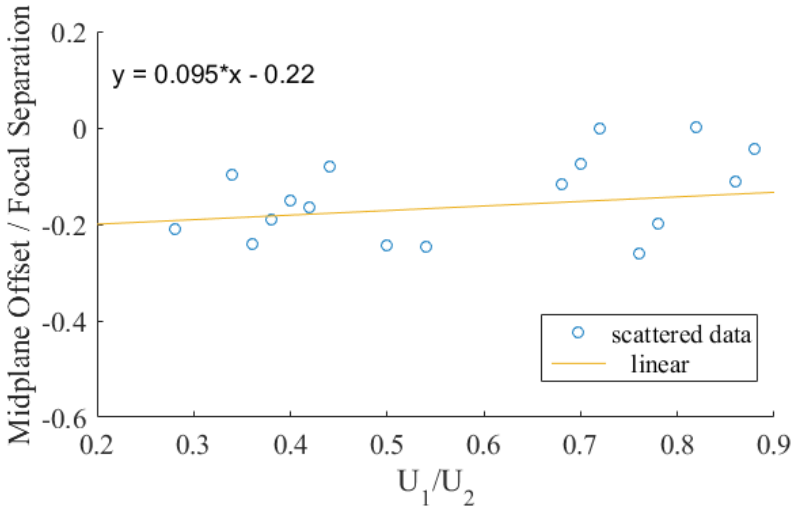

Figure 4.17: The offset of the midplane K_α emission (normalized to focal spot separation) as a function of the energy imbalance, assuming linear degradation of the beam energy from 100% to 20% over the duration of the experiment.

Despite the significant energy imbalance, the localized enhancement of K_α seen in the

previous two experimental facilities was also observed consistently on Titan, but with a shift of the signal from the midplane toward the region corresponding to the lower-energy beam. A summary of representative K_α images recorded during the Titan experiment is provided in Figure 4.18.

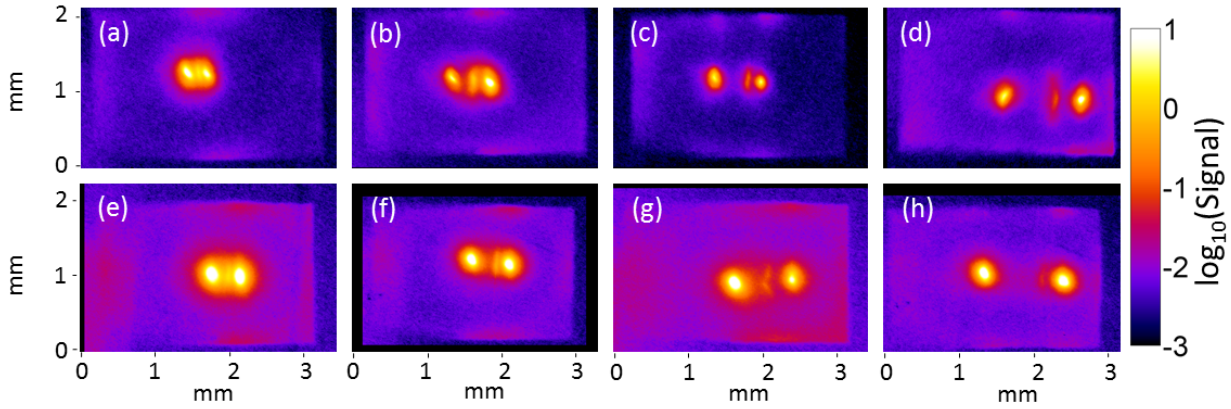

Figure 4.18: Logarithmically scaled copper K_α images from the separation scan experiment conducted with the Titan laser. The top row (a-d) corresponds to the 10 ps pulse setting and the bottom row (d-h) corresponds to the 0.7 ps pulse setting.

Figure 4.19 summarizes the dimensional characteristics of the K_α signal and the integrated midplane K_α signal.

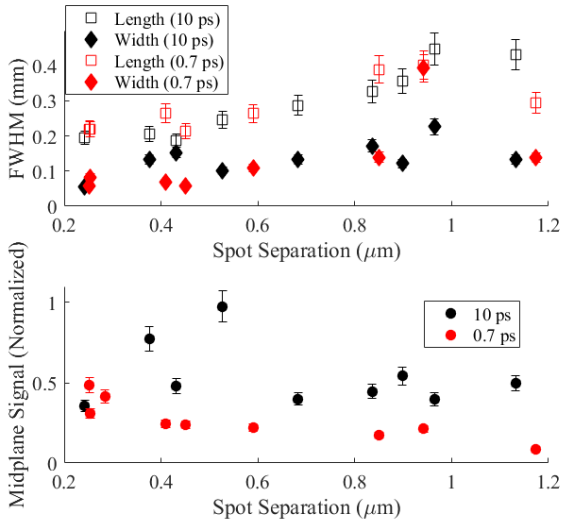

Figure 4.19: (Top) Full-width-at-half-maximum dimensional characteristics of the midplane K_α emission. (Bottom) Integrated midplane signals normalized by the average value of the integrated K_α signal from the interaction sites.

While the dimensional characteristics of the midplane K_α emission recorded with the Titan laser was not determined as accurately by a linear trend (compared to the HERCULES and Omega EP data), a general increase may be seen with increasing beam separation. The variation was likely due to the limited stability of the laser parameters and relative beam arrival time. Additionally, while the integrated midplane K_α signal displays significant fluctuation, it is apparent that the high-energy pulse case resulted in higher midplane K_α signal, while in both cases a decrease is seen with increasing pulse separation.

By plotting the results from each facility simultaneously, it is apparent that the data fits an approximately linear trend in spot separation versus current sheet length and width. This is plotted in Figure 4.20.

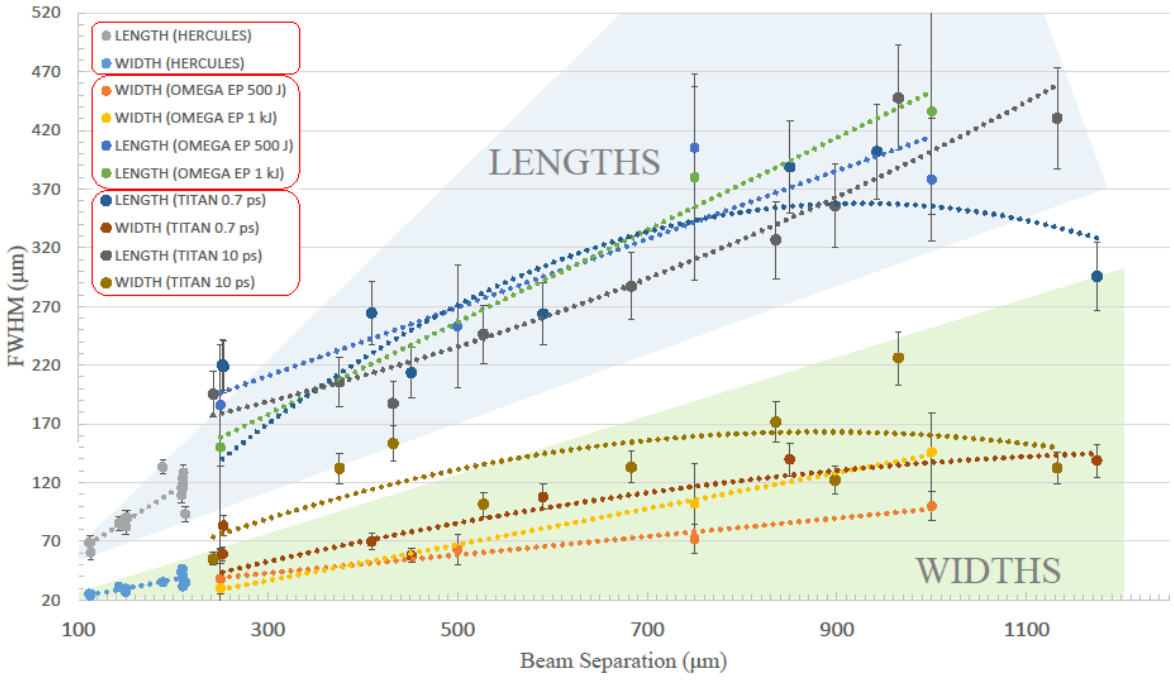

Figure 4.20: The dimensional characteristics of the K_α image data plotted for all datasets collected from HERCULES, Omega EP, and Titan. The lines are drawn as a visual aid only.

If the beam separation is extended to zero, then the trends presented in Figure 4.20 predict a width $\delta = 14 \pm 10$ μm and a length $L = 33 \pm 24$ μm.

Measurements of the aspect ratios of the diffusion regions across all experimental platforms are plotted in Figure 4.21.

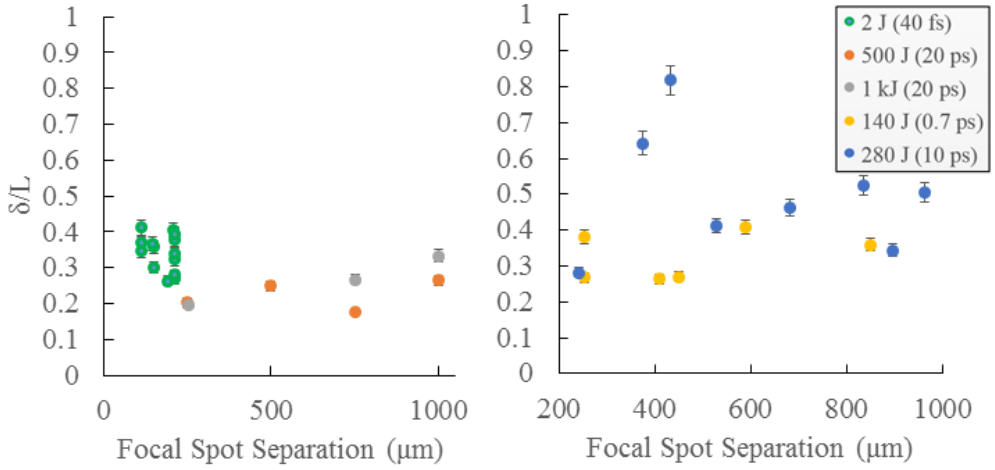

Figure 4.21: The aspect ratios of the diffusion region as measured from the K_α images for the HERCULES and Omega EP experiments (left) and the Titan experiments (right).

As is demonstrated in Figure 4.20, the averaged measured aspect ratio from the HERCULES experiments was $\delta/L = 0.35 \pm 0.05$, while for the Omega EP shots, $\delta/L = 0.225 \pm 0.05$ for the 500 J/pulse case and $\delta/L = 0.26 \pm 0.05$ for the 1 kJ/pulse case. The aspect ratios measured from the Titan experiments demonstrate a significant degree of scattering, but values of $\delta/L \approx 0.3$ were common for the 140 J/pulse case and $\delta/L \approx 0.45$ were common for the 280 J/pulse case. The exceptionally high aspect ratios measured (approaching $\delta/L \sim 1$) on Titan coincided with the greatest energy imbalances, and therefore are expected to be incomparable to the data measured from HERCULES and Omega EP.

4.7.2 X-Ray Pinhole Cameras

An X-ray pinhole camera with a front-view of the targets was utilized in Experimental Configuration 1 during the focal spot scan. It had a magnification of 4 with an energy range of $2 - 6$ keV. A summary of the X-ray pinhole data collected during the focal separation scan is presented in Figure 4.22.

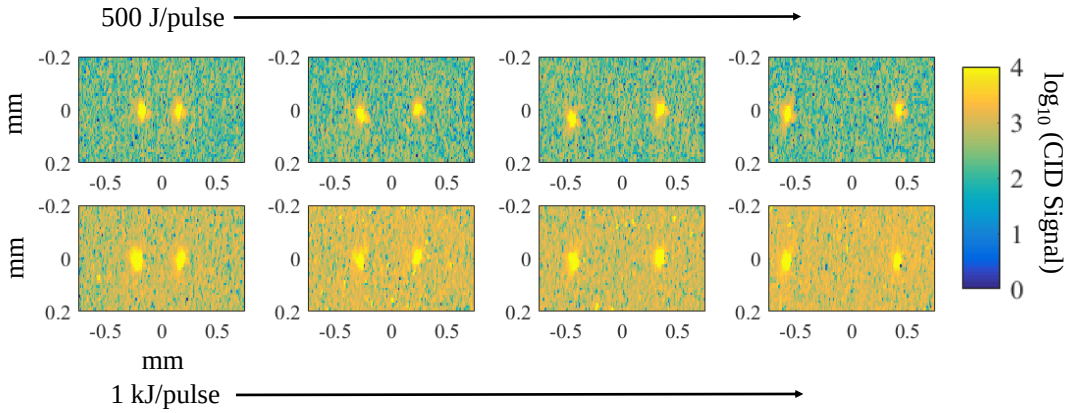

Figure 4.22: The XRPHC images collected during the focal separation scan in Experimental Configuration 1. The images are plotted on a logarithmic scale.

The broadband X-ray emission originating from either focal spot is ~ 2 orders of magnitude above background in either case, with increased noise in the case of 1 kJ/pulse. Integrated lineouts of the background-removed XRPHC signal are plotted in Figure 4.23.

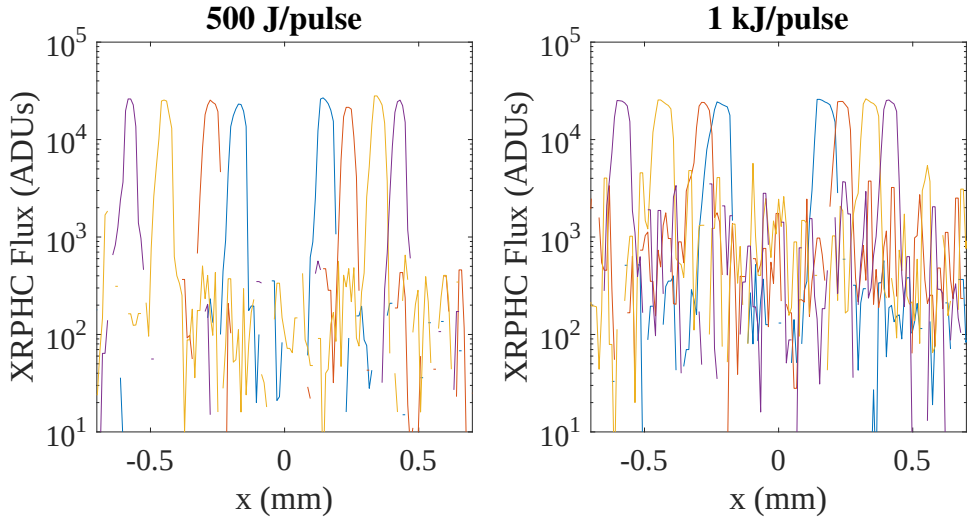

Figure 4.23: Background-subtracted lineouts of the XRPHC data collected during the focal spot separation scan in Experimental Configuration 1.

The decreased signal-to-noise ratio with higher laser energy is a common deterrent with radiation diagnostics, in this case caused by the surrounding plasma having been heated to a higher temperature and emitting broadband X-rays.

The XRPHC images verified the focal spot separations, and the lack of broadband x-ray signal from the midplane confirms that the observed K_α is not consistent with collisional

heating but rather consistent with energetic electrons accelerated into the plasma density gradient within a localized region.

4.7.3 Zinc Von Hamos

The Zinc Von Hamos (ZVH) X-ray crystal spectrometer was used during Experimental Configuration 2 on Omega EP (Target Design 2), during which it measured copper $K_{\alpha,\beta}$ spectra from the target front-side. The crystal spectrometer is designed to resolve zinc $K_{\alpha,\beta}$ emissions but is also sensitive to those of copper. The targets utilized in this experimental configuration were comprised of copper only in the midplane region, such that the emitted K-photon radiation would correspond overwhelmingly to reconnection-induced electron currents. Targets were irradiated with focal spot separations of 500 μm and 750 μm, and reference data was collected by irradiating the target with either beam firing alone. Figure 4.24 summarizes the calculated spectra in absolute units.

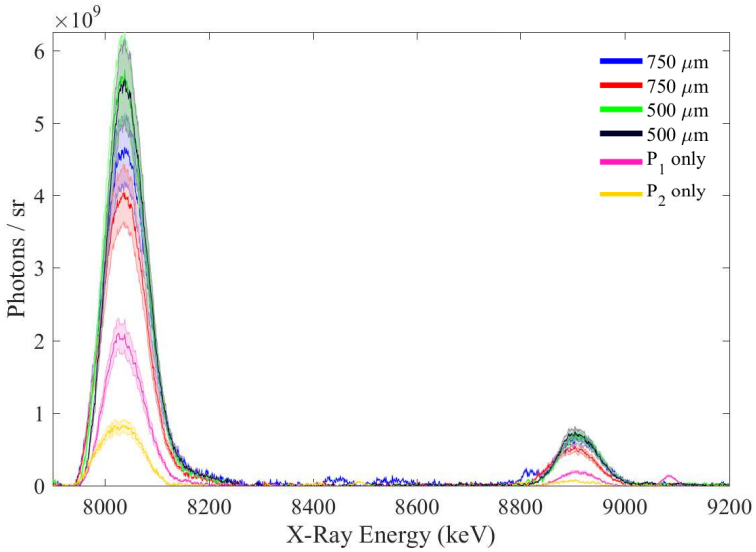

Figure 4.24: Summary of the Zinc Von Hamos (ZVH) data acquired from Omega EP with Experimental Configuration 2. Two reference shots P_1 and P_2 correspond to BL 1 and BL 2, respectively, at 500 μm separation.

Firing Pulse 1 and Pulse 2 alone yielded measurable Cu K_α and K_β X-rays, with P_1 yielding 2.4±0.24 as many as P_2 (partially accounted for by a $\sin^2\theta$ dependency of relative absorption). Therefore these signals are representative of the background signal expected

from electron propagation directly from the focal spots. For the case of 500 μm separation, the simultaneous firing of both P_1 and P_2 resulted in 2±0.2 times more photons compared to the sum of the signals induced by the individual pulses. For a larger spot separation of 750 μm, the integrated K_α drops by 21±2% compared to 500 μm.

As was outlined in Section 2.4.3, it is possible to estimate from the ratio of K_β to K_α photons the temperature of the electron plasma in the region from which the photons originate. These ratios and the corresponding estimated electron plasma temperatures are plotted in Figure 4.25.

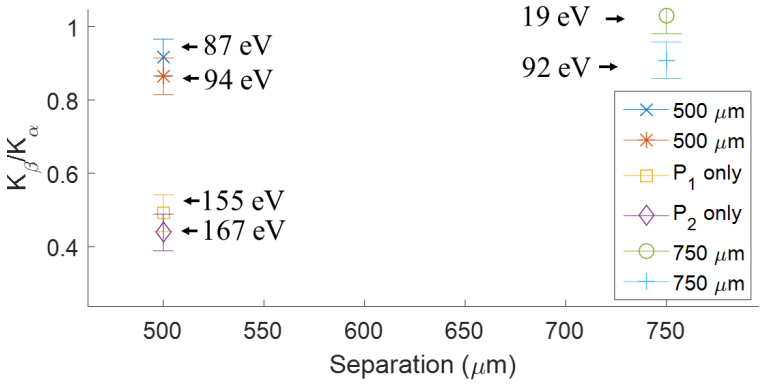

Figure 4.25: K_β/K_α ratios extracted from the Zinc Von Hamos (ZVH) spectra acquired from Omega EP with Experimental Configuration 2. Two reference shots P_1 and P_2 correspond to BL 1 and BL 2, respectively, at 500 μm separation. The corresponding estimates for electron plasma temperatures are labeled.

As can be seen from Figure 4.25, the single-pulse shots resulted in K-photon emissions from a hotter electron plasma compared to the dual-beam shots. This is suggestive that in the former case, the plasma from which the K-photons originate is primarily formed near the surface of the embedded copper bar, where the plasma may be hottest. When both beams are fired, the K-photons originate from a colder, and thus likely deeper, volume of the plasma. This is consistent with the attribution of the K-photon signal to electrons accelerated into the target by the reconnection electric field.

Because the K-photons measured for the simultaneous pulse condition contain a contribution from the same signal resulting in the single-pulse K-photons, the calculated temperatures in the former case are over-estimated. For the 500 μm separation case, the summed K-photon signals for two the single-pulse shots are subtracted from the simultaneous pulse shot sig-

nal, resulting in a K_β/K_α ratio of 0.142±0.02, corresponding to an electron temperature of approximately $T_e = 0$.

4.7.4 Single Photon Counter

An X-ray CCD operated in single-photon-counting mode was utilized on Omega EP during Experimental Campaign 1. The instrument served to measure the radiation spectrum up to $\sim$ 40 keV, providing signatures of material contaminants and estimates of the relative K-photon yield. Figure 4.26 summarizes the results from the separation scan.

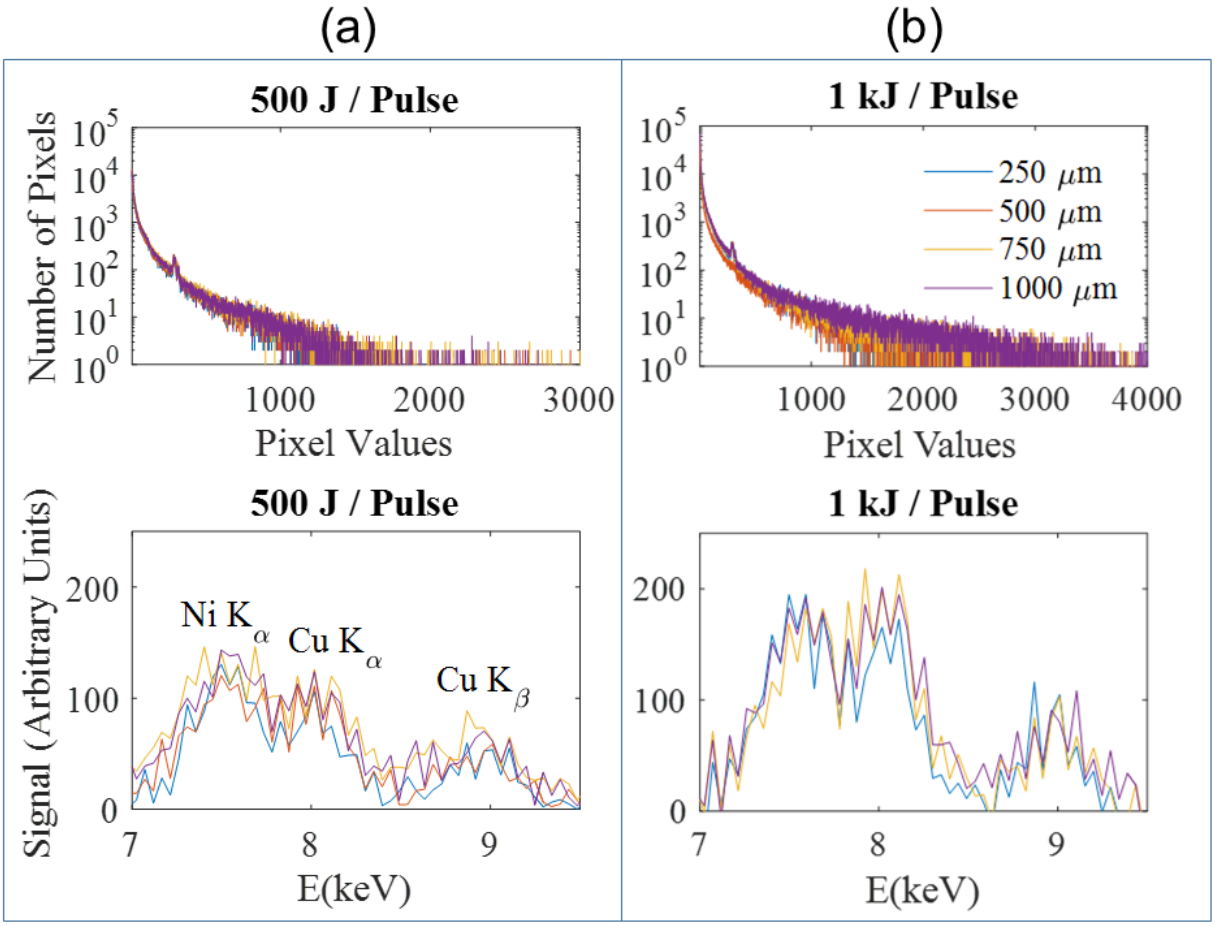

Figure 4.26: The results from the single photon counter utilized on Omega EP during Experimental Configuration 1 for the 500 J/pulse case (a) and 1 kJ/pulse case (b). The top two rows show the binned data over the entire spectrum, while the bottom two rows show the K-photons of copper and nickel with broadband X-rays subtracted and with calibrated energy axes.

In addition to the copper K_α and K_β, the nickel K_α is also present due to the material not being comprised of pure copper but rather being an alloy with trace amounts of nickel. Figure 4.26 demonstrate the effects of a hotter electron temperature with the 1 kJ/pulse case, while the K_α images suggest similar reconnection conditions. This could reflect

The similar reconnection results at higher beam energy despite the higher electron temperature on Omega EP can be explained by the following: 1) the length L of the reconnection region is determined by the global characteristic length scale, which is expected to be insensitive to beam energy, 2) the width δ of the reconnection region is expected to increase for faster reconnection rates, which was observed to generally coincide with higher beam energy, and 3) the integrated midplane emission was potentially saturated such that increased beam energy led to a small increase in K_α flux, or alternatively the higher magnitude reconnection electric field accelerated electrons to energies that led to a lower K_α emission cross section.

4.8 Simulations

The particle-in-cell (PIC) code OSIRIS was utilized to run a fully relativistic, fully 3-dimensional simulation of a dual-beam laser/plasma interaction to demonstrate magnetic reconnection. This was performed on NASA's Pleiades Supercomputer.

The parameters for the simulation are outlined in Appendix A. While the details of the accelerated electron spectra and temporal duration of the reconnection are provided in Chapter 5 and Chapter 6, respectively, this Section focuses on the demonstration of magnetic reconnection and the dimensional features of the current sheet.

A fully relativistic, three-dimensional simulation of the reconnection geometry most closely resembling the Hercules short-pulse scenario was conducted using the PIC code OSIRIS [116]. The laser pulse had a 40 fs full-width-at-half-maximum pulse duration and focused intensity of 2×10^{19} Wcm^{-2}. The pulse was normally incident upon an electron plasma with $n_{max} = 30 n_{crit}$ (where $n_{crit} = \frac{\epsilon_0 m_e}{e^2}\omega_0^2$ is the critical plasma density) and pre-plasma scale length $l = \lambda = 810$ nm, and with stationary ions. Periodic boundaries in the transverse x_2 directions were used to result in an effective spot-to-spot separation of 388 c/ω_0 (50 μm).

An isotropic, quasi-Maxwellian population of electrons with ∼1 MeV temperature was seen to be generated from the interaction site(s) after irradiation, followed by confinement of the fast electrons along the plasma surface. The maximum azimuthal B-field magnitude within the interaction site is 35 MG. The counter-streaming surface electrons and their associated azimuthal magnetic fields reach the midplane within 2 pulse durations, when rapid reconnection of the magnetic field lines within a region of $\delta \times L = 50 \times 200(c/\omega_0)^2$ was observed (a dimensional ratio comparable to the experimental measurements).

As anti-parallel magnetic field lines converged and began to reconnect, an out-of-plane electric field with $E_{peak}/cB_{R0} \approx 0.3$ formed (Figure 4.27), where $B_{R0} \approx 2$ MG is the azimuthal magnetic field magnitude in the vicinity of the reconnection layer.

The charge-separation target normal electric field was estimated by calculating $\frac{1}{2}(E_{max} + E_{min}$ within the reconnection region and subtracted this value to determine the reconnection electric field. This estimation was shown to agree within 10% of the reconnection field calculated by the following procedure: the charge-imbalance field along x_2 was constructed by taking a line-out along x_3 across the focal spot region; this was shifted by the focal spot separation and added to itself, then subtracted from the corresponding line-out along x_2.

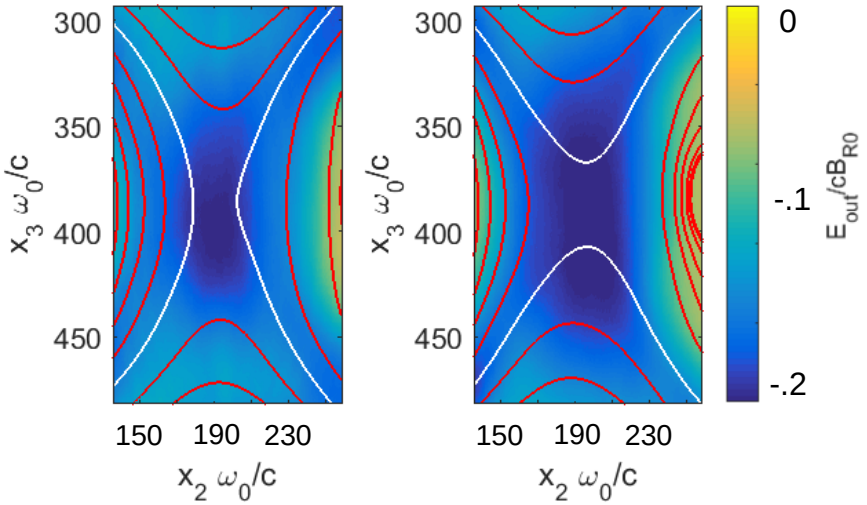

Figure 4.27: The mid-plane, target-normal reconnection electric field at $t/\tau_p = 5.6$ (left) and $t/\tau_p = 5.9$ (right), with magnetic field lines overlaid. The white magnetic field streamline is seen to demonstrate a topology change, while the electric field grows. The electric field is normalized to cB_{R0}, where B_{R0} is the local magnitude of the azimuthal magnetic field.

Three-dimensional streamlines of the magnetic field were plotted (Figure 4.28) to demonstrate the magnetic field topology; in this Figure, an iso-surface of the target-normal electric field (with value $|E_1|/cB_{R0} = 0.133$) is also shown, as well as slices of $E_1 \cdot J_1$ evaluated at center slices through the depicted simulation box.

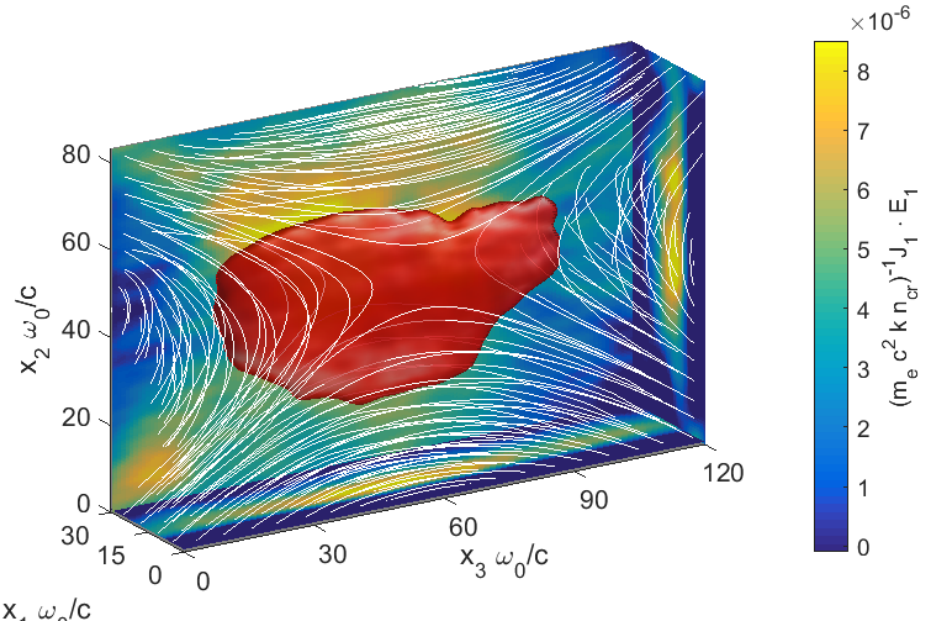

Figure 4.28: A 3-D graphic of magnetic field streamlines (white), the associated reconnection electric field (displayed as an iso-surface with magnitude $|E_1|/cB_{R0} = 0.133$), and the value of $E_1 \cdot J_1$ evaluated in center cuts through the displayed volume (box faces). The interaction sites are located 194 c/ω_0 away along x_2, and x_1 is in the target-normal direction.

Temporally averaged over two pulse durations (beginning at $t = 3\tau_p$), the value of $E_1 \cdot J_1$ (with magnetic field streamlines superimposed) is demonstrated in Figure 4.29.

Further analysis of the magnetic fields revealed pairs of newly reconnected flux tubes (cylindrical regions of space containing a magnetic field, such that the field at the side surfaces is parallel to those surfaces). Additionally, a quadrupole pattern in the out-of-plane magnetic field was observed (Figure 4.30), indicating that the Hall term of the generalized Ohm's law may be significantly contributing to the reconnection electric field [120].

Electrons are accelerated into the target within a localized region centered at the mid-plane, developing a nonthermal spectral component in addition to a Maxwellian low-energy portion. The nonthermal component may be fitted by a power law $f(\gamma) \sim \gamma^{-1.58}$ (this is shown and discussed in Section 6.6). A localized current sheet with dimensions comparable

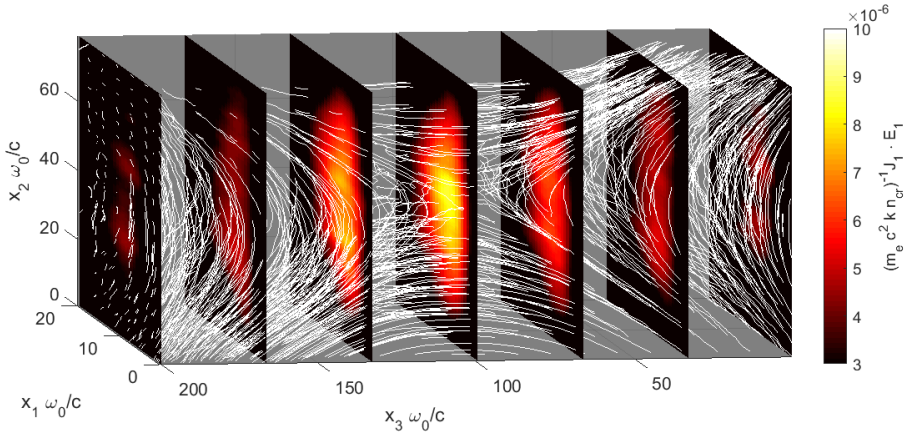

Figure 4.29: The value of $E_1 \cdot J_1$, quantifying the work done on the electrons by the field, in the midplane region. Also plotted are 3-D magnetic field streamlines initialized at the box faces.

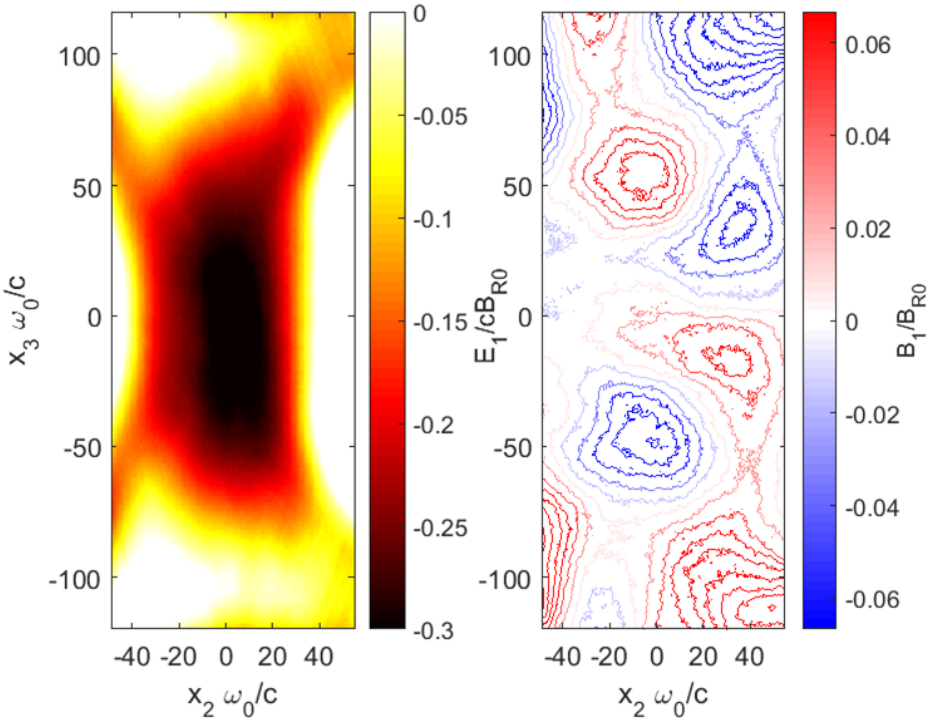

Figure 4.30: (a) The target-normal electric field with the capacitive sheath field subtracted, and normalized to cB_{R0}. (b) The magnetic field in the target-normal direction within the same region normalized to B_{R0}, demonstrating the quadrupole magntic field pattern indicative of Hall-like reconnection.

to the midplane reconnection electric field is observed, with an aspect ratio of $\delta/\text{Ł} \approx 0.3$ at $t = 5.5\tau_p$ which reduces to $\delta/\text{Ł} \approx 0.25$ at $t = 6.0\tau_p$.

Due to the relatively stationary ions over the course of the interaction, the electron magnetohydrodynamics (EMHD) applies and the reconnection rate may be written with respect to the electron current sheet aspect ratio $\delta/L = E/cB \approx 0.3$.

The development of the electron spectral characteristics indicating magnetic reconnection is disclosed in Section 5.5.

The results from the PIC simulation therefore supports the reconnection interpretation of the experimental results. While the laser pulse durations utilized on Omega EP and Titan were much longer than that of the simulation pulse, the same experiments may in the same regime of reconnection as defined by the relativistic focused intensity and corresponding relativistic inflows.

Further, calculations of the parameter $\sigma \equiv B^2/(\mu_0 n_e m_e c^2)$ were performed, resulting in values $\sigma = O(1)$ in the upstream region, indicating that the energy available per electron from the magnetic field is comparable to the electron rest mass energy. In the target-surface region, a significant percentage ($> 40\%$) of the σ values above a threshold $\sigma > 0.001$ exceed the value $\sigma = 1$. Therefore, the regime can be described as that of *relativistic* reconnection. The region of appreciable σ values was localized near the target surface, as Figure 4.31 (a) demonstrates below. Figure 4.31 (b) depicts the radial dependence of σ. At this same time-step, Figure 4.32 provides a histogram of non-zero σ values on the target surface.

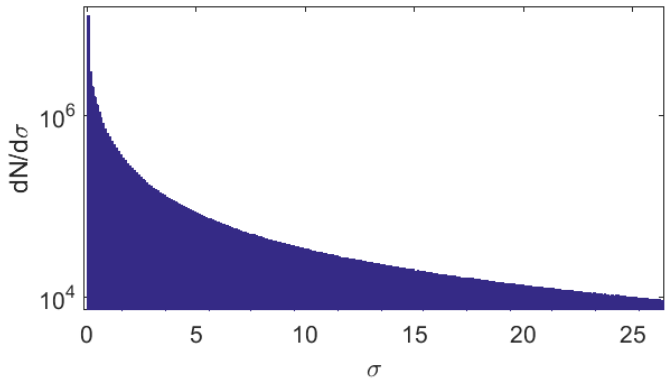

Figure 4.32: The distribution of σ values immediately before the two plasmas interact, excluding values $\sigma < 0.001$ which result from regions outside the region of interest.

No magnetic islands (i.e., *plasmoids* [35]) were observed in the simulation. These are quasi-spherical magnetic islands which spontaneously form along the reconnection X-line,

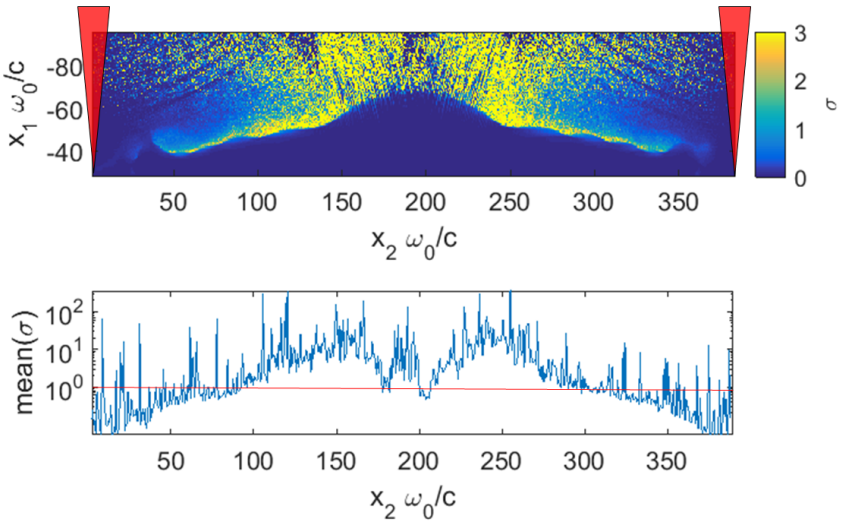

Figure 4.31: (Top) A cut-out showing a colormap of σ varying from the focal spot region (left and right boundaries) to the reconnection region (centered). The red triangles represent the horizontal focal spot location(s). (Bottom) An averaged line-out showing the variation of the mean value of σ with respect to the distance from the focal spot region, excluding values $\sigma < 0.001$. The horizontal red line indicates an average value of $\sigma = 1$.

wherein relativistic particle acceleration and magnetic energy are concentrated. Such features have been seen to form readily in 2-D and 3-D PIC simulations of magnetic reconnection in the non-relativistic and relativistic regimes [121], within the context of electron/positron plasmas. In 3D, the drift-kink instability has been seen to corrugate the reconnection layer early in time, while the plasmoid instability dominates the long term evolution and facilitates efficient particle acceleration [122]. Their absence is potentially accounted for by short length of the current sheet, to which the frequency of their generation has been seen to be linked [36]. Given that plasmoids are localized regions of very efficient particle acceleration, it is conceivable that the electrons accelerated by the reconnection electric field generated during the Omega EP experiments would be of much higher energy than predicted in our simulation.

Further, an approximation of the relative efficiency of magnetic energy to particle energy in the midplane can be obtained from the ratio of the time-rate of work performed on electrons by the reconnection electric field, $\mathbf{E} \cdot \mathbf{J} \sim 10^{-5}$, to the time rate of magnetic energy density entering the region, $\frac{\partial}{\partial t} \frac{B^2}{2\mu_0} \sim 10^{-}3$. This yields a relative peak efficiency on the order of a few percent.

4.9 Conclusions

The copper K_α images provided dimensional characteristics of the reconnection region by which the results from each facility may be compared. The comparison is in regard to the spatial extent of the current sheet, as revealed by the localized enhancement of K_α emission. The aspect ratio of the diffusion region was found to range from $\approx 0.2 - 0.45$ depending on the laser intensity and focal spot separation.

If the length L of the diffusion region is linearly related to the radius of curvature of the azimuthal magnetic field lines, this can potentially explain the surprising continuation of the linear trend to the Titan data, wherein the beam energies were imbalanced and the diffusion region was offset. In the location where the diffusion region forms, the the length L can potentially be identified as the average of the curvature radii from either interaction site. This averaged radius would be approximately equal to that experienced in the midplane if both beams were of equal energy, explaining the continued linearity.

The observation and characterization of the extended regions of K_α enhancement is consistent with magnetic reconnection. Back-side K_α measurements were compared to those collected from the target-front, revealing that the K_α X-rays were predominantly generated several microns into the target from the target's front surface.

X-ray pinhole cameras utilized during the Omega EP focal separation scan yielded spatially resolved, temporally and spectroscopically integrated images of the interaction for X-rays of energies $\sim 2 - 6$ keV. No broadband emission was observed between the two interaction sites, indicating that the observed K_α emission was not due to collisional heating between two plasmas but rather consistent with high-energy electrons propagating into the target within a localized region. This regime is also distinct from the nanosecond pulse regime where target heating due to reconnection is observed by pinhole cameras [123].

A highly ordered pyrolytic graphic (HOPG) crystal in the Von Hamos configuration was utilized to measure spectra for photons in the zinc and copper $K_{\alpha,\beta}$ range, at Omega EP with Experimental Configuration 2. From the ratio of copper K_β to copper K_α photons, it was determined that the midplane K_α radiation emanated from a relatively cold electron plasma (20-94 eV compared to 155-167 eV for single-pulse shots). This is consistent with

hot electrons generated during reconnection propagating into the midplane and depositing their energy via collisional ionization in the denser, colder plasma.

Finally, a fully relativistic 3-D PIC simulation most closely resembling the HERCULES laser conditions revealed clear signatures of magnetic reconnection in the relativistic regime. Oppositely oriented magnetic field lines were seen to reconnect within the midplane, wherein a strong target-normal electric field was generated, accelerating electrons into the target with a hard power law spectrum of $p = 1.6$ and with non-thermal energies. The reconnection was observed to occur at a peak rate of $E/cB \approx 0.3$.

To the knowledge of the author, these are the first reports of laboratory magnetic reconnection observed in a regime characterized by relativistic inflows. Simulation results indicate that the interactions likely occur within the relativistic regime, in which the energy density of the reconnecting magnetic field exceeds the rest mass energy density of the plasma.

The use of two relativistically intense laser pulses may thus be a test-bed for conducting reconnection experiments relevant to high-energy astrophysical processes. Access to regimes of even higher magnetic fields and correspondingly more magnetized plasma conditions may be made available by next-generation Petawatt laser facilities such as ELI [124], leading to a method to characterize the reconnection in relativistic electron-positron plasmas in the laboratory.

Chapter 5

Temporal Measurements of Reconnection

5.1 Introduction

A topic of significance for magnetic reconnection research is the *rate* of reconnection, typically expressed as the ratio of the reconnection electric field and the magnitude of the reconnecting magnetic field lines, normalized to the Alfven velocity: $E/v_A B$. The reconnection rate is defined as the rate at which flux conservation is violated in the reconnection process, and determines the time required for the available magnetic potential energy to dissipate via reconnection. Estimates for reconnection rates notoriously over-estimated reconnection times, for example predicting that the reconnection events which lead to the generation of solar flares would occur over the span of years (instead of days) [125].

Within the Sweet-Parker model, the ratio of the current sheet width to length $\delta/L = v_{in}/v_A = S^{-1/2}$, where S is the Lundquist number, equal to the ratio of the global Ohmic diffusion time to the global Alfven time. Since most astrophysical systems have large values of S, the predicted reconnection rate (embodied by v_{in}) is very slow. Since the current density must be large enough to dissipate the incoming magnetic energy, the current sheet must be very thin; but since this width is equal to the width of the outflow, the mass flux leaving the current diffusion region will be very low [26].

Hall reconnection proceeds much faster than Sweet Parker reconnection. One study of two-dimensional Hall magnetohydrodynamic simulations found that the Hall reconnection rate assumes a maximum value $\partial\phi/\partial t \sim 0.1 V_{A0} B_0$ where ϕ is the reconnected flux, and

V_{A0} and B_0 are the velocity and magnetic field strength in the upstream region. The rate was found to be only weakly dependent on the initial current sheet width, and completely independent of scale length of the plasma and of the system size [126].

In the case of relativistic laser/plasma interactions, the expected inflow (and outflow) speed is $v \sim c$. The Alfven velocity then takes the form $v_A = c\sqrt{\sigma/(1+\sigma)}$ where $\sigma \equiv B^2/(\mu_0 n_e m_e c^2)$ is the magnetization parameter of the plasma. Evidence for reconnection occuring within this regime was presented in the previous Chapter. Here, measurements are presented which addressed the time over which reconnection occurs in the regime explored.

Results will be presented from Omega EP (Experimental Configuration 2, depicted in Figure 4.5), in which the temporal duration of midplane K_α emission was measured. Additionally, results from the Titan facility are presented in which the same emission was attempted to be measured. Results will be compared to the 3-D PIC simulation introduced in the previous Chapter.

5.2 Experimental setup: Omega EP

The longer pulse duration of 20 ps while maintaining the a similar relativistic focused intensity allowed high-resolution time-dependent measurements of the interaction at Omega EP.

The target design (introduced in Figure 4.7) is that of an aluminum frame with an embedded copper bar in the midplane region. The copper bar was located such that the anticipated reconnection region (as deduced from time-integrated K_α images) was centered upon the embedded copper bar. The geometry of the target along with an image is displayed in Figure 5.1.

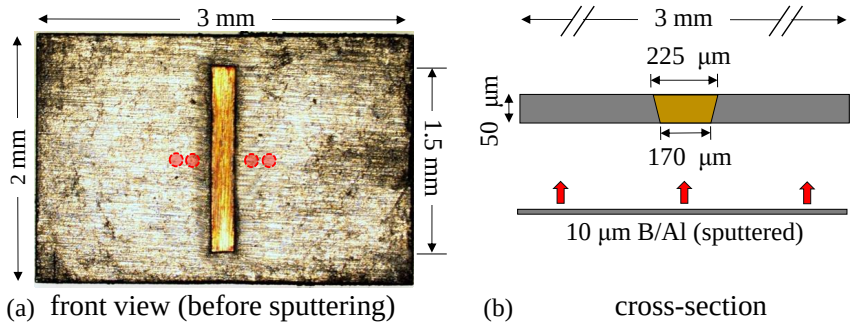

Figure 5.1: The targets used on Omega EP to determine the temporal duration of the K_α emission from copper. a) A front-view image of the target (before sputtering); the red circles indicate the focal spot positions corresponding to a 500 μm separation and 750 μm separation. While the circles are shown with a large diameter as a visual aid, the average radius within which 80% of the laser energy is contained was 18 μm. b) The target's cross section, demonstrating the boron/aluminum layer sputtered over the target's front side.

To ensure that the radially expanding surface electrons were not impeded by resistive magnetic fields generated by steep resistivity gradients between target materials [127], a 10 μm layer of boron/aluminum was sputtered onto the front surface of the target (upon which the lasers are incident). The spherically bent X-ray crystal imaged the copper bar onto the slit of a picosecond streak camera (3000 Å CsI photocathode and 600 ps sweep speed) with 6× magnification. The chamber configuration was presented in Figure 4.5, and an additional qualitative schematic is displayed below in Figure 5.2.

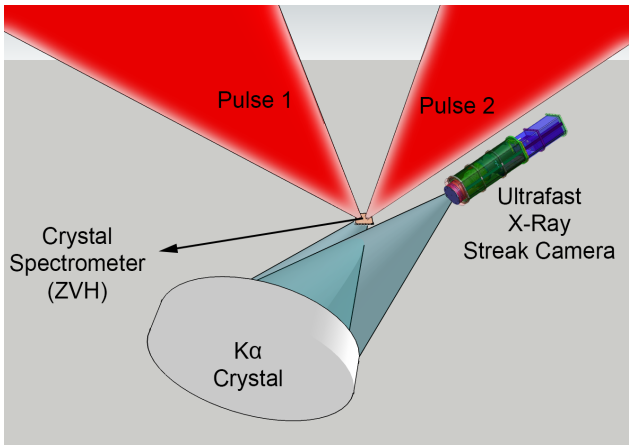

Figure 5.2: A simplified schematic indicating the incoming short-pulse laser pulses, stalk-mounted target, spherical X-ray crystal, crystal spectrometer, and ultrafast X-ray streak camera. The K_α crystal and ZVH view the target's front surface.

While Chapter 4 discussed this chamber and target geometry in regard to time-integrated X-ray measurements, this Chapter focuses on the temporal resolution of the emitted K_α signal.

5.3 Experimental setup: Titan

On Titan, the X-ray framing camera DIXI2 (see Section 3.3.4) was utilized to attempt to record time resolved X-ray midplane emissions from irradiated copper targets. The Titan chamber schematic is reproduced in Figure 5.3:

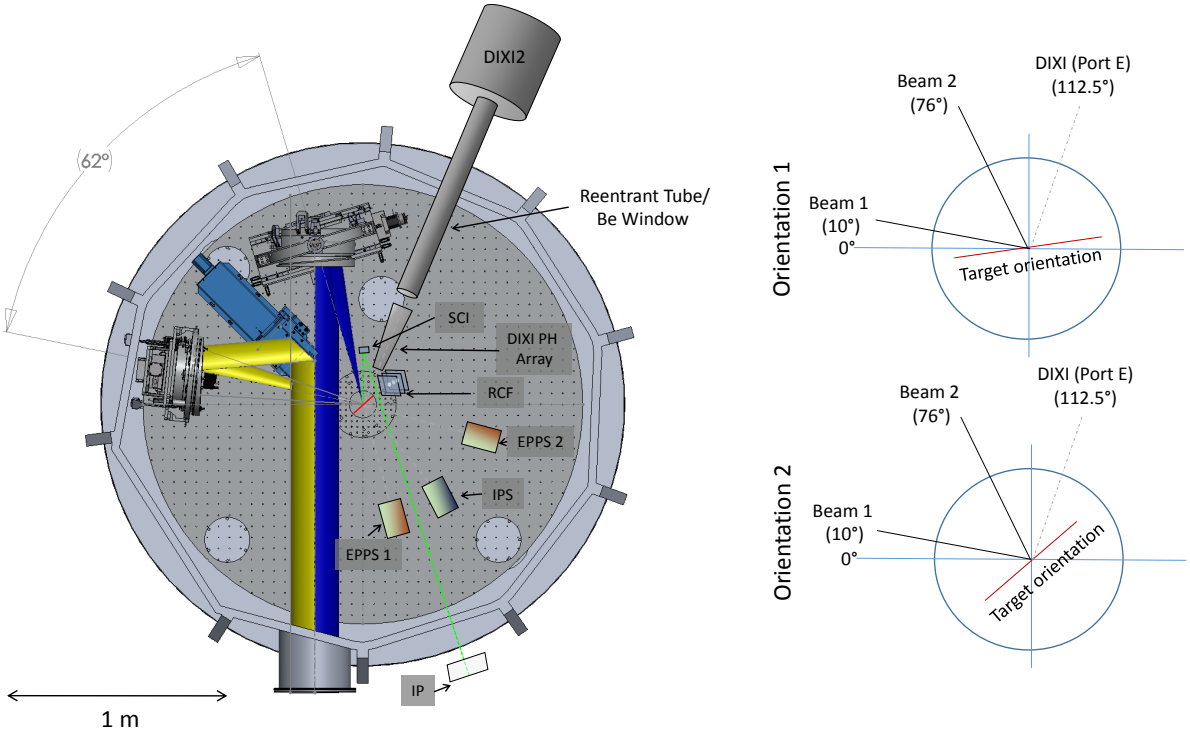

Figure 5.3: The TITAN chamber with the location of the X-ray framing camera DIXI visible. The diagrams to the right depict the two target orientations utilized during the experiments.

DIXI2 utilized a pinhole array comprised of 38, 1-mm equilateral triangles, resulting in digitally recorded images with a spatial scale of 22.47um/pixel and temporal scale of 279 μm/picosecond. The time between frames was approximately 50 ps. The pinhole geometry (with the resulting temporal scale) is depicted in Figure 5.4.

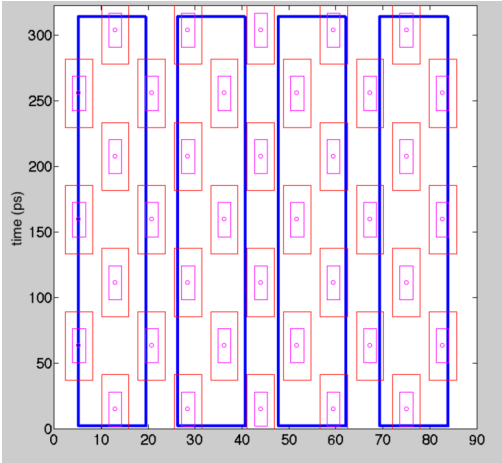

Figure 5.4: The pinhole configuration utilized for DIXI2. The positions of the red rectangles indicate the location of the triangular pinholes (*i.e.*, frames), with the vertical axis indicating the corresponding time between frames. The horizontal scale indicates the spatial extent of the pinholes, in units of millimeters.

The pinhole array was positioned ≈ 90 mm from target chamber center (TCC), resulting in an expected magnification of $\times 14$. The device could be used in time-integrated mode (in which case it behaved as a typical pinhole array) or active mode.

Targets comprised of 25 μm copper and 25 μm titanium were irradiated, with the mid-plane feature within the field of view of DIXI2.

The Titan laser was used with pulse durations of both 0.7 ps and 10 ps, with corresponding nominal energies of 140 J and 240 J, respectively. The energy was split into two pulses, resulting in nominal focused intensities of 6×10^{19} Wcm^{-2} and 7×10^{18} Wcm^{-2}, with a 15 μm FWHM focal spot size.

5.4 Results

Accurate co-timing of the two Omega EP pulses were ensured by performing a calibration shot with a 100 ps delay between the pulses onto a solid copper foil and checking the temporal separation using the UFXRSC.

Following this, the specialized targets were irradiated with 1 kJ/pulse at focal spot separations of 500 μm and 750 μm. Finally, BL 1 and BL 2 were alternatingly fired alone, at focal positions corresponding to the 500 μm separation.

A summary of the raw UFXRSC data is presented in Figure 5.5.

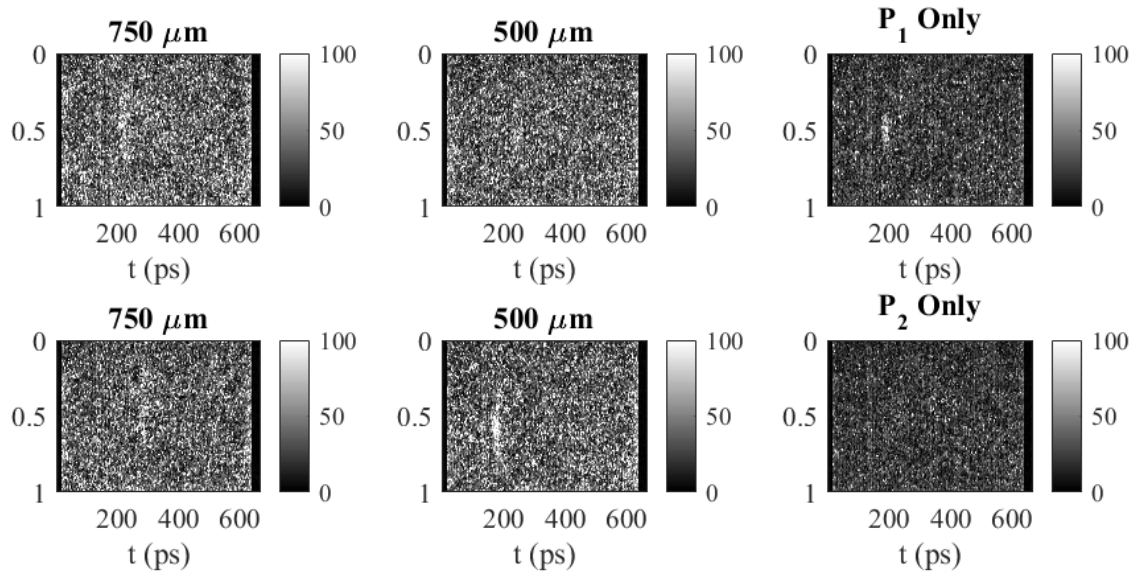

Figure 5.5: The digital images for the UFXRSC scan on Omega EP, in arbitrary digital units.

From Figure 5.5, it can be seen that the signal-to-noise level was relatively low. Despite this, the data was extracted by performing 3-pass smoothed lineouts. The resulting lineouts are displayed in Figure 5.6, with the temporal scale arbitrarily initialized.

For those shots which resulted in appreciable signal, the FWHM temporal duration and relative intensity are compared in Figure 5.7.

As can be seen from Figure 5.7, the two-beam shot corresponding to a shorter focal separation yielded approximately double the integrated K_α than the farther separation, and exceeded the combined integrated signal of the single-pulse shots at the same small separation. The longer emission duration for the 500 μm separation compared to 750 μm may be due to the larger amount of magnetic energy to be converted, resulting in a longer reconnection time and thus a correspondingly longer K_α emission duration.

The onset of the K_α emission occured within $\approx 100 - 200$ ps of the laser arrival time, with more accurate determinations being impossible due to the inconsistent triggering time of the UFXRSC by inherent jitter.

The duration of the K_α emission may be related to that of the burst of relativistic

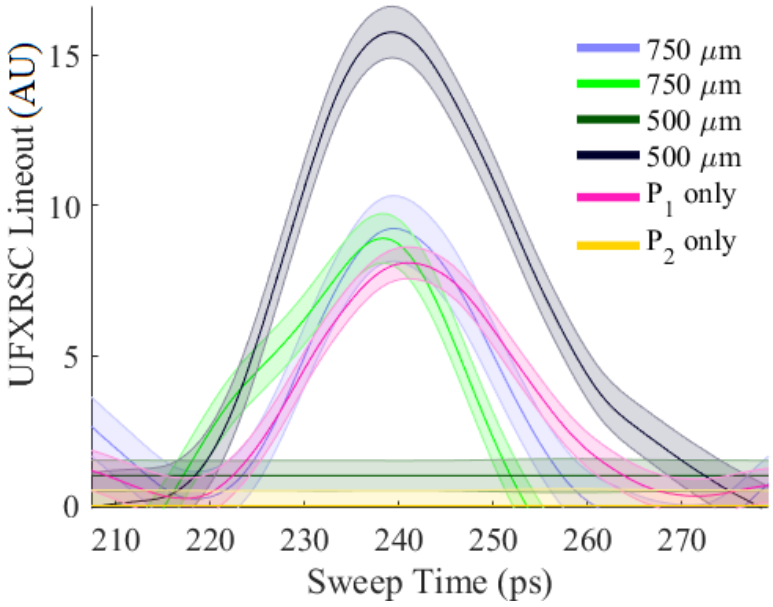

Figure 5.6: 3-pass smoothed lineouts of the UFXRSC data collected on Omega EP. The single-pulse (P_1 and P_2) shots were taken at positions corresponding to 500 μm focal separation.

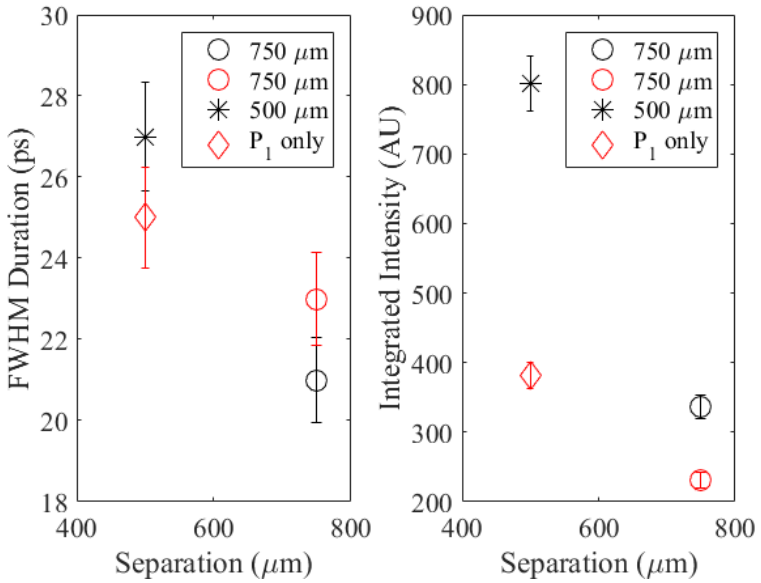

Figure 5.7: (a) The FWHM temporal duration of the K_α emission corresponding to the shots which resulted in appreciable signal. (b) The relative intensity of the integrated signal.

electrons from the interaction site. On Omega EP, a pure 50 μm-thick copper target was irradiated with two pulses of duration 20 ps, pulse energy of 500 J/pulse, a focal spot

separation of 750 μm, and a temporal separation of 100 ps. The resulting trace collected in the same manner as the shots described above is presented below in Figure 5.8.

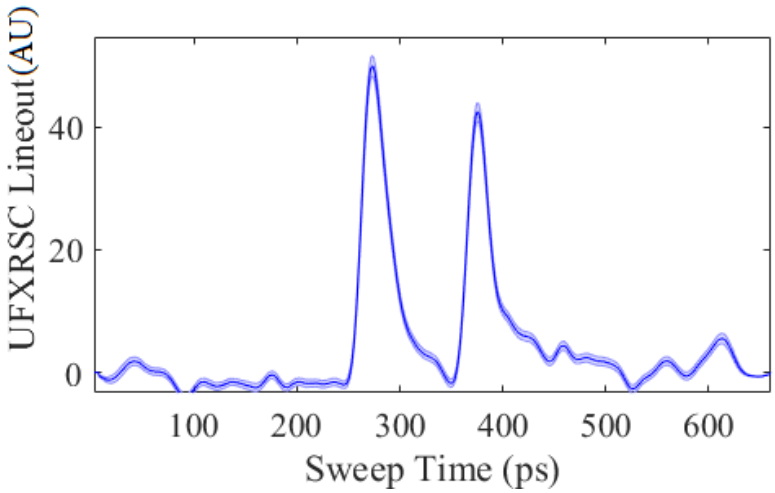

Figure 5.8: The UFXRSC trace collected at Omega EP for a reference two-beam shot taken onto a 50 μm-thick copper target with a pulse duration of 20 ps, pulse energy of 500 J/pulse, a focal spot separation of 750 μm, and a temporal separation of 100 ps. The two peaks provide the duration of K_α emission resulting from the irradiation of either beam onto the bulk copper target, separated in time to observe their entire traces.

From these traces, the FWHM pulse durations are measured to be 28 ps and 24 ps.

On the Titan laser, the DIXI2 framing camera easily resolved the X-ray signal originating from the laser interaction points, resulting in broadband emission durations $>$ 300 ps for both the 0.7 ps pulse case and the 10 ps pulse case. During the majority of the shots, the MCP gain was intentionally saturated for the focal spot site emissions, to aid in detecting midplane emission since the dynamic range is limited. Due to this, a temporal profile for the interaction site emission could not be constructed.

Midplane emission was only detectable in time-integrated mode for a total of 3 shots out of 41, indicating a lack of significant broadband signal emanating from the midplane (consistent with the Omega EP XRPHC data shown in Section 4.7.1) and displaying the difficulty of detecting time-resolved measurements. Despite the low occurrence of measurable midplane signal with the DIXI2 diagnostic, the midplane feature was consistently apparent when measured with the spherically bent X-ray crystal (section 4.7.1).

There existed 4 candidates for time resolved DIXI2 measurements, all of which were recorded with the short pulse (0.7 ps). In all cases the signal was detected for the first

frame of a given strip of time-resolved pinhole images, and was not apparent in the following frame. The average signal-to-noise ratio of the midplane emission was 1.15. One such result is presented in Figure 5.9 (a), along with (b) a comparison of the magnified emission to a simultaneously collected K_α image. It is shown that the midplane emission detected with DIXI2 was offset by the same distance observed with the K_α imager. The energy imbalance during this shot was $U_2/U_1 \approx 0.8$.

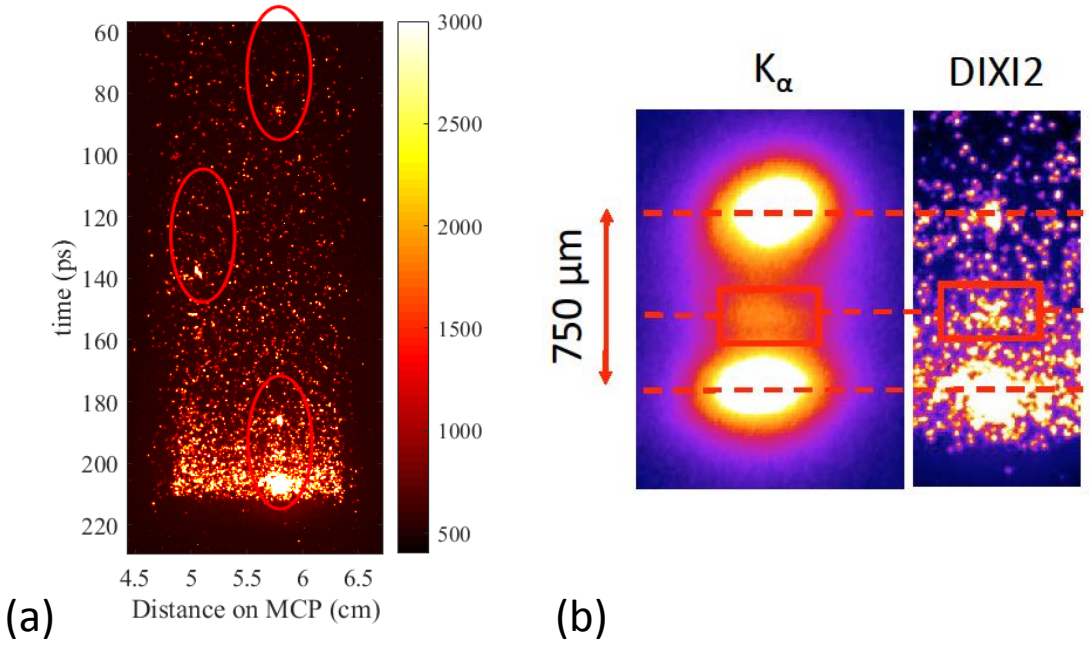

Figure 5.9: (a) A strip from the X-ray framing camera DIXI2, with laser pulse duration 0.7 ps and focal separation 750 μm; emission is detected between the two X-ray sources associated with the laser interaction sites, which disappears within 50 ps of the frame. (b) A simultaneously measured K_α image of the interaction shows the midplane emission offset observed with DIXI2 is as expected.

While a complete reconstruction of the midplane emission duration was not accomplished, the data suggests that it is significantly less than the emission from the interaction sites.

While these features were observed with copper targets, no such features were found when shooting titanium targets despite DIXI2's superior quantum efficiency at the titanium K_α compared to that of copper. Midplane features were not observed with titanium targets even when DIXI2 operated in time-integrated mode. However, due to the low occurrence

rate of midplane emission measurements with copper targets, the lack of titanium target midplane measurements may not be significant.

5.5 Simulations

As previously described in Section 4.8, a 3-D, fully relativistic particle-in-cell (PIC) simulation was performed to study magnetic reconnection in the regime characterized by relativistic inflows. While the simulation parameters (see Appendix A) are most relevant to the HERCULES laser conditions, the power per pulse is similar among the various laser pulses utilized for the experiments, and all pulses are focused to relativistic intensities. Further, the trends discussed in Chapter 4 suggest that the reconnection dynamics may be occuring in a similar regime, indicating that the simulation is potentially relevant to all experimental conditions explored in this thesis.

To analyze the temporal dynamics (as is the subject of this Chapter) from the simulation interaction, various quantities are tracked within the reconnection region (a 3-D subset of the simulation box which encompasses the midplane region, with dimensions $\Delta x_1 = 100c/\omega_0, \Delta x_2 = 50c/\omega_0, \Delta x_3 = 250c/\omega_0$).

To calculate the electron spectra over time, attention is focused to those electrons which possess a momentum direction into the plasma within the midplane region (and would subsequently result in strong K_α emission). The $p_1 - x_2$ phase space outputs were integrated over x_2 values corresponding to the reconnection region boundary with a width $\Delta x_2 = 50c/\omega_0$. The distribition $dN/d\gamma = (dp/d\gamma)dN/dp$ was then calculated, the resulting plots form which are shown in Figure 5.10.

The spectra evolve to assume a hard power law component $dN/d\gamma \propto \gamma^{-1.58}$. Based on prior simulation studies [128], this value is consistent with a value $\sigma \equiv B^2/(\mu_0 n_e m_e c^2) \gtrsim 1$, supporting the determination that the reconnection event occurs in the relativistic regime.

The reconnection electric field is calculated by subtracting the capacitive sheath electric field which forms due to the charge imbalance as electrons are accelerated away from the plasma. The resulting maximum electric field values for the total and sheath-removed fields are displayed in Figure 5.11.

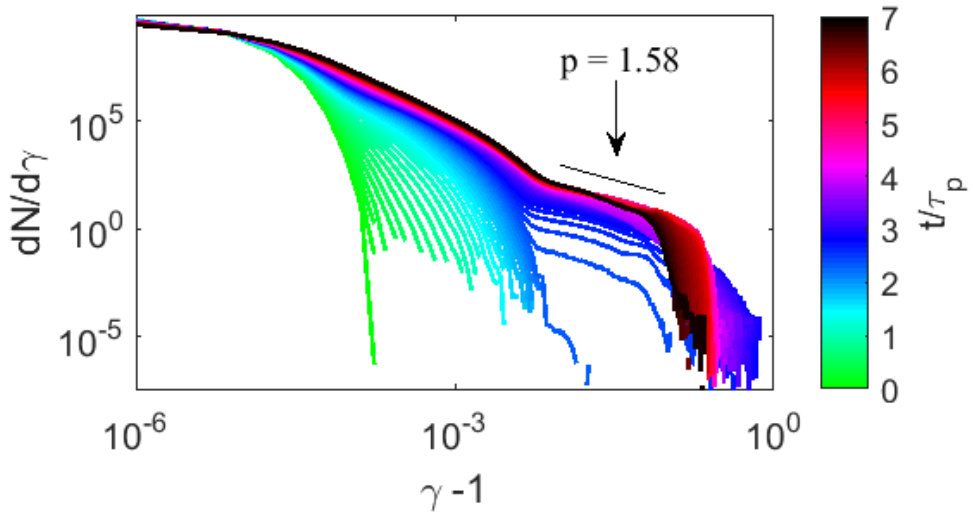

Figure 5.10: The energy spectra over time for electrons traveling into the plasma within the reconnection region.

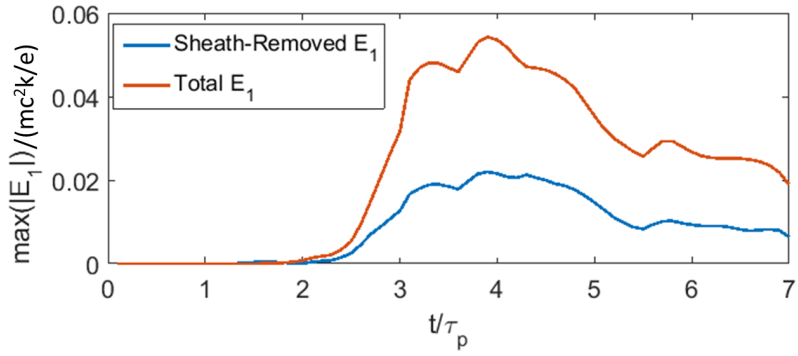

Figure 5.11: Temporal traces of the maximum total electric field magnitude and sheath-removed field magnitude evaluated within the reconnection region.

From Figure 5.11 it can be seen that an effective duration of the reconnection field lifetime is approximately equal to 2 pulse durations, and that the reconnection field magnitude is equal to approximately 1/3 that of the total electric field.

Next, it is desirable to analyze how the temporal dynamics of the magnetic potential energy in the reconnection region relates to the nonthermal electron generation. Figure 5.12 demonstrates normalized quantities of the total magnetic energy density in the reconnection region $U_b \propto B_1^2 + B_2^2 + B_3^2$ and the energy in the nonthermal portion of the electron spectrum, calculated from the phase space. Each quantity is normalized to its maximum value.

Figure 5.12 demonstrates that the nonthermal electrons gain energy as the magnetic

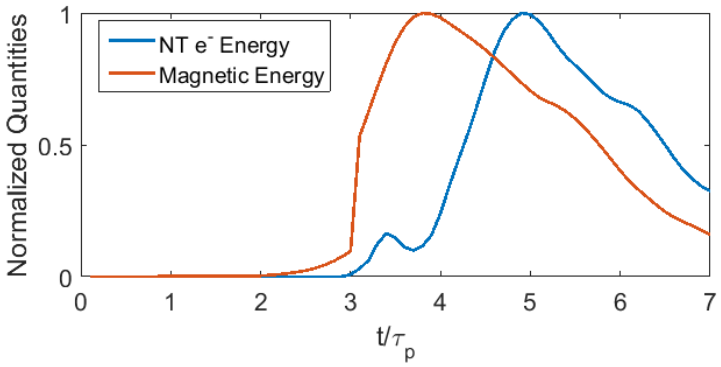

Figure 5.12: Temporal traces of the magnetic energy density in the reconnection region, and the energy in the nonthermal portion of the electron spectrum. Each variable is normalized to its own maximum value.

energy density decreases, indicating that the magnetic energy density is being transferred to the population of electrons, via the generation of the reconnection electric field.

These temporal traces also yield the ~ 2 pulse duration time over which magnetic energy is transferred to particle kinetic energy.

5.6 Conclusions

The time over which magnetic reconnection occurs in a regime characterized by intense lasers and relativistic inflows has been measured, and was found (with the Omega EP pulse parameters) to be comparable to the laser pulse duration. Perhaps more accurately, it may be compared to the duration of the burst of relativistic electron from the interaction site, which typically exceeds the laser pulse duration. This value was measured on Omega EP to be $\approx 24 - 28$ ps when firing 500 J/pulse onto a pure copper target. While these measurements were collected by firing directly onto a copper target, they indicate that the relativistic electron burst may be expected to exceed the pulse duration [129, 130].

While an experimental measurement of the *rate* of reconnection was not possible (this being the speed at which flux conservation is violated), it can be estimated by the experimantally measured aspect ratios with similar pulse conditions on Omega EP, which yielded values of 0.2-0.3.

Given the expected fast rate of reconnection, it is perhaps not surprising that the recon-

nection time is comparable to the expected burst duration of relativistic electrons.

The observation and temporal characterization of midplane K_α emission generated during magnetic reconnection in this regime will verify that magnetic potential energy may be converted to plasma kinetic energy over short timescales as indicated by the three-dimensional PIC simulations performed for this thesis.

Chapter 6

Particle Measurements of Reconnection

6.1 Introduction

A dynamic plasma reveals its behavior by a large variety of features: its radiation emission may reveal information regarding its temperature evolution through both spatial, temporal, and spectral measurements. In addition, probing the main plasma or intercepting its particle emissions also reveal pertinent details concerning the plasma behavior. In this Chapter, information is presented related to electron emission measurements and optical probing of the plasma in which magnetic reconnection events are induced.

Electron emission measurements performed on HERCULES, Omega EP, and Titan revealed spectroscopic and spatially resolved information, providing potential signatures of magnetic reconnection. Additionally, optical probe measurements performed on Omega EP revealed visual information regarding the large-scale plasma evolution during and following a reconnection event.

6.2 Experimental setup: HERCULES

The HERCULES laser facility at the University of Michigan, a Ti:Sapphire system with a wavelength of $\lambda = 810$ nm and pulse durations of 40 fs FWHM was utilized. The amplified spontaneous emission (ASE) contrast was reduced with the Cross-Wave Polarization (XPW) [118] correction technique to 10^{-11}. An f/3 paraboloidal mirror was split along its symmetry

axis with one half vertically motorized to allow two wavefront-corrected laser foci to be adjustably separated. With a 4 inch diameter, 100 TW beam incident upon the paraboloid, one focal spot had an approximate FWHM area of 174 μm^2 containing 37.5% of the beam energy, while the other had an approximate FWHM area of 337 μm^2 and 62.5% of the beam energy. Both spots therefore had approximately equal focused intensities of 2×10^{19} Wcm^{-2}.

To measure the spectra of surface electrons generated during the two-beam experiments, a variably filtered scintillating screen was positioned 10 cm from the target chamber center (TCC), placed perpendicular to the target plane. The filtering comprised of four variable-thickness aluminum wedges, with corresponding electron cutoff energies of 34 keV, 83 keV, 126 keV, and 188 keV. The variable-thickness filter setup is depicted in Figure 6.1.

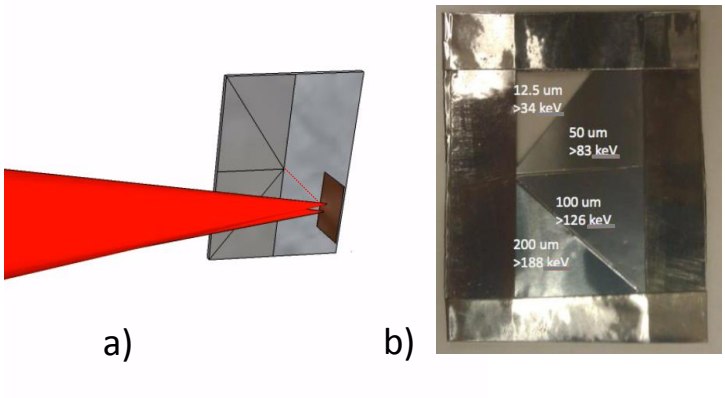

Figure 6.1: The LANEX screen position (a) and filter levels used (b).

The chamber schematic was demonstrated in Figure 4.4.

6.3 Experimental setup: Omega EP

The Omega EP experimental setup for the work described in this chapter is that of Experimental Configuration 2 (Section 4.5).

Multiple experiments conducted at Omega EP utilized Electron-proton-positron spectrometers (EPPS)s (described in Section 3.3.6), positioned along the laser axes, 40 cm from TCC. They were utilized to measure the dependence of the electron plume temperature and flux as a function of laser conditions, and in extension to characteristics of magnetic reconnection.

The Osaka University Electron Spectrometer (OU-ESM) introduced in Section 3.3.6 was utilized in one Omega EP experiment along the Beamline 1 transmitted axis to measure the angular dependence of the electron plume. The device utilized five channels at angles of -10°, -5°, 0°, 5° and 10° with respect to the laser axis, positioned to the target rear at a stand-off distance of 400 mm and an on-axis rotation of 73°. This corresponded to a set of compound angles 54.3°, 55.3°, 56.6°, 58.2°, and 60.0° from the target rear normal. Magnet pairs with 4.5 kG field strengths were utilized on all channels, which dispersed electrons to energy-dependent positions on BAS-MS image plates. The experimental geometry for the OU-ESM is presented in Figure 6.2.

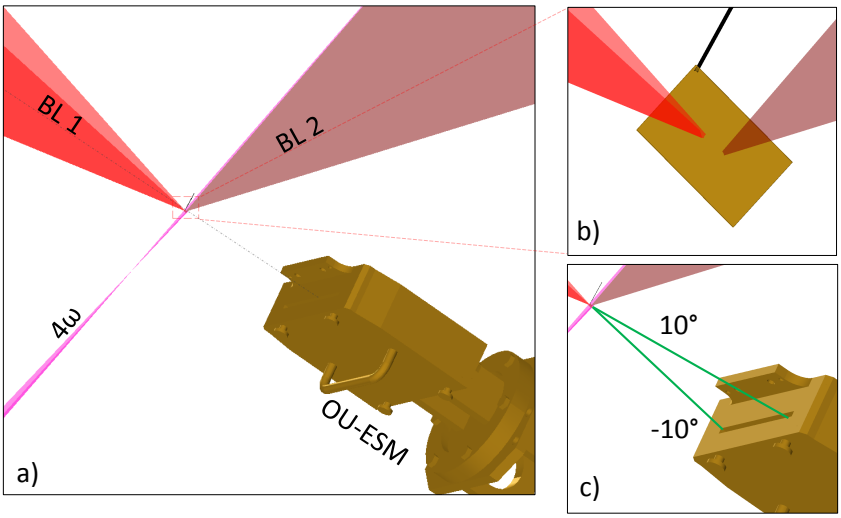

Figure 6.2: The experimental geometry for the OU-ESM as utilized on Omega EP. The OU-ESM positioned along BL1 and rotated 72° along its axis. Subplot (a) demonstrates this geometry, along with the incoming 4ω optical probe, while subplot (b) is a magnefied view of the laser focusing positions on the planar copper foil target (separated by 500 μm), and subplot (c) demonstrates the 20° angle of coverage of the spectrometer.

Additionally, the 4-ω probe (see Section 3.3.7 for details) was utilized to simultaneously measure shadowgraphy, angular filter refractometry, and polarimetry of the two interacting plasmas. The 4-ω probe viewed the target from the side, with the perspective displayed in Figure 6.3.

The AFR leg of the 4-ω diagnostic utilized a variably spaced ring aperture in the Fourier plane, while the shadowgraphy leg utilized no filter, and a third leg utilized a Wollaston

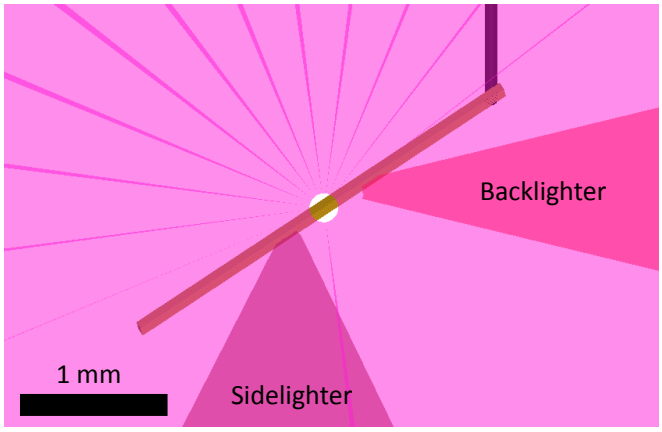

Figure 6.3: A view along the axis of the 4-ω optical probe.

prism to separate and measure the polarization components of the probe beam. The beam's polarization is rotated via the Faraday effect as the beam propagates through the plasma's magnetic field, and thus an estimate of the magnetic field topology may be inferred from the images of the polarization rotation and a plasma density may be measured.

6.4 Experimental setup: Titan

The Titan laser was used with pulse durations of both 0.7 ps and 10 ps, with corresponding nominal energies of 140 J and 240 J, respectively. The energy was split into two pulses, resulting in nominal focused intensities of 6×10^{19} Wcm^{-2} and 7×10^{18} Wcm^{-2}, with a 15 μm FWHM focal spot size.

Two EPPS devices were utilized along the axes of both beams, at a distance 43.5 cm from TCC along BL 1, and 47.5 cm along BL 2. The Titan chamber schematic indicating the EPPS positions was provided in Figure 4.8.

6.5 Results

6.5.1 Electron Measurements

On the HERCULES laser, the scintillating screen recorded measurements of relativistic surface electrons during the focal spot separation scan. For each separation, 4-5 shots were

taken and the resulting images were averaged to produce the data displayed in Figure 6.4.

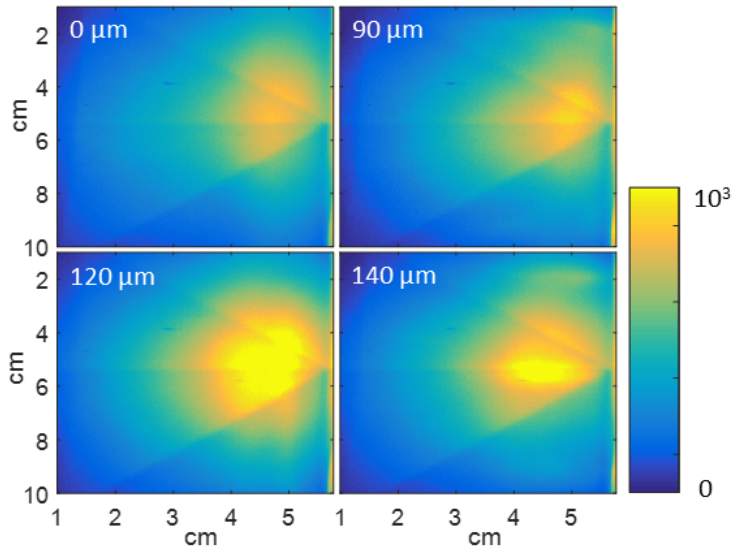

Figure 6.4: The LANEX measurements of surface electron measurements from the HERCULES experiments, as a function of the indicated focal spot separation. Each image is a calculated average over 3-4 shots with identical conditions.

By analyzing the variable filters of the LANEX screen, it was determined that the measured electron temperature was $O(100$ keV), and did not vary significantly as a function of spot separation. However, the integrated signal consistently displayed a local maximum at the 120 μm separation with 30% more flux compared to the 0 μm separation case (Figure 6.5). While the images in Figure 6.4 display beam-like structure, this is due to the $1/r^2$ falloff from the approximately spherically expanding electron source, with additional structure imparted by material inconsistencies in the target and the detector.

On Omega EP, an Electron Positron Proton Spectrometer (EPPS) was utilized along the transmitted axes of both laser pulses during the focal scans described in Section 4.7.1. The spectra collected with these devices are presented in Figure 6.6. While one direction observed a consistent decrease in electron cutoff energies (defined when the flux decreased below 10^9 photons/MeV/sr), the other direction observed higher cutoffs at intermediate separations (Figure 6.7 a). For the 500 J/pulse shots, a maximum was observed in the electron temperature along the direction of beam 2, but was seen to be negligible along beam 1 (Figure 6.7 b).

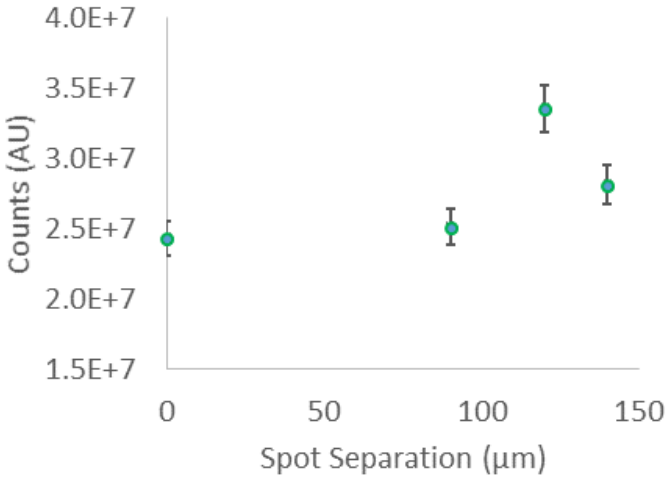

Figure 6.5: The LANEX measurements of surface electron measurements from the HERCULES experiments, indicating the integrated fluorescent flux as a function of focal spot separation.

While no identifiable pattern was found, the EPPS data suggested dependence of the electron spectra upon the focal spot separation. This may indicate heating or introduced directionality of expelled electrons by mechanisms related to magnetic reconnection. To explore this effect further, a multi-channel electron spectrometer was utilized along the direction of Pulse 1, which was positioned 35 cm from TCC and which had an angular coverage of 20 degrees with respect to the transmitted laser axis.

The summarized results from the multi-channel electron spectrometer are displayed in Figure 6.8, which show occurrences of nonthermal electron contributions with significant angular dependency.

With both beams firing with 1 kJ/pulse and a separation of 500 μm, the spectrometer revealed a nonthermal population of electrons superimposed upon a quasi-Maxwellian temperature distribution. The flux of this supra-thermal population increased as the angular array of spectrometers viewed the target at angles closer to the rear target normal, suggesting that the electrons are emitted preferentially from the midplane region. A 100 ps delay between Pulses 1 and 2 was introduced and a copper target shot with the same separation. This eliminated the observed supra-thermal features (Figure 6.9).

The non-Maxwellian features were observed for all simultaneous-firing shots except for

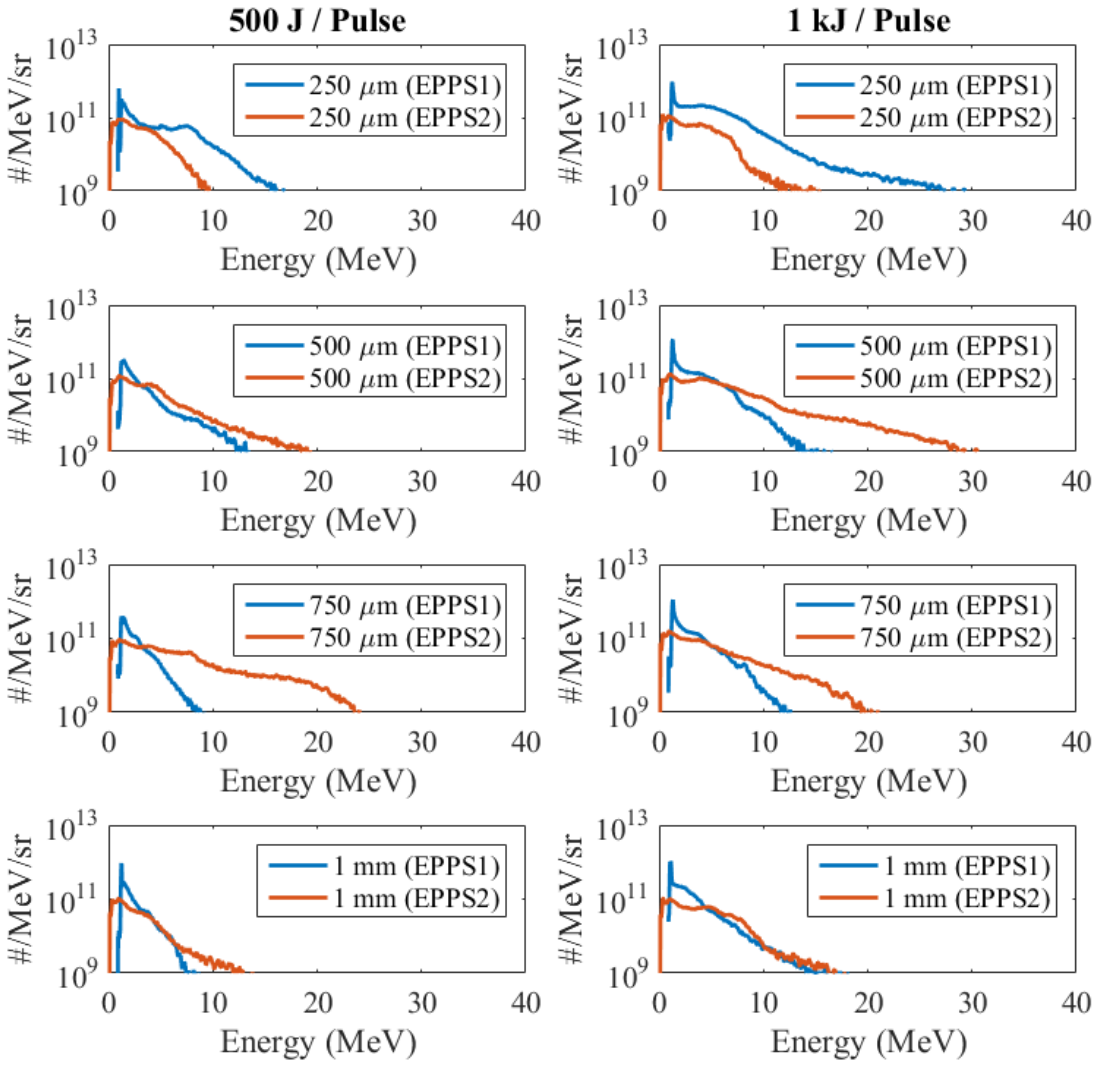

Figure 6.6: The summarized EPPS spectra collected for the varying pulse energy and focal spot separation.

one, with the features displaying angular fluctuation shot-to-shot. The direction of the reconnection-accelerated electrons is therefore potentially depends sensitively upon the plasma conditions. Further, the change occurs over a narrow range of compound angles from the target rear normal; sampling a larger range of angles should be a priority for future experiments to determine the significance of this detected variation.

Two EPPS devices were utilized along the laser axes on Titan, which resulted in the

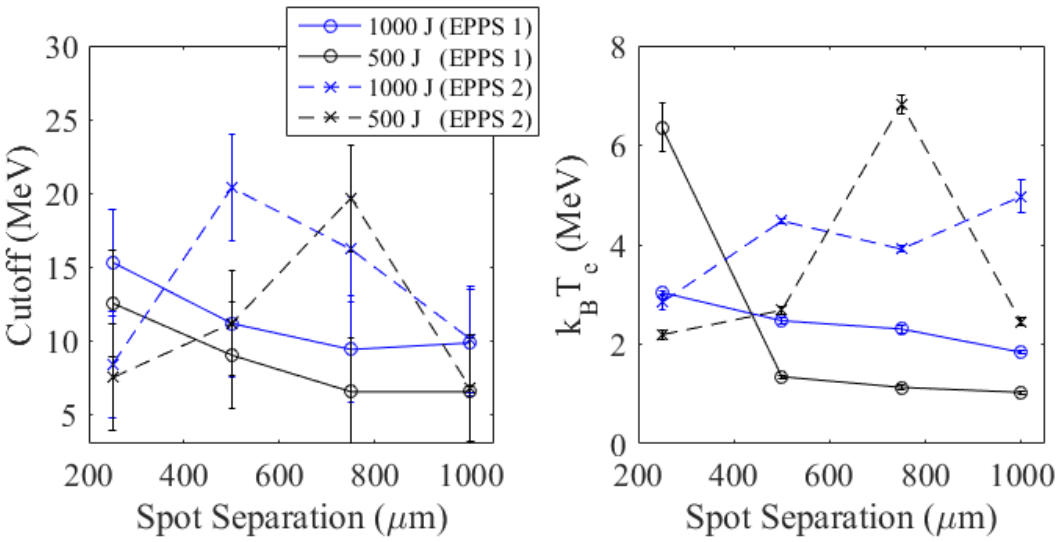

Figure 6.7: a) Electron cutoff energies as measured by EPPS 1 (along beam 1) and EPPS 2 (along beam 2) for the two energy settings utilized on OMEGA EP. The error bars represent the shot-to-shot variation in cutoff energy for identical beam and target conditions. b) Calculated electron temperatures corresponding to the same spectra.

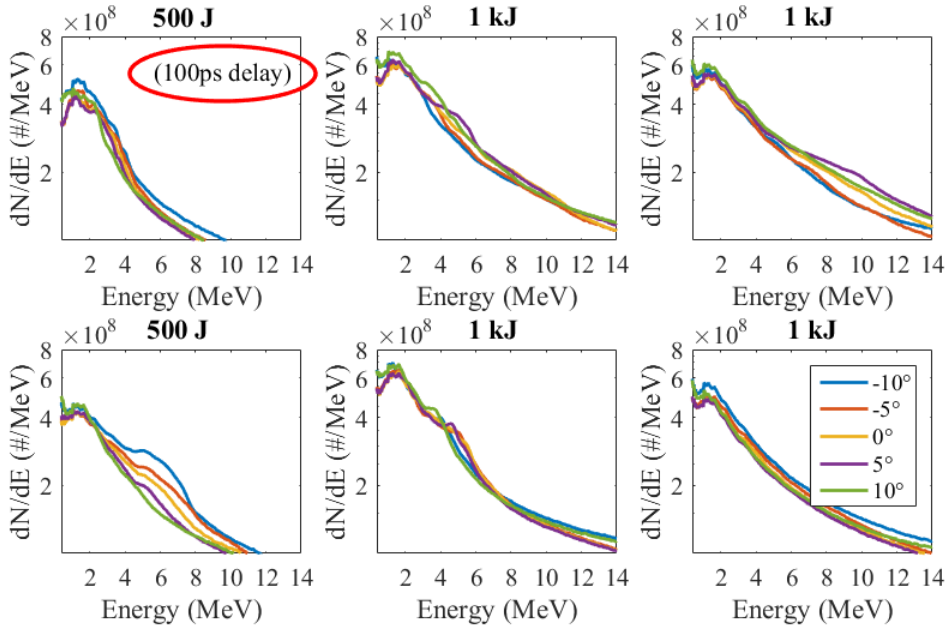

Figure 6.8: Electron spectra as a function of angle from the transmitted laser axis for a variety of shots with identical pulse conditions.

measured temperatures plotted in Figure 6.10. While no dependence on beam separation was observed, it was confirmed that the higher intensity pulses resulted in hotter electron

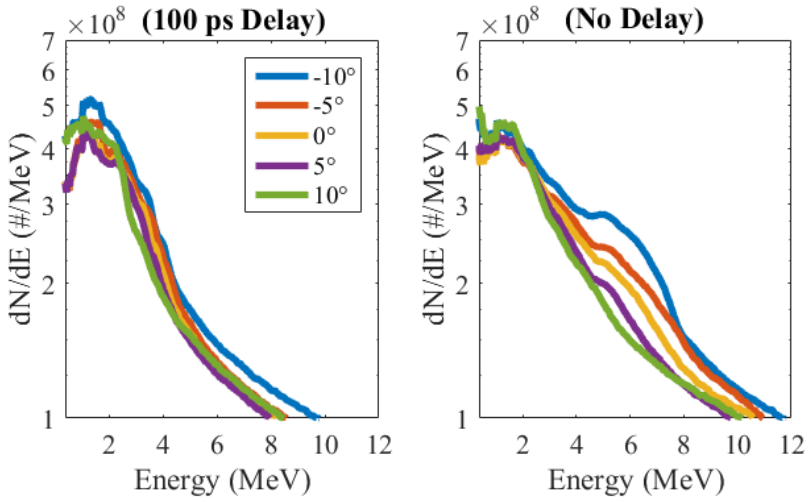

Figure 6.9: Electron spectra as a function of angle from the transmitted laser axis for the case of an intentional 100 ps delay between Pulse 1 and 2 (Left) and no delay (Right).

temperatures.

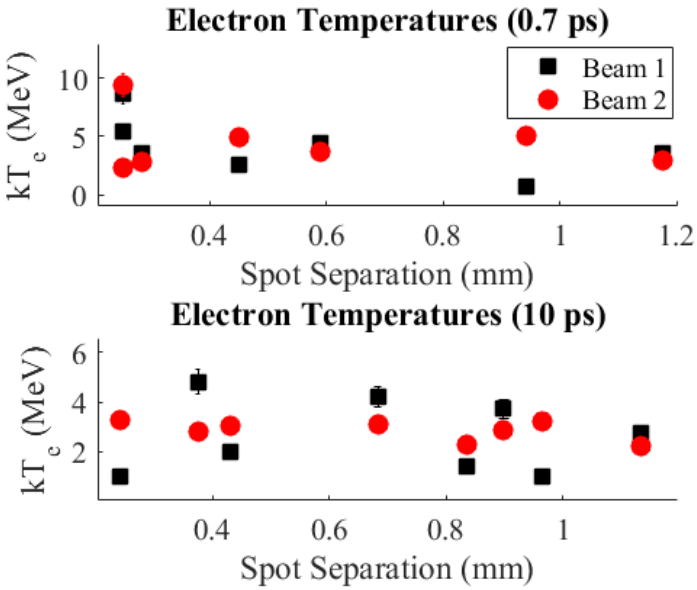

Figure 6.10: The accelerated electron temperatures measured along the laser axes, modeled as Maxwellian. The top figure demonstrates the temperature for either Beam 1 or Beam 2 for the 0.7 ps pulse duration, while the bottom figure demonstrates the temperatures for the 10 ps pulse duration.

6.5.2 Optical Probing

The 4-ω optical probe was utilized to record shadowgraphy, angular filter refractometry (AFR), and polarimetry of the two-pulse interaction at various delays after the beam arrival time.

The polarimetry data was desired to provide a measurement of the oppositely oriented magnetic field structure early in time. For a variety of delays between the optical probe and the beam arrival time, the polarization rotation was determined by the procedure outlined in Section 3.3.7. The result is demonstrated in Figure 6.11.

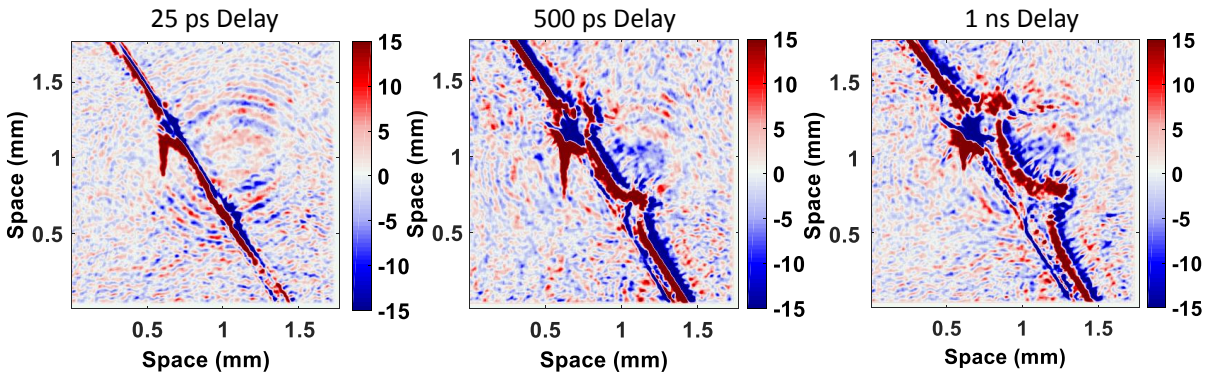

Figure 6.11: The calculated polarization rotation of the 4-ω optical probe, which arrived 25 ps, 500 ps, and 1 ns following beam arrival. The scale is in units of degrees, and the two lasers are incident from the right of the imaged target.

No indication of surface magnetic field structure were observable over the noise level at the 25 ps delay. This is due to the small thickness of the plasma at this time (< 100 μm), which is comparable to the spatial scale of the speckle noise in the image of the probe beam. At much later times (well after the anticipated reconnection event), large-scale magnetic field structure is evident, with evidence of a density perturbation in the midplane region at the 1 ns delay.

Figure 6.12 demonstrates the summarized results from the AFR diagnostic, which (while providing an insufficient number of fringes to yield a detailed plasma density profile at early times) clearly showed the boundaries of the hydrodynamically expanding plasma later in time.

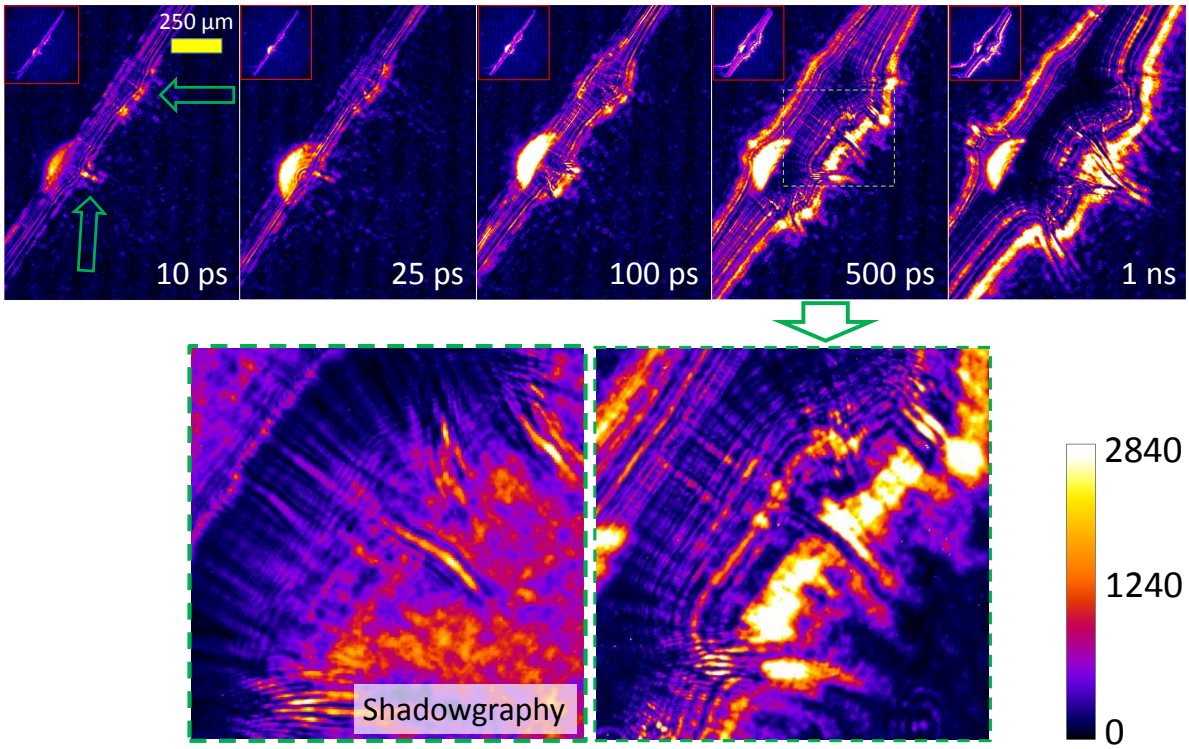

Figure 6.12: A summary of the angular filter refractometry (AFR) results, as a function of the delay between the dual pulse arrival and the arrival of the 4-ω optical probe. The midplane structure seen at 500 ps is expanded, and compared to the analogous shadowgraphy image collected simultaneously.

In addition to these boundaries, a sharp density perturbation is observed in the focal midplane region at 500 ps following the pulse arrival time. This feature is more clearly observed using the shadowgram, given that the AFR diagnostic is limited in resolution by diffraction from optical elements in the near-field. The shadowgraphy revealed that this feature is 20 μm wide and 170 μm long. While an involved hydrodynamic simulation of the two-beam interaction is required to model the density of this feature above the background plasma, it is clear that the feature is consistent with that of a narrow density perturbation.

The shadowgraphy diagnostic delivers information via the displacement of the probe light, and the degree of displacement is given by $\Delta I/I \propto d^2 n_e/dx^2$. Figure 6.13 demonstrates the comparison of a lineout across the shadowgraphy perturbation to that derived from assuming a local Gaussian density depression.

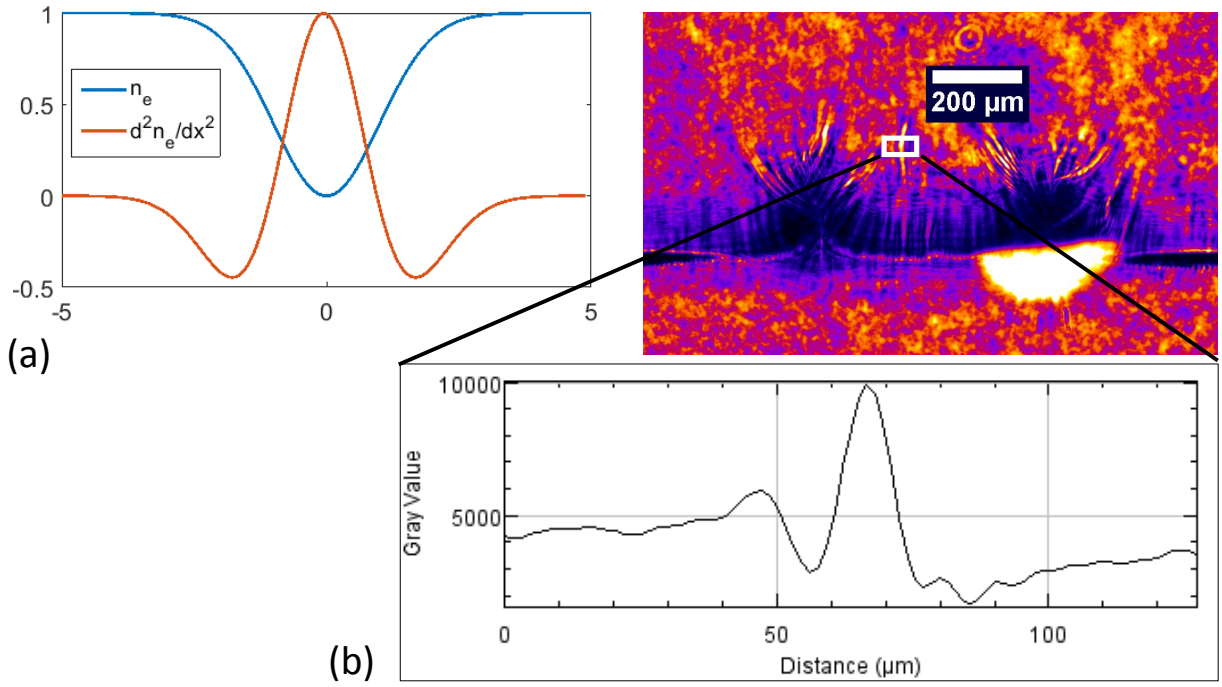

Figure 6.13: (a) Demonstration of a local electron plasme depression leading to a local maximum of its second derivative. (b) An enhanced lineout of the shadowgraphy density purbertubation.

From Figure 6.13, it is clear that the feature is a local density depression in the plasma profile. This structure may be evidence of target heating in the midplane region by the reconnection electric field, or may potentially indicate the presence of an outflow jet propagating at a large angle from the target plane.

The shadowgraphy data additionally provides a measurement of the hydrodynamic speed at which the plasmas propagate outward, which was measured as 2.5×10^5 m/s.

6.6 Simulations

The simulation results discussed in Sections 4.8 and 5.5 allow comparisons to the experimental results regarding the relativistic electron spectra.

The surface electrons generated during the interaction in the simulation have a temperature of ~ 1 MeV, which is comparable to the HERCULES measurements of surface electrons which was determined to be $O(100$ keV$)$.

Electron acceleration is observed within the reconnection in the longitudinal direction, which develop a nonthermal spectral component in addition to a bi-Maxwellian low-energy portion. The nonthermal component was fitted with a power law $f(\gamma) \sim \gamma^{-1.56}$, consistent with reconnection in the relativistic regime. The maximum value of $\gamma_{||}$ is consistent with the time over which the electric field acts upon the electrons, via the simple estimate $m_e c^2 \gamma_{max} = \int |qE_{peak}| cdt$. A time-integrated total amount of energy of 35.8 GeV is transferred to energetic electrons in the reconnection region. Figure 6.14 displays the laser-longitudinal electron momentum and energy spectrum, respectively, evaluated in either a $78c/\omega_0$-wide region surrounding the reconnection region (red curve) or an area chosen exterior to this region (black curve). Outputs are shown at $t = 0$ (top row) and at $t = 5\tau_p$ (bottom row) where τ_p is the FWHM laser pulse duration.

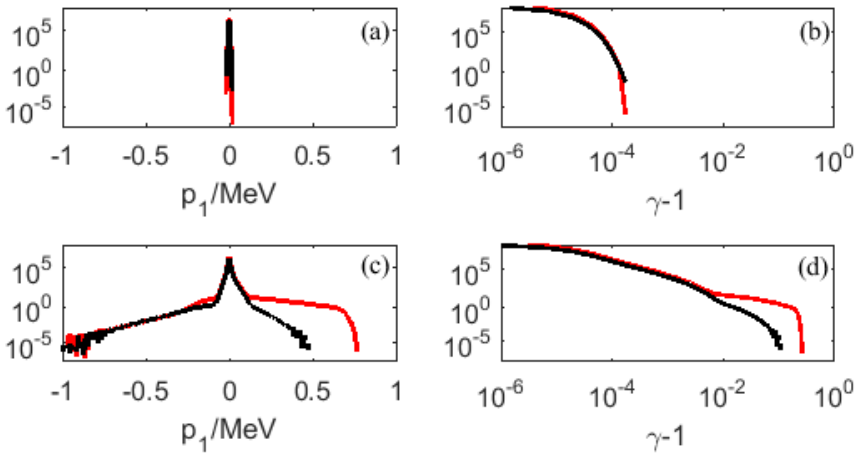

Figure 6.14: Momenta of electrons propagating in the laser longitudinal direction (left column) and corresponding energy spectra (right column) at the simulation initiation time (top row) and at $t = 5\tau_p$ (bottom row). Red curves correspond to variables evaluated within the reconnection region and black curves are evaluated exterior to this region. The vertical axes are either dN/dp_1 or $dN/d\gamma$ with arbitrary units. Positive momentum values correspond to the laser propagation direction.

Evidence for outflow along the long axis of the reconnection region was found from phase space calculations comparing inflow to outflow electrons. Comparisons are shown from two time steps in Figure 6.15, suggesting that at later stages of the reconnection region development, electrons gain energy from the reconnection fields.

Comparison of the phase space in the reconnection region between this 3 dimensional

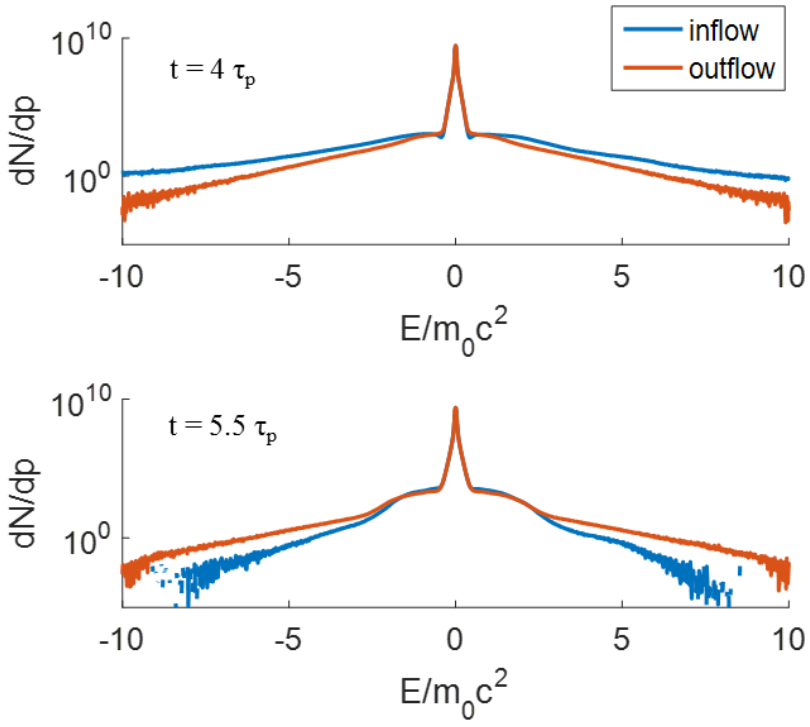

Figure 6.15: Comparisons of inflow (along x_2) and outflow (along x_3) electron distributions at two time steps, showing the transition to the phase during which electrons gain significant energy from the reconnection fields in the outflow direction.

simulation and an analogous 2 dimensional simulation (with identical pulse and plasma parameters, but with a 75 μm separation instead of 500 μm) was performed, to search for features unique to the occurrence of magnetic reconnection. The 2 dimensional simulation only included the laser longitudinal direction and one laser transverse direction, thus making magnetic reconnection impossible. The results of the phase space comparison are demonstrated graphically in Figure 6.16.

Figure 6.16 demonstrates that when simulating the interaction in 3D, a new phase space structure appears as a concentrated region at relatively high momentum values (in addition to the nonthermal component previously modeled with a hard power-law spectrum). The structure may be due to a combined effect of the target-normal electric field and the neighboring curved magnetic field reversal structure. This structure may be related to the narrow-spread electron distribution measured by the OU-ESM electron spectrometer. This feature does not appear in the spectra displayed in Figure 6.14 due to spatial averaging

through the reconnection region.

6.7 Conclusions

The measurement of particle emissions and plasma densities during two-beam experiments can provide evidence of magnetic reconnection. The presence of electrons displaying separation-dependent angular variation suggests significant magnetic field influence (as in the case of the EPPS measurements), and the OU-ESM measurements suggested a population of electrons are preferrentially accelerated along the target rear normal – implying the influence of the reconnection electric field. Optical probe measurments indicated structure in the diffusion region which may be indicative of a hydrodynamic response of the reconnection current sheet formation.

The HERCULES measurements show evidence of surface electron currents, although any contribution from reconnection appeared to be small. Therefore, the use of a spectrometers on Omega EP was integral in inferring reconnection-accelerated electrons via the detailed population characteristics, albeit measured in a different plane due to experimental constraints.

The 3D simulation indicates the development of spectral characteristics consistent with magnetic reconnection in the relativistic regime, with quasi-monoenergetic characteristics in the target normal direction.

Additional work can be done to further explore these effects, such as utilizing an array of electron spectrometers with additional angular coverage. Additionally, utilizing targets comprised of plastic may result in a larger scale length plasma, resulting in potentially better resolved magnetic field measurements with optical probe polarimetry. Such an increase in scale length may also be achieved by pre-irradiating the target $\sim O(100$ ps) prior to the dual beam arrival time.

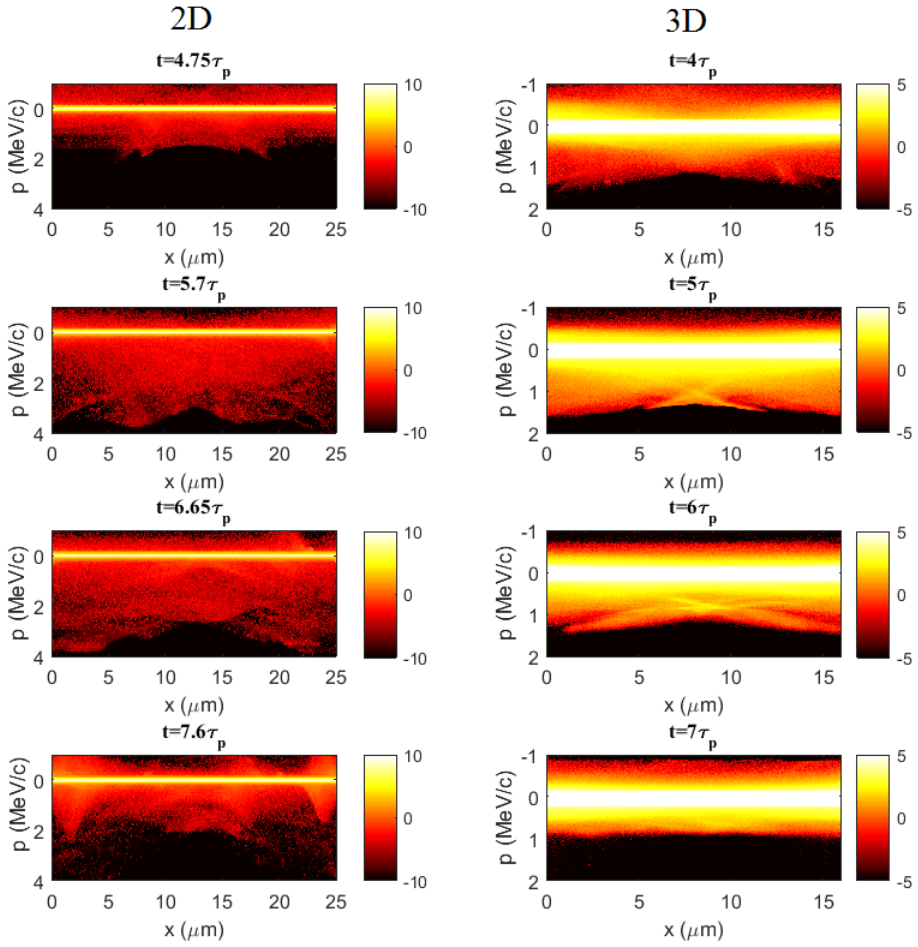

Figure 6.16: Phase space images of the reconnection region compared between the 3D simulation and an analogous 2D simulation, with the x-value corresponding to the dimension along which the two focal spots are separated and the momentum corresponding to the target-normal direction (with positive values corresponding to motion directed into the denser portions of the plasma). The results are presented in different scales due to the difference in the total number of particles between the two simulations. Effort was made to present the data in such a way as the features of interest are easily visible.

Chapter 7

Conclusions and Outlook

7.1 Summary and Discussion

Evidence has been presented for laser-driven, fast magnetic reconnection occurring a regime characterized by relativistic inflows and a ratio of magnetic energy density to electron rest mass energy density exceeding unity. The reconnection conditions were generated by focusing high power, short-pulse lasers onto solid metal foils.

By performing such experiments in a controlled, laboratory setting, it is shown that conditions relevant to high-energy astrophysical phenomena such as gamma-ray bursts, pulsar wind emissions, and active galactic nuclei emissions can be achieved. The use of high-intensity laser systems in particular was paramount in order to achieve sufficiently large magnetic fields to reach the regime characterizing these astrophysical systems.

The lasers utilized were:

1. The HERCULES Laser, Center for Ultrafast Optical Science, University of Michigan, Ann Arbor MI.

2. The Omega EP Laser System, Laboratory for Laser Energetics, Rochester NY.

3. The Titan Laser, Jupiter Laser Facility, Lawrence Livermore National Laboratory, Livermore CA.

Evidence for reconnection in this regime was collected with X-ray emission detection

(both spatially and temporally resolved), accelerated plasma measurements, and optical probing techniques. Finally a fully 3-D PIC simulation was run to further characterize the details of the reconnection process.

The results of the conducted experiments are summarized and discussed below.

7.1.1 X-Ray Emissions

Two high-intensity lasers were focused with variable separation ≤ 1 mm onto bulk copper targets.

Spatially-resolved K_α emission measurements collected with a spherical X-ray crystal allowed the identification of the reconnection region between the focal spot locations, wherein magnetic field lines break and reconnect. Because this process is associated with a localized reconnection electric field which accelerated electrons into the plasma density gradient, a localized enhancement of K_α emission was observed and associated with the spatial extent of the current sheet.

The dimensional characteristics of this region were measured, enabling approximations of the reconnection rate. It was determined that the reconnection rates measured were fast (> 0.1) (Section 4.7.1).

Broadband X-ray pinhole measurements were performed (Section 4.7.2), which resulted in no detectable midplane emission in the range of 2-6 keV. This result indicates that the observed K_α emission is not a byproduct of collisional heating of two plasmas but is rather consistent with high-energy electrons accelerated into the plasma density gradient by a reconnection electric field.

An X-ray crystal spectrometer was used to distinguish between the copper K_α and K_β photons emanating from the mid-plane region only (Section 4.7.3). This enabled the calculation of the temperature from which the K-photons originate during reconnection, resulting in negligibly small temperature values. By only firing single pulses, the resultant K-photons from the mid-plane region were observed with the same techniques to originate from a much hotter plasma ($T_e \approx$ 155-167 keV).

7.1.2 Temporal Measurements

On Omega EP, the spherical K_α crystal imaged K_α emissions from a specialized target onto an ultrafast X-ray streak camera in Experimental Configuration 2 (Figure 4.5). The specialized targets were comprised of copper only in the midplane region where the current sheet forms (Figure 4.7). This resulted in measured K_α emission durations equal to $\Delta t \approx 27$ ps in the case of a 500 μm focal spot separation, and $\Delta t \approx 22$ ps in the case of a 750 μm focal spot separation (Figure 5.7). The longer duration of emission in the case of the smaller focal spot separation is potentially due to the larger amount of magnetic energy to be converted, as the magnetic field falls with distance from the focal spot locations.

7.1.3 Particle Measurements

On the HERCULES laser system, a variably filtered LANEX screen was positioned 10 cm from the target, positioned normal to the target plane (Figure 6.1). The focal spots were separated vertically, and the LANEX positioned such as to intercept electrons comprising the reconnection outflow. It was determined that the electron temperature was of order 100 keV, which did not vary significantly as the focal spot separation was varied. However, the integrated signal revealed a maximum at the 120 μm separation, with 30% more signal compared to the zero-separation case. This result is significant as the integrated midplane signal as measured by the K_α crystal was also maximized at a comparable separation of ≈ 140 μm.

On Omega EP, charged particle spectrometers were positioned along the transmitted laser axes in Experimental Configuration 1 (Figure 4.4). This resulted in focal spot separation dependence upon the electron spectra, potentially suggesting a directionality of expelled electrons caused by the occurrence of reconnection (Figure 6.6). By utilizing a 5-channel electron spectrometer in Experimental Configuration 3 (Figure 4.6), it was found that a nonthermal, quasi-monoenergetic feature appears in the electron spectra as one approaches compound angles closer to the rear target normal, potentially sampling the population of electrons which were accelerated by the reconnection electric field into the plasma density gradient (Figure 6.9).

Again on Omega EP, optical probing techniques in Experimental Configuration 3 revealed a late-time ($\gtrsim$ 500 ps) midplane plasma density perturbation which may be a response to plasma heating in the midplane due to reconnection, or may indicate the presence of plasma jets inclined at large angles from the target surface (Figure 6.12).

7.1.4 PIC Simulation

A 3-D PIC simulation was performed in which two laser pulses with FWHM duration 40 fs, central wavelength 810 nm, and focused intensity of 2×10^{21} Wcm^{-2} were focused with a 50 μm separation onto a pre-plasma with scale length $= \lambda$. Ions were stationary and the simulation modeled $3 \times 3 \times 3$ particles per cell. More details are provided in Appendix A.

Various features of reconnection were observed, including:

1. The formation of a current sheet region wherein magnetic field lines reconnected, with dimensional characteristics resulting in an aspect ratio of $\approx$0.3, which is near the experimentally measured values.

2. The formation of a reconnection electric field, with a normalized magnitude equal to $E_{REC}/cB_{REC} = 0.3$ (Figure 4.28).

3. A population of electrons accelerated into the plasma density gradient to high energy, with spectral characteristics expected from reconnection (Figure 5.10).

Significantly, it was found that the magnetization parameter $\sigma \equiv B^2/(\mu_0 n_e m_e c^2)$ exceeded $\sigma = 1$ in a significant percentage of the plasma, indicating that the interaction is that of *relativistic* reconnection (Figure 4.31). Therefore, high intensity laser-plasma experiments may be a test bed for high-energy astrophysical phenomena in which strong magnetic fields may accelerate plasma to relativistic speeds.

7.2 Outlook

Even higher magnetic field magnitudes (and thus potentially even higher plasma magnetization) may possibly be achieved with the next generation of high-intensity lasers, for example

the ELI facility which aims to deliver peak powers of 200 PetaWatts [124]. This might allow extensive and thorough laboratory research of high-energy astrophysical events, at high repetition rate.

Additionally, the high rate of positron production in the high-intensity regime [131, 132] could allow the study of magnetic reconnection in electron-positron plasmas, which are thought to exist in high-energy astrophysical plasmas such as in gamma ray bursts [133].

With existing (or easily attainable) laser and diagnostic technology, additional research can be performed to further characterize the reconnection regime investigated in this thesis.

Direct magnetic field measurements with proton deflectometry would be valuable in directly observing the changing field topology and in measuring the dimensions of the region of the midplane magnetic null. This was not possible at the facilities utilized due to the limited number of short-pulse beam lines, but was instead inferred from spatially resolved X-ray signatures.

Additionally, varying the pre-plasma scale-length with which the main pulse interacts would be interesting due to the corresponding dependence of the magnetic field's magnitude and spatial extent in the direction of the plasma density gradient [56].

While the work presented in this thesis describes the first laboratory experiments on relativistic magnetic reconnection, there is much work yet to be performed. It is the hope of the author that the torch is taken up by many capable scientists and that it leads to a deeper understanding of both fundamental physics and the internal workings of high-energy astrophysical phenomena.

Appendix A

OSIRIS Simulation Parameters

The particle-in-cell (PIC) code OSIRIS [116] was utilized to run a fully relativistic, fully 3-dimensional simulation of a two-beam laser/plasma interaction to demonstrate magnetic reconnection with the HERCULES laser conditions.

Figure 1 depicts the simulation box dimensions and boundary conditions.

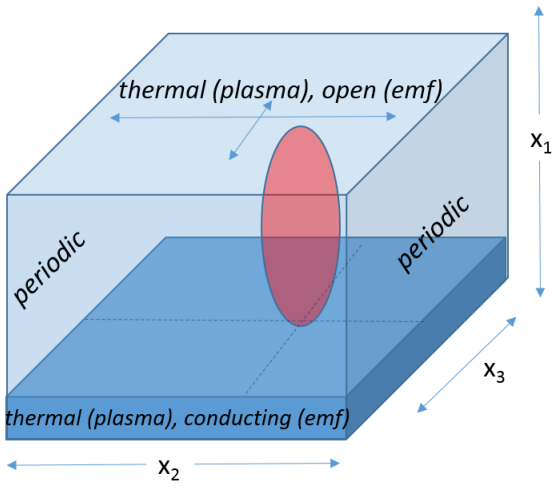

Figure A.1: The simulation box dimensions for the OSIRIS simulation.

In simulation units, the box ranges from $x_1 \in [-150, 35]c/\omega_0, x_2 \in [0, 387.9]c/\omega_0, x_3 \in [0, 775.8]c/\omega_0$.

The laser pulse has a Gaussian field envelope with rise and fall times of 20 fs, a focused intensity corresponding to $a_0 = 3$, and focal FWHM of $87.75c/\omega_0$. The pulse is initialized at

$x_1 = -50c/\omega_0$ and with a transverse offset in x_2 by $129.3c/\omega_0$.

The plasma is an electron plasma with maximum density $n_{max} = 30n_{crit}$, with an exponential density ramp which rises with a scale length $L = \lambda$ and reaches the maximum value at $x_1 = 0$. The plasma extends to the lower longitudinal boundary $x_1 = 35$ and makes contact with the boundaries of x_2 and x_3. The electron plasma had $3 \times 3 \times 3$ particles per cell and was initialized with a thermal velocity distribution. Additionally, stationary ions were generated by OSIRIS.

Open space boundaries were utilized in the laser longitudinal direction for fields, with thermal boundaries utilized for particles. Thus, electrons which are heated by the laser and propagate to the $x_1 = 35$ boundary are replaced by a particle with a random direction and a velocity determined by a pre-defined thermal distribution identical to the initial distribution. Periodic boundaries were utilized for fields and particles in the laser transverse directions to simulate a two-spot geometry, resulting in an effective focal spot separation of $387.9\omega_0/c$.

The spatial resolution in the simulation was $\Delta x_1 = \Delta x_2 = \Delta x_3 = 0.165c/\omega_0$, with 6 cells per c/ω_L and 1 cell per c/ω_p at the maximum electron plasma density. The Courant condition was met with a timestep of $\Delta t = 0.093$.

The *input deck* utilized to run the simulation is provided below.

```
   node_conf
{
node_number(1:3) = 14, 30, 60,
if_periodic(1:3) = .false., .true., .true.,
}

   grid
{
nx_p(1:3) = 1120, 2400, 4800,
}

   time_step
{ dt = .093,
```

```
ndump = 100,
}

   restart
{
ndump_fac = 1,
if_restart = .true.,
if_remold = .true.,
}

   space
{ xmin(1:3) = -150, 0, 0,
xmax(1:3) = 35, 387.9, 775.8,
if_move(1:3) = .false., .false., .false.,
}


time
{
tmin = 0.0,
tmax = 910.0,
}

emf_bound
{
type(1:2,1) = 30, 30,
}

   diag_emf
{
```

```
ndump_fac= 0,
ndump_fac_ave = 1,
n_ave(1:3) = 4, 4, 4,
reports = "e1, savg", "e2, savg", "e3, savg",
"b1, savg", "b2, savg", "b3, savg",
}

  particles
{
num_species = 1,
num_neutral = 0,
ndump_fac = 0,
ndump_fac_ave = 1,
}

  species
{
name = "electrons" ,
num_par_max = 65000000,
num_par_x(1:3) = 3, 3, 3,
rqm=-1.0,
vth(1:3) = 0.01 , 0.01 , 0.01 ,
vfl(1:3) = 0.0 , 0.0 , 0.0 ,
den_min = 1.d-3,
interpolation = "linear",
}

  profile
{
density = 30.0,
```

```
profile_type(1:2) = "math func",
math_func_expr='1.0
/(1.0+exp(-1.0/6.28*(x1+3.1415)))*(x1<35.0)',
}

   spe_bound
{
type(1:2,1) = 50, 50, !  thermal
pth_bnd(1:3,1,1)=0.01,0.01,0.01,
pth_bnd(1:3,2,1)=0.01,0.01,0.01,
thermal_type="random dir",
}

   diag_species
{
ndump_fac_ave = 1,
n_ave(1:3) = 4, 4, 4,
reports = "charge, savg",
ndump_fac_pha = 1,
ps_xmin(1:3) = -150, 0, 0,
ps_xmax(1:3) = 35, 387.9, 775.8,
ps_nx(1:3) = 1120, 2400, 4800,
ps_pmin(1:3) = -20.0, -20.0, -20.0,
ps_pmax(1:3) = 20.0, 20.0, 20.0,
ps_np(1:3) = 4000, 4000, 4000,
if_ps_p_auto(1:3) = .false., .false., .false.,
ps_gammamin = 1.0,
ps_gammamax = 200.0,
ps_ngamma = 2000000,
phasespaces = "x2x1","g", "p1x1", "p2x1", "p3x1", "p1x2",
```

```
"p2x2", "p3x2","p2p1", "p3p1",
"p3p2","x3x1","x3x2","p1x3","p2x3","p3x3",
ndump_fac_raw = 0,
}

   zpulse
{
a0 = 3,
omega0 = 1.0,
pol = 0.0d0,
propagation = "forward",
direction=1,
lon_type = "polynomial",
lon_rise = 47.6,
lon_flat = 0.0,
lon_fall = 47.6,
lon_start =85,
per_offset = 64.65,
per_type = "gaussian",
per_fwhm = 38.75,
per_focus = 50,
}

   smooth
{
smooth_type = "compensated",
}

diag_current
{
```

```
ndump_fac = 0,
ndump_fac_ave = 1,
n_ave(1:3) = 4, 4, 4,
reports = "j1, savg", "j2, savg","j3, savg",
}
```

Bibliography

[1] M. G. Haines. Magnetic-field generation in laser fusion and hot-electron transport. *Canadian Journal of Physics*, **64**, 912 (1986).

[2] H. C. Spruit. The source of magnetic fields in neutron stars. *Proceedings of the International Astronomical Union*, **4**, 61 (2008).

[3] T. G. Forbes. Solar physics: Flares caught in the act. *Nature Physics*, **9**, 456 (2013).

[4] Y. Su, A. M. Veronig, G. D. Holman, B. R. Dennis, T. Wang, M. Temmer, and W. Gan. Imaging coronal magnetic-field reconnection in a solar flare. *Nature Physics*, **9**, 489 (2013).

[5] X. H. Deng and H. Matsumoto. Rapid magnetic reconnection in the Earth's magnetosphere mediated by whistler waves. *Nature*, **410**, 557 (2001).

[6] M. Øieroset, T. D. Phan, M. Fujimoto, R. P. Lin, and R. P. Lepping. In situ detection of collisionless reconnection in the Earth's magnetotail. *Nature*, **412**, 414 (2001).

[7] B. Cerutti, G. R. Werner, D. A. Uzdensky, and M. C. Begelman. Gamma-ray flares in the Crab Nebula: A case of relativistic reconnection. *Physics of Plasmas*, **21**, 056501 (2014).

[8] E. N. Parker. Sweet's mechanism for merging magnetic fields in conducting fluids. *Journal of Geophysical Research*, **62**, 509 (1957).

[9] G. Kopp, G. Lawrence, and G. Rottman. The Total Irradiance Monitor (TIM): Science Results. *Solar Physics*, **230**, 129 (2005).

[10] S. Poedts. Coronal mass ejection: The birth of a solar eruption. *Nature Physics*, **8**, 783 (2012).

[11] J. R. Lemen, A. M. Title, D. J. Akin, P. F. Boerner, C. Chou, J. F. Drake, D. W. Duncan, C. G. Edwards, F. M. Friedlaender, G. F. Heyman, N. E. Hurlburt, N. L. Katz, G. D. Kushner, M. Levay, R. W. Lindgren, D. P. Mathur, E. L. McFeaters, S. Mitchell, R. A. Rehse, C. J. Schrijver, L. A. Springer, R. A. Stern, T. D. Tarbell, J.-P. Wuelser, C. J. Wolfson, C. Yanari, J. A. Bookbinder, P. N. Cheimets, D. Caldwell, E. E. Deluca, R. Gates, L. Golub, S. Park, W. A. Podgorski, R. I. Bush, P. H. Scherrer, M. A. Gummin, P. Smith, G. Auker, P. Jerram, P. Pool, R. Soufli, D. L. Windt, S. Beardsley, M. Clapp, J. Lang, and N. Waltham. The Atmospheric Imaging Assembly (AIA) on the Solar Dynamics Observatory (SDO). *Solar Physics*, **275**, 17 (2011).

[12] RHESSI MISSION FACTS. `http://hesperia.gsfc.nasa.gov/rhessi2/mission/mission-facts/index.html` (2002).

[13] M. C. Begelman. Instability of Toroidal Magnetic Field in Jets and Plerions. *The Astrophysical Journal*, **493**, 291 (1998).

[14] Y. Lyubarsky and J. G. Kirk. Reconnection in a Striped Pulsar Wind. *The Astrophysical Journal*, **547**, 437 (2001).

[15] D. Giannios. Reconnection-driven plasmoids in blazars: fast flares on a slow envelope. *Monthly Notices of the Royal Astronomical Society*, **431**, 355 (2013).

[16] D. Giannios. Prompt GRB emission from gradual energy dissipation. *Astronomy and Astrophysics*, **480**, 305 (2008).

[17] D. L. Kaplan, S. Chatterjee, B. M. Gaensler, and J. Anderson. A Precise Proper Motion for the Crab Pulsar, and the Difficulty of Testing Spin-Kick Alignment for Young Neutron Stars. *The Astrophysical Journal*, **677**, 1201 (2008).

[18] E. Clausen-Brown and M. Lyutikov. Crab nebula gamma-ray flares as relativistic reconnection minijets. *Monthly Notices of the Royal Astronomical Society*, **426**, 1374 (2012).

[19] J. Aleksić, E. A. Alvarez, L. A. Antonelli, P. Antoranz, M. Asensio, M. Backes, J. A. Barrio, D. Bastieri, J. B. González, W. Bednarek, A. Berdyugin, K. Berger, E. Bernardini, A. Biland, O. Blanch, R. K. Bock, A. Boller, G. Bonnoli, D. B. Tridon, I. Braun, T. Bretz, A. Cañellas, E. Carmona, A. Carosi, P. Colin, E. Colombo, J. L. Contreras, J. Cortina, L. Cossio, S. Covino, F. Dazzi, A. D. Angelis, G. D. Caneva, E. D. C. del Pozo, B. D. Lotto, C. D. Mendez, A. D. Ortega, M. Doert, A. Domínguez, D. D. Prester, D. Dorner, M. Doro, D. Eisenacher, D. Elsaesser, D. Ferenc, M. V. Fonseca, L. Font, C. Fruck, R. J. G. López, M. Garczarczyk, D. Garrido, G. Giavitto, N. Godinović, D. Hadasch, D. Häfner, A. Herrero, D. Hildebrand, D. Höhne-Mönch, J. Hose, D. Hrupec, T. Jogler, H. Kellermann, S. Klepser, T. Krähenbühl, J. Krause, J. Kushida, A. L. Barbera, D. Lelas, E. Leonardo, N. Lewandowska, E. Lindfors, S. Lombardi, M. López, A. López-Oramas, E. Lorenz, M. Makariev, G. Maneva, N. Mankuzhiyil, K. Mannheim, L. Maraschi, M. Mariotti, M. Martínez, D. Mazin, M. Meucci, J. M. Miranda, R. Mirzoyan, J. Moldón, A. Moralejo, P. Munar-Adrover, A. Niedzwiecki, D. Nieto, K. Nilsson, N. Nowak, R. Orito, D. Paneque, R. Paoletti, S. Pardo, J. M. Paredes, S. Partini, M. A. Perez-Torres, M. Persic, L. Peruzzo, M. Pilia, J. Pochon, F. Prada, P. G. P. Moroni, E. Prandini, I. P. Gimenez, I. Puljak, I. Reichardt, R. Reinthal, W. Rhode, M. Ribó, J. Rico, S. Rügamer, A. Saggion, K. Saito, T. Y. Saito, M. Salvati, K. Satalecka, V. Scalzotto, V. Scapin, C. Schultz, T. Schweizer, M. Shayduk, S. N. Shore, A. Sillanpää, J. Sitarek, I. Šnidarić, D. Sobczynska, F. Spanier, S. Spiro, V. Stamatescu, A. Stamerra, B. Steinke, J. Storz, N. Strah, T. Surić, L. Takalo, H. Takami, F. Tavecchio, P. Temnikov, T. Terzić, D. Tescaro, M. Teshima, O. Tibolla, D. F. Torres, A. Treves, M. Uellenbeck, H. Vankov, P. Vogler, R. M. Wagner, Q. Weitzel, V. Zabalza, F. Zandanel, R. Zanin, and K. Hirotani. Phase-resolved energy spectra of the Crab pulsar in the range of 50–400 GeV measured with the MAGIC telescopes. *Astronomy & Astrophysics*, **540**, A69 (2012).

[20] J. Aleksić, E. A. Alvarez, L. A. Antonelli, P. Antoranz, M. Asensio, M. Backes, J. A. Barrio, D. Bastieri, J. B. González, W. Bednarek, A. Berdyugin, K. Berger, E. Bernardini, A. Biland, O. Blanch, R. K. Bock, A. Boller, G. Bonnoli, D. B. Tridon, I. Braun,

T. Bretz, A. Cañellas, E. Carmona, A. Carosi, P. Colin, E. Colombo, J. L. Contreras, J. Cortina, L. Cossio, S. Covino, F. Dazzi, A. D. Angelis, G. D. Caneva, E. D. C. del Pozo, B. D. Lotto, C. D. Mendez, A. D. Ortega, M. Doert, A. Domínguez, D. D. Prester, D. Dorner, M. Doro, D. Eisenacher, D. Elsaesser, D. Ferenc, M. V. Fonseca, L. Font, C. Fruck, R. J. G. López, M. Garczarczyk, D. Garrido, G. Giavitto, N. Godinović, D. Hadasch, D. Häfner, A. Herrero, D. Hildebrand, D. Höhne-Mönch, J. Hose, D. Hrupec, T. Jogler, H. Kellermann, S. Klepser, T. Krähenbühl, J. Krause, J. Kushida, A. L. Barbera, D. Lelas, E. Leonardo, E. Lindfors, S. Lombardi, M. López, A. López-Oramas, E. Lorenz, M. Makariev, G. Maneva, N. Mankuzhiyil, K. Mannheim, L. Maraschi, B. Marcote, M. Mariotti, M. Martínez, D. Mazin, M. Meucci, J. M. Miranda, R. Mirzoyan, J. Moldón, A. Moralejo, P. Munar-Adrover, D. Nieto, K. Nilsson, R. Orito, N. Otte, I. Oya, D. Paneque, R. Paoletti, S. Pardo, J. M. Paredes, S. Partini, M. A. Perez-Torres, M. Persic, L. Peruzzo, M. Pilia, J. Pochon, F. Prada, P. G. P. Moroni, E. Prandini, I. P. Gimenez, I. Puljak, I. Reichardt, R. Reinthal, W. Rhode, M. Ribó, J. Rico, M. Rissi, S. Rügamer, A. Saggion, K. Saito, T. Y. Saito, M. Salvati, K. Satalecka, V. Scalzotto, V. Scapin, C. Schultz, T. Schweizer, M. Shayduk, S. N. Shore, A. Sillanpää, J. Sitarek, I. Snidaric, D. Sobczynska, F. Spanier, S. Spiro, V. Stamatescu, A. Stamerra, B. Steinke, J. Storz, N. Strah, T. Surić, L. Takalo, H. Takami, F. Tavecchio, P. Temnikov, T. Terzić, D. Tescaro, M. Teshima, O. Tibolla, D. F. Torres, A. Treves, M. Uellenbeck, H. Vankov, P. Vogler, R. M. Wagner, Q. Weitzel, V. Zabalza, F. Zandanel, R. Zanin, and K. Hirotani. Observations of the Crab Pulsar between 25 and 100 GeV with the MAGIC I Telescope. *The Astrophysical Journal*, **742**, 43 (2011).

[21] , E. Aliu, T. Arlen, T. Aune, M. Beilicke, W. Benbow, A. Bouvier, S. M. Bradbury, J. H. Buckley, V. Bugaev, K. Byrum, A. Cannon, A. Cesarini, J. L. Christiansen, L. Ciupik, E. Collins-Hughes, M. P. Connolly, W. Cui, R. Dickherber, C. Duke, M. Errando, A. Falcone, J. P. Finley, G. Finnegan, L. Fortson, A. Furniss, N. Galante, D. Gall, K. Gibbs, G. H. Gillanders, S. Godambe, S. Griffin, J. Grube, R. Guenette, G. Gyuk, D. Hanna, J. Holder, H. Huan, G. Hughes, C. M. Hui, T. B. Humensky, A. Imran,

P. Kaaret, N. Karlsson, M. Kertzman, D. Kieda, H. Krawczynski, F. Krennrich, M. J. Lang, M. Lyutikov, A. S. Madhavan, G. Maier, P. Majumdar, S. McArthur, A. McCann, M. McCutcheon, P. Moriarty, R. Mukherjee, P. Nuñez, R. A. Ong, M. Orr, A. N. Otte, N. Park, J. S. Perkins, F. Pizlo, M. Pohl, H. Prokoph, J. Quinn, K. Ragan, L. C. Reyes, P. T. Reynolds, E. Roache, H. J. Rose, J. Ruppel, D. B. Saxon, M. Schroedter, G. H. Sembroski, G. D. Şentürk, A. W. Smith, D. Staszak, G. Tešić, M. Theiling, S. Thibadeau, K. Tsurusaki, J. Tyler, A. Varlotta, V. V. Vassiliev, S. Vincent, M. Vivier, S. P. Wakely, J. E. Ward, T. C. Weekes, A. Weinstein, T. Weisgarber, D. A. Williams, and B. Zitzer. Detection of Pulsed Gamma Rays Above 100 GeV from the Crab Pulsar. *Science*, **334**, 69 (2011).

[22] F. A. Aharonian, S. V. Bogovalov, and D. Khangulyan. Abrupt acceleration of a 'cold' ultrarelativistic wind from the Crab pulsar. *Nature*, **482**, 507 (2012).

[23] M. Lyutikov, D. Balsara, and C. Matthews. Crab GeV flares from the corrugated termination shock. *Monthly Notices of the Royal Astronomical Society*, **422**, 3118 (2012).

[24] L. Sironi and A. Spitkovsky. Particle Acceleration in Relativistic Magnetized Collisionless Electron-Ion Shocks. *The Astrophysical Journal*, **726**, 75 (2010).

[25] M. Yamada, H. Ji, S. Hsu, T. Carter, R. Kulsrud, N. Bretz, F. Jobes, Y. Ono, and F. Perkins. Study of driven magnetic reconnection in a laboratory plasma. *Physics of Plasmas*, **4** 1936 (1997).

[26] E. G. Zweibel and M. Yamada. Magnetic Reconnection in Astrophysical and Laboratory Plasmas. *Annual Review of Astronomy and Astrophysics*, **47**, 291 (2009).

[27] H. Ji, T. Carter, S. Hsu, and M. Yamada. Study of local reconnection physics in a laboratory plasma. *Earth, Planets and Space*, **53**, 539 (2001).

[28] M. Yamada, Y. Ren, H. Ji, J. Breslau, S. Gerhardt, R. Kulsrud, and A. Kuritsyn. Experimental study of two-fluid effects on magnetic reconnection in a laboratory plasma with variable collisionality. *Physics of Plasmas*, **13**, 052119 (2006).

[29] M. Yamada. Progress in understanding magnetic reconnection in laboratory and space astrophysical plasmasa). *Physics of Plasmas*, **14**, 058102 (2007).

[30] P. Sweet. The Neutral Point Theory of Solar Flares, in *IAU Symposium 6, Electromagnetic Phenomena in Cosmical Physics* (1958).

[31] P. M. Nilson, L. Willingale, M. C. Kaluza, C. Kamperidis, S. Minardi, M. S. Wei, P. Fernandes, M. Notley, S. Bandyopadhyay, M. Sherlock, R. J. Kingham, M. Tatarakis, Z. Najmudin, W. Rozmus, R. G. Evans, M. G. Haines, A. E. Dangor, and K. Krushelnick. Magnetic Reconnection and Plasma Dynamics in Two-Beam Laser-Solid Interactions. *Physical Review Letters*, **97**, 255001 (2006).

[32] L. Willingale, P. M. Nilson, M. C. Kaluza, A. E. Dangor, R. G. Evans, P. Fernandes, M. G. Haines, C. Kamperidis, R. J. Kingham, C. P. Ridgers, M. Sherlock, A. G. R. Thomas, M. S. Wei, Z. Najmudin, K. Krushelnick, S. Bandyopadhyay, M. Notley, S. Minardi, M. Tatarakis, and W. Rozmus. Proton deflectometry of a magnetic reconnection geometry. *Physics of Plasmas*, **17**, 043104 (2010).

[33] C. K. Li, F. H. Séguin, J. A. Frenje, J. R. Rygg, R. D. Petrasso, R. P. J. Town, O. L. Landen, J. P. Knauer, and V. A. Smalyuk. Observation of Megagauss-Field Topology Changes due to Magnetic Reconnection in Laser-Produced Plasmas. *Physical Review Letters*, **99**, 055001 (2007).

[34] J. Zhong, Y. Li, X. Wang, J. Wang, Q. Dong, C. Xiao, S. Wang, X. Liu, L. Zhang, L. An, F. Wang, J. Zhu, Y. Gu, X. He, G. Zhao, and J. Zhang. Modelling loop-top X-ray source and reconnection outflows in solar flares with intense lasers. *Nature Physics*, **6**, 984 (2011).

[35] Q.-L. Dong, S.-J. Wang, Q.-M. Lu, C. Huang, D.-W. Yuan, X. Liu, X.-X. Lin, Y.-T. Li, H.-G. Wei, J.-Y. Zhong, J.-R. Shi, S.-E. Jiang, Y.-K. Ding, B.-B. Jiang, K. Du, X.-T. He, M. Y. Yu, C. S. Liu, S. Wang, Y.-J. Tang, J.-Q. Zhu, G. Zhao, Z.-M. Sheng, and J. Zhang. Plasmoid Ejection and Secondary Current Sheet Generation from Magnetic Reconnection in Laser-Plasma Interaction. *Physical Review Letters*, **108**, 215001 (2012).

[36] G. Fiksel, W. Fox, A. Bhattacharjee, D. H. Barnak, P.-Y. Chang, K. Germaschewski, S. X. Hu, and P. M. Nilson. Magnetic Reconnection between Colliding Magnetized Laser-Produced Plasma Plumes. *Physical Review Letters*, **113**, 105003 (2014).

[37] M. J. Rosenberg, C. K. Li, W. Fox, A. B. Zylstra, C. Stoeckl, F. H. Séguin, J. A. Frenje, and R. D. Petrasso. Slowing of Magnetic Reconnection Concurrent with Weakening Plasma Inflows and Increasing Collisionality in Strongly Driven Laser-Plasma Experiments. *Physical Review Letters*, **114**, 205004 (2015).

[38] M. J. Rosenberg, C. K. Li, W. Fox, I. Igumenschev, F. H. Seguin, J. A. Frenje, C. Stoeckl, V. Glebov, and R. D. Petrasso. A Laboratory Study of Asymmetric Magnetic Reconnection in Strongly Driven Plasmas. *Nature Communications*, **6**, 6190 (2015).

[39] S. R. Totorica, T. Abel, and F. Fiuza. Nonthermal Electron Energization from Magnetic Reconnection in Laser-Driven Plasmas. *Physical Review Letters*, **116**, 095003 (2016).

[40] A. Lazarian, G. L. Eyink, E. T. Vishniac, and G. Kowal. *Magnetic Reconnection in Astrophysical Environments*, pp. 311–372. Springer Berlin Heidelberg, Berlin, Heidelberg (2015). ISBN 978-3-662-44625-6.

[41] A. S. Joglekar, A. G. R. Thomas, W. Fox, and A. Bhattacharjee. Magnetic Reconnection in Plasma under Inertial Confinement Fusion Conditions Driven by Heat Flux Effects in Ohm's Law. *Phys. Rev. Lett.*, **112**, 105004 (2014).

[42] D. Strickland and G. Mourou. Compression of amplifed chirped optical pulses. *Optics Communications*, **55(6)**, 447 (1985).

[43] V. Yanovsky, V. Chvykov, G. Kalinchenko, P. Rousseau, T. Plancon, T. Matsuoka, A. Maksimchuk, J. Ness, G. Cheriaux, G. Mourou, and K. Krushelnick. Ultra-high intensity-300-TW laser at 0.1 Hz Repetition Rate. *Optics Express*, **16(3)**, 2019 (2008).

[44] A. Dubietis, G. Jonušauskas, and A. Piskarskas. Powerful femtosecond pulse generation by chirped and stretched pulse parametric amplification in BBO crystal. *Optics Communications*, **88**, 437 (1992).

[45] I. Ross, P. Matousek, M. Towrie, A. Langley, and J. Collier. The prospects for ultrashort pulse duration and ultrahigh intensity using optical parametric chirped pulse amplifiers. *Optics Communications*, **144**, 125 (1997).

[46] I. N. Ross, J. L. Collier, P. Matousek, C. N. Danson, D. Neely, R. M. Allott, D. A. Pepler, C. Hernandez-Gomez, and K. Osvay. Generation of terawatt pulses by use of optical parametric chirped pulse amplification. *Applied Optics*, **39**, 2422 (2000).

[47] E. Treacy. Optical pulse compression with diffraction gratings. *IEEE Journal of Quantum Electronics*, **5**, 454 (1969).

[48] F. Brunel. Not-so-resonant, Resonant Absorption. *Physical Review Letters*, **59**, 52 (1987).

[49] J. P. Freidberg, R. W. Mitchell, R. L. Morse, and L. I. Rudsinski. Resonant Absorption of Laser Light by Plasma Targets. *Physical Review Letters*, **28**, 795 (1972).

[50] P. Wang, J. Hua, Y. Lin, and Y. Ho. Ponderomotive acceleration of electrons by an ultrashort laser pulse. *Physics Letters A*, **300**, 76 (2002).

[51] W. L. Kruer. *The Physics of Laser Plasma Interactions.* Westview Press (1988), 1st edition edition (2003).

[52] P. Gibbon. *Short Pulse Laser Interactions with Matter: An Introduction.* Imperial College Press (2007).

[53] M. G. Haines. Saturation Mechanisms for the Generated Magnetic Field in Nonuniform Laser-Matter Irradiation. *Physical Review Letters*, **78**, 254 (1997).

[54] A. R. Bell, F. N. Beg, Z. Chang, A. E. Dangor, C. N. Danson, C. B. Edwards, A. P. Fews, M. H. R. Hutchinson, S. Luan, P. Lee, P. A. Norreys, R. A. Smith, P. F.

Taday, and F. Zhou. Observation of plasma confinement in picosecond laser-plasma interactions. *Physical Review E*, **48**, 2087 (1993).

[55] M. Chen, Z.-M. Shenga, J. Zheng, Y.-Y. Ma, M. A. Bari, Y.-T. Li, and J. Zhang. Surface electron acceleration in relativistic laser-solid interactions. *Optics Express*, **14**, 3093 (2006).

[56] W. Schumaker, N. Nakanii, C. McGuffey, C. Zulick, V. Chyvkov, F. Dollar, H. Habara, G. Kalintchenko, A. Maksimchuk, K. A. Tanaka, A. G. R. Thomas, V. Yanovsky, and K. Krushelnick. Ultrafast Electron Radiography of Magnetic Fields in High-Intensity Laser-Solid Interactions. *Physical Review Letters*, **110**, 015003 (2013).

[57] D. W. Forslund, J. M. Kindel, and K. Lee. Theory of Hot-Electron Spectra at High Laser Intensity. *Physical Review Letters*, **39**, 284 (1977).

[58] W. Priedhorsky, D. Lier, R. Day, and D. Gerke. Hard-X-Ray Measurements of 10.6-μm Laser-Irradiated Targets. *Physical Review Letters*, **47**, 1661 (1981).

[59] P. Gibbon and A. R. Bell. Collisionless absorption in sharp-edged plasmas. *Physical Review Letters*, **68**, 1535 (1992).

[60] F. Pegoraro. Generalised relativistic Ohm's laws, extended gauge transformations, and magnetic linking. *Physics of Plasmas*, **22**, 112106 (2015).

[61] C. Chin-Fatt, A. W. DeSilva, G. C. Goldenbaum, R. Hess, C. Coté, A. Filuk, J. Gauvreau, and F. K. Hwang. Formation and decay of a spheromak plasma. *Physics of Fluids B*, **5** 1816 (1993).

[62] R. Susino, A. Bemporad, and S. Mancuso. Physical Conditions of Coronal Plasma at the Transit of a Shock Driven by a Coronal Mass Ejection. *The Astrophysical Journal*, **812**, 119 (2015).

[63] A. Kandus and C. G. Tsagas. Generalized Ohm's law for relativistic plasmas. *Monthly Notices RAS*, **385**, 883 (2008).

[64] J. D. Hares, J. D. Kilkenny, M. H. Key, and J. G. Lunney. Measurement of Fast-Electron Energy Spectra and Preheating in Laser-Irradiated Targets. *Physical Review Letters*, **42**, 1216 (1979).

[65] H. Chen, B. Soom, B. Yaakobi, S. Uchida, and D. D. Meyerhofer. Hot-electron Characterization from $K\alpha$ Measurements in High-contrast, p-Polarized, Picosecond Laser-Plasma Interactions. *Physical Review Letters*, **70**, 3431 (1993).

[66] K. B. Wharton, S. P. Hatchett, S. C. Wilks, M. H. Key, J. D. Moody, V. Yanovsky, A. A. Offenberger, B. A. Hammel, M. D. Perry, and C. Joshi. Experimental Measurements of Hot Electrons Generated by Ultraintense ($> 10^{19} W/cm^2$) Laser-Plasma Interactions on Solid-Density Targets. *Physical Review Letters*, **81**, 822 (1998).

[67] K. Yasuike, M. H. Key, S. P. Hatchett, R. A. Snavely, and K. B. Wharton. Hot electron diagnostic in a solid laser target by K-shell lines measurement from ultraintense laser–plasma interactions ($3 \times 10^{20} W/cm^2$, 400 J). *Review of Scientific Instruments*, **72**, 1236 (2001).

[68] L. Willingale, A. G. R. Thomas, A. Maksimchuk, A. Morace, T. Bartal, J. Kim, R. B. Stephens, M. S. Wei, F. N. Beg, and K. Krushelnick. Investigation of relativistic intensity laser generated hot electron dynamics via copper K-alpha imaging and proton acceleration. *Physics of Plasmas*, **20**, 123112 (2013).

[69] H. Sawada, W. Theobald, C. Stoeckl, G. Fiksel, P. K. Patel, C. D. Chen, T. Yabuuchi, F. N. Beg, R. B. Stephens, K. U. Akli, H. S. McLean, and M. H. Key. Monochromatic Imaging of 8.0-keV Cu K-alpha Emission Induced by Energetic Electrons Generated at OMEGA EP . *IEEE Transactions on Plasma Science*, **39**, 2816 (2011).

[70] T. Ma, F. N. Beg, A. G. MacPhee, H.-K. Chung, M. H. Key, A. J. Mackinnon, P. K. Patel, S. Hatchett, K. U. Akli, R. B. Stephens, C. D. Chen, R. R. Freeman, A. Link, D. T. Offermann, V. Ovchinnikov, and L. D. Van Woerkom. Electron heated target temperature measurements in petawatt laser experiments based on extreme ultraviolet imaging and spectroscopy. *Review of Scientific Instruments*, **79**, 10 (2008).

[71] W. Bambynek, B. Crasemann, R. W. Fink, H. U. Fruend, H. Mark, C. D. Swift, R. E. Price, and P. V. Rao. X-Ray Fluorescence Yields, Auger, and Coster-Kronig Transition Probabilities. *Review of Modern Physics*, **44**, 716 (1972).

[72] A. G. R. Thomas, M. Sherlock, C. Kuranz, C. P. Ridgers, and R. P. Drake. Hybrid Vlasov–Fokker–Planck–Maxwell simulations of fast electron transport and the time dependance of K shell excitation in a mid-Z metallic target. *New Journal of Physics*, **15**, 015017 (2013).

[73] M. Guerra, F. Parente, P. Indelicato, and J. P. Santos. Modified binary encounter Bethe model for electron-impact ionization. *International Journal of Mass Spectrometry*, **313**, 1 (2013).

[74] X. Llovet, C. J. Powell, F. Salvat, and A. Jablonski. Cross Sections for Inner-Shell Ionization by Electron Impact. *Journal of Physical and Chemical Reference Data*, **43**, 013102 (2014).

[75] J. Myatt, W. Theobald, J. A. Delettrez, C. Stoeckl, M. Storm, T. C. Sangster, A. V. Maximov, and R. W. Short. High-intensity laser interactions with mass-limited solid targets and implications for fast-ignition experiments on OMEGA EP). *Physics of Plasmas*, **14**, 056301 (2007).

[76] J. MacFarlane, I. Golovkin, P. Woodruff, S. Kulkarni, and I. Hall Simulation of plasma ionization and spectral properties with PrismSPECT. *IEEE International Conference on Plasma Science (ICOPS), 2013 Abstracts.* 1 (2013).

[77] H. E. Petschek. Magnetic Field Annihilation. *NASA Special Publication*, **50**, 425 (1964).

[78] H. Baty, E. R. Priest, and T. G. Forbes. Petschek-like reconnection with uniform resistivity. *Physics of Plasmas*, **16**, 060701 (2009).

[79] H. Baty, T. G. Forbes, and E. R. Priest. The formation and stability of Petschek reconnection. *Physics of Plasmas*, **21**, 112111 (2014).

[80] D. Biskamp. Magnetic reconnection via current sheets. *Physics of Fluids*, **29**, 1520 (1986).

[81] T. Shibayama, K. Kusano, T. Miyoshi, T. Nakabou, and G. Vekstein. Fast magnetic reconnection supported by sporadic small-scale Petschek-type shocks. *Physics of Plasmas*, **22**, 100706 (2015).

[82] M. Hoshino and Y. Lyubarsky. Relativistic Reconnection and Particle Acceleration. *Space Science Reviews*, **173**, 521 (2012).

[83] D. A. Larrabee, R. V. E. Lovelace, and M. M. Romanova. Lepton Acceleration by Relativistic Collisionless Magnetic Reconnection. *The Astrophysical Journal*, **586**, 72 (2003).

[84] Y. Lyubarsky and M. Liverts. Particle Acceleration in the Driven Relativistic Reconnection. *The Astrophysical Journal*, **682**, 1436 (2008).

[85] L. Sironi and A. Spitkovsky. Acceleration of Particles at the Termination Shock of a Relativistic Striped Wind. *The Astrophysical Journal*, **741**, 39 (2011).

[86] J. G. Kirk. Particle Acceleration in Relativistic Current Sheets. *Physical Review Letters*, **92**, 181101 (2004).

[87] O. C. de Jager, A. K. Harding, P. F. Michelson, H. I. Nel, P. L. Nolan, P. Sreekumar, and D. J. Thompson. Gamma-Ray Observations of the Crab Nebula: A Study of the Synchro-Compton Spectrum. *The Astrophysical Journal*, **457**, 253 (1996).

[88] A. A. Abdo, M. Ackermann, M. Ajello, A. Allafort, L. Baldini, J. Ballet, G. Barbiellini, D. Bastieri, K. Bechtol, R. Bellazzini, B. Berenji, R. D. Blandford, E. D. Bloom, E. Bonamente, A. W. Borgland, A. Bouvier, T. J. Brandt, J. Bregeon, A. Brez, M. Brigida, P. Bruel, R. Buehler, S. Buson, G. A. Caliandro, R. A. Cameron, A. Cannon, P. A. Caraveo, J. M. Casandjian, Ö. Çelik, E. Charles, A. Chekhtman, C. C. Cheung, J. Chiang, S. Ciprini, R. Claus, J. Cohen-Tanugi, L. Costamante, S. Cutini, F. D'Ammando, C. D. Dermer, A. de Angelis, A. de Luca, F. de Palma, S. W.

Digel, E. do Couto e Silva, P. S. Drell, A. Drlica-Wagner, R. Dubois, D. Dumora, C. Favuzzi, S. J. Fegan, E. C. Ferrara, W. B. Focke, P. Fortin, M. Frailis, Y. Fukazawa, S. Funk, P. Fusco, F. Gargano, D. Gasparrini, N. Gehrels, S. Germani, N. Giglietto, F. Giordano, M. Giroletti, T. Glanzman, G. Godfrey, I. A. Grenier, M.-H. Grondin, J. E. Grove, S. Guiriec, D. Hadasch, Y. Hanabata, A. K. Harding, K. Hayashi, M. Hayashida, E. Hays, D. Horan, R. Itoh, G. Jóhannesson, A. S. Johnson, T. J. Johnson, D. Khangulyan, T. Kamae, H. Katagiri, J. Kataoka, M. Kerr, J. Knödlseder, M. Kuss, J. Lande, L. Latronico, S.-H. Lee, M. Lemoine-Goumard, F. Longo, F. Loparco, P. Lubrano, G. M. Madejski, A. Makeev, M. Marelli, M. N. Mazziotta, J. E. McEnery, P. F. Michelson, W. Mitthumsiri, T. Mizuno, A. A. Moiseev, C. Monte, M. E. Monzani, A. Morselli, I. V. Moskalenko, S. Murgia, T. Nakamori, M. Naumann-Godo, P. L. Nolan, J. P. Norris, E. Nuss, T. Ohsugi, A. Okumura, N. Omodei, J. F. Ormes, M. Ozaki, D. Paneque, D. Parent, V. Pelassa, M. Pepe, M. Pesce-Rollins, M. Pierbattista, F. Piron, T. A. Porter, S. Rainò, R. Rando, P. S. Ray, M. Razzano, A. Reimer, O. Reimer, T. Reposeur, S. Ritz, R. W. Romani, H. F.-W. Sadrozinski, D. Sanchez, P. M. S. Parkinson, J. D. Scargle, T. L. Schalk, C. Sgrò, E. J. Siskind, P. D. Smith, G. Spandre, P. Spinelli, M. S. Strickman, D. J. Suson, H. Takahashi, T. Takahashi, T. Tanaka, J. B. Thayer, D. J. Thompson, L. Tibaldo, D. F. Torres, G. Tosti, A. Tramacere, E. Troja, Y. Uchiyama, J. Vandenbroucke, V. Vasileiou, G. Vianello, V. Vitale, P. Wang, K. S. Wood, Z. Yang, and M. Ziegler. Gamma-Ray Flares from the Crab Nebula. *Science*, **331**, 739 (2011).

[89] D. A. Uzdensky. Magnetic Reconnection in Extreme Astrophysical Environments. *Space Science Reviews*, **160**, 45 (2011).

[90] P. M. Nilson, L. Willingale, M. C. Kaluza, C. Kamperidis, S. Minardi, M. S. Wei, P. Fernandes, M. Notley, S. Bandyopadhyay, M. Sherlock, R. J. Kingham, M. Tatarakis, Z. Najmudin, W. Rozmus, R. G. Evans, M. G. Haines, A. E. Dangor, and K. Krushelnick. Bidirectional jet formation during driven magnetic reconnection in two-beam laser–plasma interactions. *Physics of Plasmas*, **15**, 092701 (2008).

[91] A. S. Joglekar, A. G. R. Thomas, W. Fox, and A. Bhattacharjee. Magnetic Reconnection in Plasma under Inertial Confinement Fusion Conditions Driven by Heat Flux Effects in Ohm's Law. *Phys. Rev. Lett.*, **112**, 105004 (2014).

[92] D. D. Ryutov, R. P. Drake, and B. A. Remington. Criteria for Scaled Laboratory Simulations of Astrophysical MHD Phenomena. *The Astrophysical Journal Supplement Series*, **127**, 465 (2000).

[93] S. V. Bulanov, F. Pegoraro, and A. S. Sakharov. Magnetic reconnection in electron magnetohydrodynamics. *Physics of Fluids B*, **4**, 2499 (1992).

[94] Y. L. Ping, J. Y. Zhong, Z. M. Sheng, X. G. Wang, B. Liu, Y. T. Li, X. Q. Yan, X. T. He, J. Zhang, and G. Zhao. Three-dimensional fast magnetic reconnection driven by relativistic ultraintense femtosecond lasers. *Physical Review E*, **89**, 031101 (2014).

[95] O. A. A. Jullien and S. Saltiel. 10^{10} temporal contrast for femtosecond ultraintense lasers by cross-polarized wave generation. *Optics Letters*, **30**, 920 (2005).

[96] V. Chvykov, P. Rousseau, S. Reed, G. Kalinchenko, and V. Yanovsky. Generation of 10^{11} contrast 50 TW laser pulses. *Optics Letters*, **31**, 1456 (2006).

[97] Omega EP System Operations Manual (Volume VII - System Description). `http://www.lle.rochester.edu/omega_facility/documentation/volume_vii.php` (2006).

[98] Jupiter Laser Facility: Titan Laser. `https://jlf.llnl.gov/laser-facilities/titan` (2016).

[99] R. A. Lerche, J. W. McDonald, R. L. Griffith, G. V. d. Dios, D. S. Andrews, A. W. Huey, P. M. Bell, O. L. Landen, P. A. Jaanimagi, and R. Boni. Preliminary performance measurements for a streak camera with a large-format direct-coupled charge-coupled device readout. *Review of Scientific Instruments*, **75** 4042 (2004).

[100] F. Dollar, T. Matsuoka, G. M. Petrov, A. G. R. Thomas, S. S. Bulanov, V. Chvykov, J. Davis, G. Kalinchenko, C. McGuffey, L. Willingale, V. Yanovsky, A. Maksimchuk,

and K. Krushelnick. Control of Energy Spread and Dark Current in Proton and Ion Beams Generated in High-Contrast Laser Solid Interactions. *Physical Review Letters*, **107**, 065003 (2011).

[101] OMEGA EP Temporal Contrast Measurements. http://www.lle.rochester.edu/media/about/OLUG_workshop/OLUG10_workshop/documents/Dorrer_OLUG10.pdf (2010).

[102] C. Stoeckl, G. Fiksel, D. Guy, C. Mileham, P. M. Nilson, T. C. Sangster, M. J. Shoup, and W. Theobald. A spherical crystal imager for OMEGA EP. *Review of Scientific Instruments*, **83**, 033107 (2012).

[103] Ultra Fast X-ray Streak Camera for TIM Based Platforms. https://e-reports-ext.llnl.gov/pdf/614073.pdf (2012).

[104] C. Thomas, G. Rehm, I. Martin, and R. Bartolini. X-ray pinhole camera resolution and emittance measurement. *Physical Review Accelerators and Beams*, **13**, 022805 (2010).

[105] S. R. Nagel, T. J. Hilsabeck, P. M. Bell, D. K. Bradley, M. J. Ayers, K. Piston, B. Felker, J. D. Kilkenny, T. Chung, B. Sammuli, J. D. Hares, and A. K. L. Dymoke-Bradshaw. Investigating high speed phenomena in laser plasma interactions using dilation x-ray imager (invited)a). *Review of Scientific Instruments*, **85**, 11 (2014).

[106] S. Fourmaux, S. Corde, K. T. Phuoc, P. M. Leguay, S. Payeur, P. Lassonde, S. Gnedyuk, G. Lebrun, C. Fourment, V. Malka, S. Sebban, A. Rousse, and J. C. Kieffer. Demonstration of the synchrotron-type spectrum of laser-produced Betatron radiation. *New Journal of Physics*, **13**, 033017 (2011).

[107] Single Photon Counting Spectrometer (SPC). Volume VIII System Shot Operations. Chapter 6 Experimental Diagnostics. D-TX-P-118 Rev C. http://www.lle.rochester.edu/04_resources/04_07_PDM/pdmdocs/release/D/D-TX/D-TX-P-118/C/D-TX-P-118_REVC.PDF (2012).

[108] D. C. Slater. Thomson parabola ion analyzer for laser-plasma studies. *Review of Scientific Instruments*, **49**, 1493 (1978).

[109] A. Buck, K. Zeil, A. Popp, K. Schmid, A. Jochmann, S. D. Kraft, B. Hidding, T. Kudyakov, C. M. S. Sears, L. Veisz, S. Karsch, J. Pawelke, R. Sauerbrey, T. Cowan, F. Krausz, and U. Schramm. Absolute charge calibration of scintillating screens for relativistic electron detection. *Review of Scientific Instruments*, **81**, 033301 (2010).

[110] H. Chen, A. J. Link, R. van Maren, P. K. Patel, R. Shepherd, S. C. Wilks, and P. Beiersdorfer. High performance compact magnetic spectrometers for energetic ion and electron measurement in ultraintense short pulse laser solid interactionsa). *Review of Scientific Instruments*, **79**, 10 (2008).

[111] W. Liang, Y. Li, M. Xu, X. Yuan, Z. Zheng, Y. Zhang, F. Liu, Z. Wang, H. Li, Z. Jin, Z. Wei, W. Zhao, Y. Li, and J. Zhang. Study of hot electrons generated from intense laser-plasma interaction employing Image Plate. *Science in China Series G: Physics, Mechanics and Astronomy*, **51**, 1455 (2008). ISSN 1862-2844.

[112] T. Bonnet, M. Comet, D. Denis-Petit, F. Gobet, F. Hannachi, M. Tarisien, M. Versteegen, and M. M. Aléonard. Response functions of imaging plates to photons, electrons and 4He particles. *Review of Scientific Instruments*, **84**, 103510 (2013).

[113] H. Chen, N. L. Back, T. Bartal, F. N. Beg, D. C. Eder, A. J. Link, A. G. MacPhee, Y. Ping, P. M. Song, A. Throop, and L. Van Woerkom. Absolute calibration of image plates for electrons at energy between 100keV and 4MeV. *Review of Scientific Instruments*, **79**, 033301 (2008).

[114] A. Davies, D. Haberberger, R. Boni, S. Ivancic, R. Brown, and D. H. Froula. Polarimetry diagnostic on OMEGA EP using a 10-ps, 263-nm probe beama). *Review of Scientific Instruments*, **85**, 11 (2014).

[115] D. Haberberger. Optical Probing Measurements on OMEGA EP. `http://www.lle.rochester.edu/media/about/OLUG_workshop/OLUG14_workshop/documents/Haberberger_OLUG14.pdf` (2004).

[116] R. A. Fonseca, L. O. Silva, F. S. Tsung, V. K. Decyk, W. Lu, C. Ren, W. B. Mori, S. Deng, S. Lee, T. Katsouleas, and J. C. Adam. *Computational Science — ICCS*

2002: International Conference Amsterdam, The Netherlands, April 21–24, 2002 Proceedings, Part III, chapter OSIRIS: A Three-Dimensional, Fully Relativistic Particle in Cell Code for Modeling Plasma Based Accelerators, pp. 342–351. Springer Berlin Heidelberg, Berlin, Heidelberg (2002). ISBN 978-3-540-47789-1.

[117] F. J. Marshall, T. Ohki, D. McInnis, Z. Ninkov, and J. Carbone. Imaging of laser–plasma x-ray emission with charge-injection devices. *Review of Scientific Instruments*, **72**, 713 (2001).

[118] V. Chvykov, P. Rousseau, S. Reed, G. Kalinchenko, and V. Yanovsky. Generation of 10^{11} contrast 50 TW laser pulses. *Optics Letters*, **31**, 1456 (2006).

[119] C. Reich, I. Uschmann, F. Ewald, S. Düsterer, A. Lübcke, H. Schwoerer, R. Sauerbrey, E. Förster, and P. Gibbon. Spatial characteristics of K α x-ray emission from relativistic femtosecond laser plasmas. *Physical Review E*, **68**, 5 (2003).

[120] D. A. Uzdensky and R. M. Kulsrud. Physical origin of the quadrupole out-of-plane magnetic field in Hall-magnetohydrodynamic reconnection. *Physics of Plasmas*, **13**, 062305 (2006).

[121] N. F. Loureiro and D. A. Uzdensky. Magnetic reconnection: from the Sweet Parker model to stochastic plasmoid chains. *Plasma Physics and Controlled Fusion*, **58**, 014021 (2016).

[122] L. Sironi and A. Spitkovsky. Relativistic Reconnection: An Efficient Source of Non-Thermal Particles. *The Astrophysical Journal*, **783**, L21 (2014).

[123] M. A. Yates, D. B. van Hulsteyn, H. Rutkowski, G. Kyrala, and J. U. Brackbill. Experimental Evidence for Self-Generated Magnetic Fields and Remote Energy Deposition in Laser-Irradiated Targets. *Physical Review Letters*, **49**, 1702 (1982).

[124] D. Charalambidis, Z. Diveki, P. Dombi, J. A. Fülöp, M. Kalashnikov, R. Lopez-Martens, K. Osvay, and E. Racz. ELI-ALPS, the attosecond facility of the extreme light infrastructure. In *Lasers and Electro-Optics Europe (CLEO EUROPE/IQEC), 2013 Conference on and International Quantum Electronics Conference*, p. 1 (2013).

[125] E. N. Parker. The Solar-Flare Phenomenon and the Theory of Reconnection and Annihiliation of Magnetic Fields. *Astrophysical Journal Supplement*, **8**, 177 (1963).

[126] J. D. Huba and L. I. Rudakov. Hall Magnetic Reconnection Rate. *Physical Review Letters*, **93**, 175003 (2004).

[127] X. H. Yang, H. B. Zhuo, Y. Y. Ma, H. Xu, T. P. Yu, D. B. Zou, Z. Y. Ge, B. B. Xu, Q. J. Zhu, F. Q. Shao, and M. Borghesi. Effects of resistive magnetic field on fast electron divergence measured in experiments. *Plasma Physics and Controlled Fusion*, **57**, 025011 (2015).

[128] F. Guo, H. Li, W. Daughton, and Y.-H. Liu. Formation of Hard Power Laws in the Energetic Particle Spectra Resulting from Relativistic Magnetic Reconnection. *Physical Review Letters*, **113**, 155005 (2014).

[129] P. M. Nilson, J. R. Davies, W. Theobald, P. A. Jaanimagi, C. Mileham, R. K. Jungquist, C. Stoeckl, I. A. Begishev, A. A. Solodov, J. F. Myatt, J. D. Zuegel, T. C. Sangster, R. Betti, and D. D. Meyerhofer. Time-Resolved Measurements of Hot-Electron Equilibration Dynamics in High-Intensity Laser Interactions with Thin-Foil Solid Targets. *Phys. Rev. Lett.*, **108**, 085002 (2012).

[130] A. G. R. Thomas, M. Sherlock, C. Kuranz, C. P. Ridgers, and R. P. Drake. Hybrid Vlasov-Fokker-Planck-Maxwell simulations of fast electron transport and the time dependance of K -shell excitation in a mid- Z metallic target. *New Journal of Physics*, **15**, 015017 (2013).

[131] H. Chen, J. Bonlie, R. Cauble, F. Fiuza, W. Goldstein, A. Hazi, C. Keane, A. Link, E. Marley, S. R. Nagel, J. Park, R. Shepherd, G. J. Williams, D. D. Meyerhofer, G. Fiksel, D. Barnak, P. Y. Chang, M. Nakai, Y. Arikawa, H. Azechi, S. Fujioka, S. Kojima, N. Miyanaga, T. Morita, T. Nagai, H. Nishimura, T. Ozaki, Y. Sakawa, H. Takabe, Z. Zhang, S. Kerr, R. Fedosejevs, Y. Sentoku, M. P. Hill, D. J. Hoarty, L. M. R. Hobbs, and S. F. James. Progress Towards a Laser Produced Relativistic Electron-Positron Pair Plasma. *Journal of Physics: Conference Series*, **688**, 012010 (2016).

[132] V. Berezhiani, D. Garuchava, and P. Shukla. Production of electron-positron pairs by intense laser pulses in an overdense plasma. *Physics Letters A*, **360**, 624 (2007). ISSN 0375-9601.

[133] W. Luo, Y.-B. Zhu, H.-B. Zhuo, Y.-Y. Ma, Y.-M. Song, Z.-C. Zhu, X.-D. Wang, X.-H. Li, I. C. E. Turcu, and M. Chen. Dense electron-positron plasmas and gamma-ray bursts generation by counter-propagating quantum electrodynamics-strong laser interaction with solid targets. *Physics of Plasmas*, **22**, 063112 (2015).